

THEORETICAL INVESTIGATIONS OF EARLY UNIVERSE
SIMULATORS

KATE BROWN

Thesis submitted for the degree of
Doctor of Philosophy



*School of Mathematics, Statistics & Physics
Newcastle University
Newcastle upon Tyne
United Kingdom*

October 2023

For Lil, who sat me in front of Countdown before I could talk.

Acknowledgements

I would first like to thank my supervisors Ian Moss and Tom Billam for all their guidance over the last four years. Your academic expertise has been invaluable, but so has your patience and support during difficult times. I don't think many supervisors are dedicated enough to hold meetings in their house when the university is closed, but I'm very glad to have found the exception! Thank you both for always finding time for me, no matter how silly or frequent the questions!

I would also like to thank all the wonderful people I've had the privilege of sharing PhD *i* with. Ash, Cristiana, Devika, Francesca, Holly, Jake, Joe, Mario, Stephen, Ryan N, Sam M, Sam W, Stephen and Tao; you're all star of the week in my eyes! I'm also very grateful to the countless others in the department who have helped me out over the years, including (but not limited to) Marios, Nick K, Niko and Ryan D. A special thanks must be given to Tom Bland, for making me believe I was capable of attempting a PhD in the first place, and to the others who started my research journey: Clive Emary, Nick Proukakis and Paolo Comaron.

Outside of the department, I must thank all of the amazing friends who have ridden this rollercoaster with me. Anna, Chris, Corey, Eliza, Emily, Jamie, Kieren, Pearce, Penny and Zoe, thank you for always being there for me, and for the many cups of tea, D&D games, crafting sessions, and wild swims along the way. I suppose I should probably also thank Florence Welch, the North Sea and chocolate.

Finally, I'd like to thank my family for their endless love and encouragement. Thanks goes to my dad, for warning me that algebra could get a bit scary when I was six years old, and to my mam, for making me read every day, because "if you can't read, you can't be a scientist, because you won't be able to understand the question." I'd also like to thank my twin sister Laura, for bringing joy – and stray animals – into every room. Lastly, I'd like to thank my partner Liam, for balancing out my chaos with calmness, for stopping me from living off ready meals for the last year, and for always saying yes to an adventure.

P.S. Thank you to Jettsy the cat, for meowing in my face and biting me as I wrote this.



Abstract

The very early universe remains a mystery, with the nature of phase transitions such as inflation and electroweak symmetry breaking still uncertain. Whilst we cannot probe the early universe itself, we may simulate it, using laboratory analogues, such as ultracold gases. Here, we explore the possibility of first-order transitions, and carry out theoretical investigations to determine the strengths and experimental viability of a range of candidate cold-atom models.

We begin by considering a one-dimensional, two-component, finite-temperature Bose gas. We perform simulations using the stochastic projected Gross-Pitaevskii equation (SPGPE) and verify the validity of this approach, by demonstrating that thermal fluctuations in the relative phase are characteristic of a relativistic thermal system. We go on to simulate vacuum-decay in this system and find agreement between the resultant rates of vacuum decay and those predicted by instanton theory.

In line with experimental protocol, we go on to incorporate time-dependent interactions into this system. This is known to give rise to parametric instabilities. We use analytical methods to locate the resultant resonance bands and determine the dependence of their amplitude on damping rate. Subsequently, we demonstrate that the resonances may be suppressed by raising the damping rate. However, we find the required rate to be unrealistically high, casting doubt on the viability of this model.

We move on to consider a three-component system, free from resonant instabilities, whereby components interact via radio frequency and Raman couplings. Within the elaborate phase structure of the system, we identify an effective Klein-Gordon field. Initially, we examine a one-dimensional, zero-temperature system and use Gross-Pitaevskii simulations within the truncated Wigner approximation to model vacuum-decay. We investigate the dependence of the rate of vacuum decay on particle density and find reasonable agreement with instanton methods.

Next, we extend our three-component investigations to a two-dimensional, finite-temperature gas, and return to SPGPE simulations. This improves the agreement between numerical and theoretical decay rates. Finally, we introduce an optical box trap and find that the trap walls seed vacuum decay.

Contents

1	Introduction	1
1.1	The Early Universe	1
1.1.1	Inflation	2
1.1.2	Electroweak Symmetry Breaking	3
1.1.3	Baryogenesis	5
1.1.4	Quark-Hadron Transition	7
1.2	Vacuum Decay	7
1.2.1	The Coleman Instanton	8
1.2.2	A Practical Solution	12
1.3	Quantum Simulators of Fundamental Physics	12
1.3.1	The Limitations of Observations	12
1.3.2	Analogue Systems	12
1.3.3	False Vacuum Decay	13
1.3.4	QSimFP Consortium	15
1.4	Bose-Einstein Condensation	15
1.4.1	The Prediction of Bose-Einstein Condensation	15
1.4.2	What is Bose-Einstein Condensation?	16
1.4.3	The First Bose-Einstein Condensate	18
1.4.4	Quasi Condensation	18
1.5	Spin	19
1.5.1	Angular Momentum Formalism	19
1.5.2	The Alkali Metals	21

1.5.3	Energy Level Notation	21
1.5.4	Hyperfine Structure	22
1.5.5	The Zeeman Effect	22
1.5.6	Breit-Rabi Diagrams	22
1.6	Modelling a Bose Gas	24
1.6.1	The Gross-Pitaevskii Equation	24
1.6.2	Bogoliubov Expansion	26
1.6.3	Truncated-Wigner Approximation	29
1.6.4	The Stochastic Projected GPE	31
1.6.5	The Spinor GPE	32
1.7	Numerics	34
1.7.1	XMDS2	34
1.7.2	Bootstrap Resampling Approach	35
1.7.3	The Mollweide Projection	35
1.8	Thesis Outline	37
1.9	List of Publications	38
2	Simulating False Vacuum Decay in a Pseudo-Spin-1/2 Bose Gas at Finite Temperature: Static Interaction Potential	39
2.1	Introduction	39
2.2	System	39
2.3	Numerical Modelling	42
2.4	Equilibrium Correlations	43
2.5	Bubble Nucleation	46
2.6	Experimental realization	51
2.7	Conclusion	52
3	Simulating False Vacuum Decay in a Pseudo-Spin-1/2 Bose Gas at Finite Temperature: Oscillatory Interaction Potential	53
3.1	Introduction	53
3.2	System	53

3.3	Time averaging	55
3.4	Instability	56
3.5	Numerical Setup	58
3.6	Numerical Results	59
3.7	Experimental Realization	62
3.8	Conclusion	63
4	Simulating False Vacuum Decay in a Spin-1 Bose Gas at Zero Temperature	64
4.1	Introduction	64
4.2	System	65
4.3	Rescaling	69
4.4	Ground States	70
4.5	Klein-Gordon Limit	74
4.6	Dispersion Relation	76
4.7	Numerical Setup	78
4.8	Numerical Results	79
4.9	Experimental Realisation	83
4.10	Conclusion	84
5	Simulating False Vacuum Decay in a Spin-1 Bose Gas at Finite Temperature	85
5.1	Introduction	85
5.2	System	85
5.3	Numerical Setup: Periodic Boundaries	86
5.4	Numerical Results: Periodic Boundaries	87
5.5	Numerical Setup: Trapping Potential	90
5.6	Numerical Results: Trapping Potential	92
5.7	Experimental Realisation	94
5.8	Conclusion	95
6	Conclusions and Future Work	96

6.1	Conclusions	96
6.1.1	Chapter 2	96
6.1.2	Chapter 3	97
6.1.3	Chapter 4	97
6.1.4	Chapter 5	97
6.1.5	General Conclusions	98
6.2	Future Work	98
6.2.1	Pseudo-Spin-1/2 System	98
6.2.2	Spin-1 System	99
6.2.3	General Ideas	99
A	Appendices	100
B		100
A.1	Reducing the Dimensions of the GPE	100
A.1.1	1D condensate	100
A.1.2	2D condensate	102
C		104
B.1	Reformulating the two-component potential in terms of relative phase . . .	104
B.2	Making the 1D SGPE Dimensionless	105
B.3	Klein-Gordon Reduction of the SGPE	106
B.4	Instanton exponent	113
D		115
C.1	Klein-Gordon Reduction: Time-Dependent Potential	115
C.2	Parametric Resonance: Growth Rate	118
D.1	Spin 1 System: Klein Gordon Reduction	120

List of Figures

1.1	A schematic showing the nature of a second-order electroweak phase transition	4
1.2	A schematic showing the nature of a first-order electroweak phase transition	5
1.3	The typical potential geometry of scalar field that is susceptible to vacuum decay	7
1.4	A schematic of first-order vacuum decay	8
1.5	A schematic demonstrating the process of Bose-Einstein condensation	17
1.6	A schematic demonstrating the wave-like behaviour of matter	17
1.7	The first realisation of Bose-Einstein condensation	18
1.8	The electron configuration of the first three alkali metals	21
1.9	A Breit-Rabi diagram showing the Zeeman splitting of the ground state of hydrogen.	23
1.10	Breit-Rabi diagrams showing the Zeeman splitting of the ground states of potassium and lithium	24
1.11	Level coupling diagrams for a simple spin-1 and pseudo-spin-1/2 system	33
1.12	The Mollweide projection of the globe	36
2.1	The dependence of V_{stat} on ϵ and λ	42
2.2	The correlation function of fluctuations about the true vacuum state	44
2.3	The effective barrier height as a function of temperature	45
2.4	Examples of bubble growth at $T = 0.03T_{\text{CO}}$	46
2.5	The probability, P , of remaining in the false-vacuum state at a range of temperatures	47
2.6	The effect of raising the momentum cut-off on survival probability	49

2.7	The relationship between the rate of false vacuum decay, temperature and barrier height	50
2.8	The effect of lowering the dissipation parameter on the rate of vacuum decay	51
3.1	The evolution of V_{osc} for a range of modulation frequencies	54
3.2	The dependence of the parametric instability on driving frequency and the damping parameter	57
3.3	The role of the control parameter $\alpha(t)$ in the pseudo-spin-1/2 system	59
3.4	The evolution of $\cos(\varphi)$ for a range of values of the damping parameter	60
3.5	The rate of false vacuum decay as a function of the damping parameter	61
4.1	A level coupling diagram of the spin-1 system	65
4.2	The Mollweide projection of the magnetization, $m_z = \zeta_{+1}^2 - \zeta_{-1}^2$, about the sphere $\zeta_{+1}^2 + \zeta_0^2 + \zeta_{-1}^2 = 1$	71
4.3	The Mollweide projection of the interaction potential in the absence of mixing	72
4.4	Plots of the interaction potential in (θ, φ) -space, with $(\zeta_{+1}, \zeta_0, \zeta_{-1}) = (\zeta, \zeta', \zeta)$	73
4.5	The dependence of V_{int} on ϵ and λ at $\theta = 0$	74
4.6	The effective Klein-Gordon potential	76
4.7	A comparison of the Klein-Gordon and Bogoliubov dispersion relations about the false vacuum state	77
4.8	Examples of bubble growth for ${}^7\text{Li}$	80
4.9	The rate of false vacuum decay as a function of density	81
4.10	The rate of false vacuum decay as a function of barrier height	83
5.1	The role of the control parameter $\alpha(t)$ in the spin-1 system	87
5.2	An example realisation of bubble nucleation in ${}^7\text{Li}$	88
5.3	The rate of false vacuum decay as a function of density and temperature	89
5.4	The square trapping potential V_{trap}	91
5.5	The result of propagating the Thomas Fermi solution in real time using the damped GPE	92
5.6	The varying behaviour of example $\cos(\varphi)$ realisations in the presence of V_{trap}	93
5.7	A comparison of the rate of false vacuum decay in the presence and absence of V_{trap}	94

Chapter 1

Introduction

Over the last forty years, the value of cosmological analogue systems has become apparent, with such systems providing a unique new window into the lesser understood processes of our universe. This has been aided by the growing availability of ultracold atom systems, including atomic Bose-Einstein condensates, which have proven to be a versatile medium for probing many-body physics. In this thesis, we focus on one cosmological process in particular: false vacuum decay, whereby a scalar field tunnels through a barrier in its potential, from a metastable state into a stable state, via the nucleation of bubbles. Here, we view this early-universe phase transition through the lens of spinor condensates. We evaluate a number of such cold atom analogue models, by means of extensive numerical investigations. We verify our findings by comparing with well-established theoretical predictions, and go on to prescribe a corresponding experimental protocol for each system considered. We begin with a review of the early universe.

1.1 The Early Universe

The universe is thought to have undergone many phase transitions as its composition evolved from thermal plasma to nucleons, nuclei, elements, galaxies and beyond [1, 2]. Whilst evidence revealing the existence and nature of such transitions accumulates, much remains uncertain about the first moments of our cosmos. Here, we give a non-technical summary of the most established theories, drawing particular attention to those which motivate the investigations of this thesis.

1.1.1 Inflation

There are some fundamental flaws in the Hot Big Bang theory, which can be navigated by appending a period of accelerated expansion. In particular, an epoch of cosmological inflation $10^{-36} - 10^{-32}$ s after the Big Bang, during which time the universe cooled from around 10^{15}GeV to around 10^9GeV , explains both the flatness problem and the horizon problem.

The Flatness Problem

The mass density required for the geometry of the universe to be flat is known as the critical density, ρ_c . This value is unstable; any deviation from $\rho = \rho_c$ is amplified as the universe ages. It is then puzzling that observations [3] show the universe to be remarkably close to flat. Given the age of the universe, this observation requires any departure from flatness in the early universe to have been minuscule. It is possible that this occurred by coincidence, but the general consensus is that it did not. Instead, this feature is accounted for by inflation. Just as inflating a balloon flattens its surface locally, a period of accelerated expansion could render the observable universe flat. Only upon zooming far out would any curvature become apparent.

The Horizon Problem

The cosmic microwave background (CMB) is approximately isotropic, with a temperature of $T_0 \approx 2.725\text{K}$. This property indicates that the CMB is in thermal equilibrium. Given that the photons of the CMB have been travelling unimpeded since the time of decoupling, prior to which the mean free path of photons was very short, this observation is puzzling. Even regions of the CMB which appear close together should not have interacted at all prior to decoupling. So how was thermal equilibrium established? Again, this is explained by inflation, since by this mechanism, any small region in thermal equilibrium prior to inflation would have blown up to such an extent that its photons were driven out of causal contact. Whilst the resultant segregated regions would subsequently evolve independently, this evolution would be heavily influenced by initial conditions, which each region shares.

Now a widely accepted phenomenon, inflation was first proposed by Alan Guth in 1981 [4]. Whilst the details of inflation are unresolved, most theories agree that inflation was driven by a scalar field known as the inflaton. The consensus is that the universe cooled after the Big Bang, then underwent a period of accelerated expansion, and as a result

reheated, before gradually cooling again to its current temperature. Guth postulated that inflation was a first order phase transition, as introduced in detail in Section 1.2. He proposed that during its initial cooling period, the universe found itself in a metastable state, where it supercooled, bound by a potential barrier. Slowly, local regions tunnelled through the barrier and found their way into a stable state via bubble nucleation. These bubbles expanded rapidly, generating radiation as they collided, causing the universe to reheat. However, Guth’s original model required the rate of bubble nucleation to be low; too low to account for the volume of collisions needed to sufficiently reheat the universe [5]. Thus, modifications proved necessary, and a year later, Andrei Linde [6] and the group of Andreas Albrecht and Paul Steinhardt [7] independently arrived at the same solution, following the groundwork of Stephen Hawking and Ian Moss [8]. They suggested that instead of tunneling through a barrier, the inflaton rolled slowly down its potential. This gradual change in phase mimics the low nucleation rate of Guth inflation, but the alteration in potential geometry allows enough radiation to be generated to sufficiently reheat the universe. This higher order transition is known as slow-roll inflation, or new inflation, with Guth inflation relabelled as old inflation.

1.1.2 Electroweak Symmetry Breaking

In the present universe, the electromagnetic force and the weak force are seemingly distinct. The prior has infinite range, whereas the latter acts only over distances of around 10^{-18}m , and the prior is notably stronger. Furthermore, the electromagnetic force acts via massless photons, whereas the weak interaction occurs by means of massive W^\pm and Z bosons. However, at energies above around 160GeV, these forces become indistinguishable, and are thus relabeled as the electroweak force. The process by which these forces diverged is known as the electroweak phase transition, which is thought to have occurred around one nanosecond after the Big Bang [9].

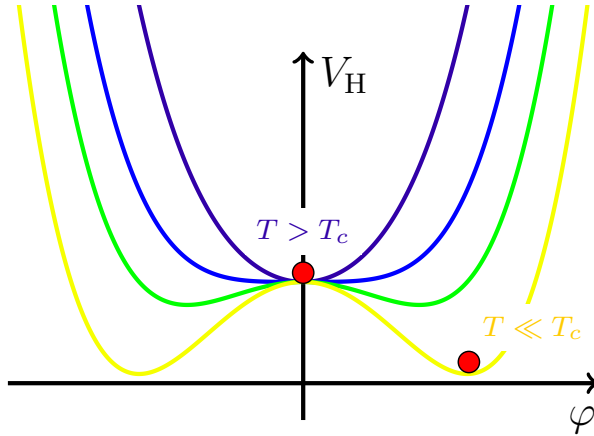


Figure 1.1: A schematic showing the nature of a second-order electroweak phase transition. Above some critical temperature, T_c , the Higgs potential, $V_H(\varphi)$, possesses a single minimum, about which $V_H(\varphi)$ is symmetric. The geometry of $V_H(\varphi)$ deforms as the universe cools. Below T_c , the midpoint of $V_H(\varphi)$ becomes a local maximum and $V_H(\varphi)$ gains degenerate minima, about which $V_H(\varphi)$ is not symmetric. The Higgs field, φ , rolls smoothly from the symmetric phase into either minima.

This transition can be attributed to the symmetry breaking of the Higgs potential. The Higgs field, φ , is scalar, with temperature-dependent potential V_H . According to the Standard Model, Higgs decay was a second order transition, as sketched in Figure 1.1. In this description, above some critical temperature, T_C , the Higgs potential exhibits a single minimum, at $\varphi = 0$, about which the potential is symmetric. In this symmetric phase, W^\pm and Z bosons are massless, and so behave in the same manner as photons. However, below T_C , the coordinate $\varphi = 0$ becomes a local maximum and V_H develops degenerate local minima. The Higgs field is not symmetric about any such minimum. Thus, as the universe cooled and rolled from $\varphi = 0$ into a new minimum, the symmetry of the Higgs field was broken. In the broken-symmetry phase, W^\pm and Z bosons have mass, and so act differently to photons. Hence, the weak force differentiated from the electromagnetic force. According to the Standard Model, the universe rolled smoothly down V_H as it cooled, by means of thermal fluctuations, preserving local thermal equilibrium.

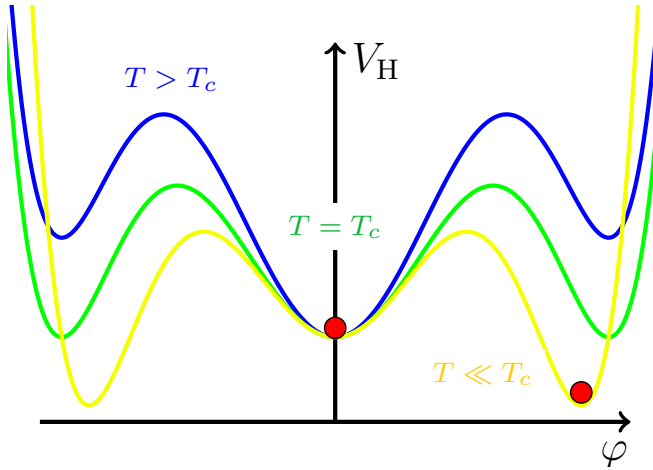


Figure 1.2: A schematic showing the nature of a first-order electroweak phase transition. In contrast to the second-order prescription of Figure 1.1, here V_H has sizeable potential barriers and consequently, additional minima. Above some critical temperature, T_c , the Higgs field remains settled in the global minimum at $\varphi = 0$. As temperature lowers below T_c , the nature of the minima swap, rendering the symmetric phase metastable. The field then tunnels through the barrier, into a new global minimum.

However, the Standard Model is incomplete, and just as there was a need to incorporate inflation, some mysteries of the early universe can be accounted for if we allow for modifications in the geometry of V_H . One such possibility is that the Higgs field possesses notable potential barriers, as shown in Figure 1.2. These barriers create additional minima. Above T_c , the global minimum remains at $\varphi = 0$ and the additional minima are inconsequential. However, as the universe cooled, the energy of the broken-symmetric phases lowered, until it succeeded that of the symmetric phase. Thermal fluctuations were insufficient to overcome the potential barriers. Thus, the field instead tunneled through the barrier, undergoing a first order phase transition, as described in detail in Section 1.2. Such a transition would cause an abrupt change in the state of the universe, breaking thermal equilibrium. In contrast to a second-order transition, this would have significant observational consequences, and could potentially account for a number of mysteries of the early universe, including baryon asymmetry, primordial black holes [5, 10, 11], and the generation of gravitational waves [12–15] and magnetic fields. The prior is elaborated on in Section 1.1.3.

1.1.3 Baryogenesis

Baryogenesis is the process responsible for the imbalance of matter and anti-matter in the observable universe. This is known as the baryon asymmetry problem. The baryon

number of a system is given by

$$B = \frac{1}{3}(n_q - n_{\tilde{q}}), \quad (1.1)$$

where n_q is the number of quarks and $n_{\tilde{q}}$ is the number of anti-quarks. In the present universe, baryon number is conserved; in any interaction, baryons and anti-baryons are created or destroyed in equal quantities. Therefore, it is not outrageous to postulate that baryons and anti-baryons were created in equal quantities in the first place. But then we would expect the matter and anti-matter to have annihilated, leaving behind empty space. Given that matter makes up 30% of our universe, something is clearly amiss. Either the universe began with less anti-matter, or interactions took place later which preferentially created matter. Neither possibility is understood, but physicists favour the latter.

In 1967, Andrei Sakharov deduced three conditions which must be satisfied for the universe to be able to synthesize matter and anti-matter at unequal rates:

1. Baryon number violation.
2. C and CP violation.
3. Departure from thermal equilibrium.

These are the Sakharov conditions [16]. The first condition is a given; an existing symmetry in the baryon to anti-baryon ratio cannot be broken unless some interaction exists for which baryon number is not conserved. Charge conjugation (C) violation is also necessary, otherwise interactions which produce an excess of baryons would be cancelled out by interactions which produce an excess of anti-baryons. However, if C-symmetry is broken but charge conjugation parity (CP) symmetry is not, baryon number conservation is still possible. Thus, CP-violation is required too. Finally, when a system is in thermal equilibrium, interactions take place at equal rates in both the forwards and backwards direction. If this condition held, any interaction which creates an asymmetry would be undone by its reverse reaction. Therefore, the universe could not have been in thermal equilibrium at the time of baryogenesis.

The nature and timing of baryogenesis is still up for debate, but one popular theory is that the baryon asymmetry of the universe arose as a result of the electroweak phase transition [17]. At high temperatures, the electroweak field equations possess a class of static, non-perturbative solutions known as sphalerons. Provided that the electroweak phase transition was first-order, local-departures from thermal equilibrium would have arisen during this epoch. Any net increase in baryon number arising from sphaleron processes would then have been able to persist in such regions.

1.1.4 Quark-Hadron Transition

Whilst the foundations of baryon-asymmetry were laid during the electroweak epoch, the universe was too hot at this time for baryons to form. Instead, the universe was filled with quark-gluon plasma. Then, at around 10^{-5} seconds after the Big Bang, quarks bound to form hadrons. Subsequent fluctuations in Baryon number indicate that this transition may also have been first-order [18], although lattice gauge theory simulations suggest otherwise [19].

1.2 Vacuum Decay

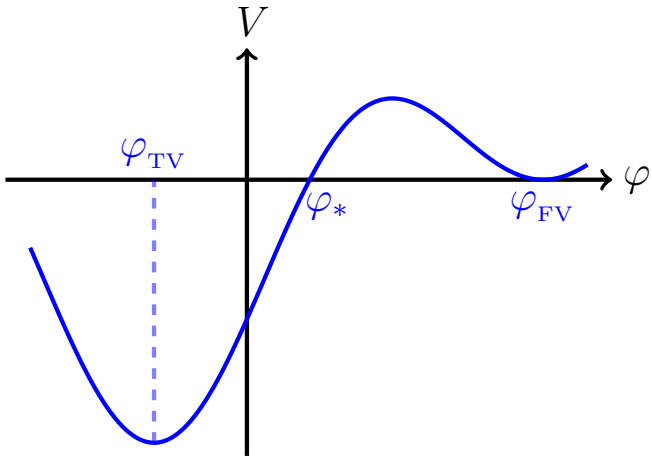


Figure 1.3: The typical potential, V , of a scalar field, φ , that is susceptible to vacuum decay. The potential possesses a local minimum, φ_{FV} , known as the false vacuum state, and a global minimum, φ_{TV} , known as the true vacuum state. The additional coordinate for which $V = V(\varphi_{\text{FV}})$, which we label φ_* , is known as the escape point.

Consider a scalar field, $\varphi(t, \mathbf{x})$, with potential $V(\varphi)$ as shown in Figure 1.3. The potential exhibits two minima, one global and one local, separated by a potential barrier. Classically, both minima are stable; if the field finds itself in either minimum it cannot escape. However, quantum effects render this story incomplete. In the quantum realm, the global minimum remains stable. The same cannot be said for the local minimum; the field may settle in this state for some time, but eventually quantum fluctuations send the field through the potential barrier and into the global minimum. Consequently, we refer to the metastable local minimum as the false vacuum state, and the stable global minimum as the true vacuum state. We label these as φ_{FV} and φ_{TV} , respectively, and the escape point of the potential barrier as φ_* . This quantum tunneling process is known as false vacuum decay.

False vacuum decay may also occur via thermal means. If the size of a thermal fluctuation exceeds the height of the potential barrier, the field may hop over the barrier and fall into the true vacuum state, instead of tunnelling through. Strangely, this process may still be examined using quantum-tunneling techniques, as discussed in the subsequent section.

In this thesis, we are primarily interested in first-order vacuum decay. In the context of cosmology, such a phase transition proceeds as follows. A small region of the universe, or some analogous system, finds itself in the true vacuum state, either by quantum or thermal means. Typically, the surrounding false vacuum dominates and the bubble swiftly shrinks to nothing. However, should the initial bubble of true vacuum be large enough, it is energetically favourable for it to grow. As a result, it expands outwards at the speed of light, gradually consuming the entirety of space. A schematic of such a phase transition is shown in Figure 1.4.

First order false vacuum decay would give rise to violent density fluctuations, which would have echoes in the present day universe, in the form of signals in the cosmic microwave background [20]. Furthermore, multiple bubbles of true vacuum may nucleate throughout a system. Given enough time, they will collide, emitting energy as they do so. It is possible that this energy is responsible for the production of gravitational waves [12–15] and primordial black holes [5, 10, 11] in the early universe.

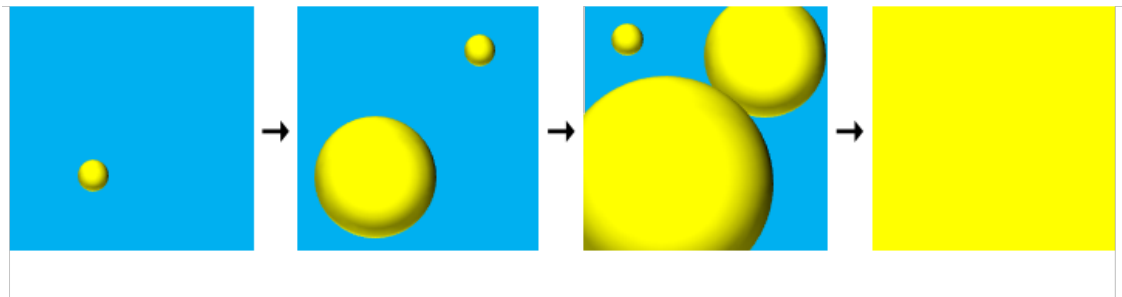


Figure 1.4: A schematic of first-order vacuum decay. Initially, all of space is in the false vacuum state (blue). A bubble of true vacuum (yellow) forms and expands. Multiple such bubbles may nucleate over time, which collide as they grow. The bubbles gradually consume the entirety of space, eventually resulting in a true-vacuum universe.

1.2.1 The Coleman Instanton

An instanton is a classical solution to the equations of motion of a quantum system, obtained by moving to Euclidean spacetime [21, 22]. Instantons allow us to approximate quantum field theory calculations and are a particularly useful tool for tackling quantum tunneling problems.

In the famous papers “*Fate of the False Vacuum, I-II*” [23, 24], Coleman and Callan

use instanton methodology to examine the process of vacuum decay for the scalar field introduced in the previous section. In particular, they calculate an analytic expression for the rate of false vacuum decay, Γ , given by¹:

$$\Gamma \approx \mathcal{V} \left| \frac{\det' S''_E[\varphi_b]}{\det S''_E[\varphi_{\text{FV}}]} \right|^{-1/2} \left(\frac{S_E[\varphi_b]}{2\pi} \right)^{N/2} e^{-S_E[\varphi_b]}, \quad (1.2)$$

where \mathcal{V} is the volume of space considered. The quantities S_E and N will be defined momentarily. We do not wish to offend the authors of Ref. [24] by attempting to outline their sophisticated derivation of the above. Rather, we summarize the steps necessary to make use of Equation (1.2). Before proceeding, we note that this work was extended to account for gravitational effects in Ref. [25].

We begin with an action, S . For a scalar field in Minkowski space, with signature $(+, -, -, -)$, this is given by:

$$S[\varphi] = \int_{-\infty}^{\infty} dt d^3x \left\{ \frac{1}{2} \left(\frac{\partial \varphi}{\partial t} \right)^2 - \frac{1}{2} (\nabla \varphi)^2 - V(\varphi) \right\}, \quad (1.3)$$

where units have been chosen such that $c = 1$.

We then move to Euclidean spacetime, by introducing the imaginary time coordinate:

$$t = i\tau. \quad (1.4)$$

The Euclidean action, S_E , is subsequently defined such that:

$$S_E = iS[\varphi(\tau, \mathbf{x})]. \quad (1.5)$$

Hence, we find,

$$S_E[\varphi] = \int_{-\infty}^{\infty} d\tau d^3x \left\{ \frac{1}{2} \left(\frac{\partial \varphi}{\partial \tau} \right)^2 + \frac{1}{2} (\nabla \varphi)^2 + V(\varphi) \right\}. \quad (1.6)$$

From this, we obtain the Euclidean equation of motion:

$$\frac{\partial^2 \varphi}{\partial \tau^2} + \nabla^2 \varphi = V'(\varphi). \quad (1.7)$$

Notice that S_E is the functional which appears in Equation (1.2), alongside its second functional derivative, S''_E , and functional determinant. Here, \det' is used to denote taking

¹Technically, this is only true when $V(\varphi_{\text{FV}}) = 0$. However, since it is $V'(\varphi)$ which appears in the equation of motion - for example see Equation (1.7) - we are always free to shift V such that this holds.

the functional derivative of the argument whilst neglecting modes with eigenvalue zero, as detailed in Ref. [24]. zero-modes are instead accounted for by the contribution of $(S_E[\varphi_b]/(2\pi))^{N/2}$ which appears in Equation (1.2), where the exponent N is given by the number of zero-modes, as specified in Section 1.2.2.

Equation (1.2) requires us to evaluate S_E at the bounce² φ_b . This is the solution of Equation (1.7) which satisfies:

$$\lim_{|\mathbf{x}| \rightarrow \infty} \varphi_b(\tau, \mathbf{x}) = \varphi_{\text{FV}}. \quad (1.8)$$

Condition (1.8) is consistent with the definition of first-order vacuum decay; a bubble of true vacuum appears locally and expands, but far away from the bubble, the false vacuum state prevails. Practically, this condition ensures that $S_E[\varphi_b]$ is finite. Additional conditions hold, depending on whether we are considering quantum or thermal vacuum decay. We consider these cases separately.

Case 1: Quantum Vacuum Decay

If the false vacuum state decays via quantum fluctuations, the bounce must satisfy two additional conditions:

$$\frac{\partial \varphi_b}{\partial \tau}(0, \mathbf{x}) = 0, \quad (1.9)$$

and

$$\lim_{\tau \rightarrow \pm\infty} \varphi_b(\tau, \mathbf{x}) = \varphi_{\text{FV}}. \quad (1.10)$$

In words, these conditions tell us that the field begins in the false vacuum state, before tunneling through the potential barrier. Then at some point, which by time-translational invariance we are free to label as $\tau = 0$, the field turns around and heads back to the false vacuum; we say the field “bounces.”

Given the symmetry of Equation (1.7), we make the ansatz:

$$\varphi_b = \varphi_b(\rho), \quad (1.11)$$

where $\rho = \sqrt{\tau^2 + |\mathbf{x}|^2}$. The Euclidean action then reduces to:

$$S_E[\varphi_b] = 2\pi^2 \int_0^\infty \rho^3 d\rho \left\{ \frac{1}{2} \left(\frac{\partial \varphi_b}{\partial \rho} \right)^2 + V(\varphi_b) \right\}, \quad (1.12)$$

²For any given system, there may actually be multiple bounces with the same Euclidean action. For details on how to deal with this rigorously, see Refs. [23, 24]. In practice, we need not worry; the prefactor of Equation (1.21) takes care of this possibility.

and the equation of motion transforms accordingly:

$$\frac{\partial^2 \varphi_b}{\partial \rho^2} + \frac{3}{\rho} \frac{\partial \varphi_b}{\partial \rho} = V'(\varphi_b). \quad (1.13)$$

Conditions (1.8) and (1.10) combine to give:

$$\lim_{\rho \rightarrow \infty} \varphi_b(\rho) = \varphi_{\text{FV}}. \quad (1.14)$$

Case 2: Thermal Vacuum Decay

Interestingly, whilst a thermal system leaps the potential barrier, the corresponding instanton still tunnels beneath it, as for a zero temperature system. If the false vacuum state decays via a purely thermal transition, then:

$$\frac{\partial \varphi_b}{\partial \tau} = 0, \quad (1.15)$$

and the Euclidean action simplifies to:

$$S_E[\varphi_b] = \beta \int_{-\infty}^{\infty} d^3x \left\{ \frac{1}{2} (\nabla \varphi_b)^2 + V(\varphi_b) \right\}, \quad (1.16)$$

where $\beta = 1/T$ [26]. Similarly to quantum case, we make the ansatz:

$$\varphi_b = \varphi_b(r), \quad (1.17)$$

where $r = |\mathbf{x}|$. Then, the Euclidean action and equation of motion become:

$$S_E[\varphi_b] = 4\pi\beta \int_0^{\infty} r^2 dr \left\{ \frac{1}{2} \left(\frac{\partial \varphi_b}{\partial r} \right)^2 + V(\varphi_b) \right\}, \quad (1.18)$$

and

$$\frac{\partial^2 \varphi_b}{\partial r^2} + \frac{2}{r} \frac{\partial \varphi_b}{\partial r} = V'(\varphi_b). \quad (1.19)$$

Finally, condition 1.8 becomes:

$$\lim_{r \rightarrow \infty} \varphi_b(r) = \varphi_{\text{FV}}. \quad (1.20)$$

In either case, given a specific potential V , we are ready to solve for φ_b . In general, this can only be achieved numerically, as in Ref. [27], although analytic solutions exist in some limits [23, 24].

1.2.2 A Practical Solution

From the previous section, it is clear that calculating the rate of false vacuum decay, Γ , rigorously via Equation (1.2) is an incredibly involved process. In practice, when comparing Coleman's predictions to numerical results, it often suffices to use:

$$\Gamma = A \left(S_E[\varphi_b] \right)^{N/2} e^{-S_E[\varphi_b]}, \quad (1.21)$$

with A left as a free parameter, determined by fitting Equation (1.21) to the available data.

Let n be the number of spatial dimensions of the scalar field under consideration. It turns out that the number of zero-modes, N , obeys the following prescription:

$$N = \begin{cases} n, & \text{if vacuum decay is a thermal process,} \\ n + 1, & \text{if vacuum decay is a quantum process.} \end{cases} \quad (1.22)$$

We make use of this simplified methodology throughout this thesis.

1.3 Quantum Simulators of Fundamental Physics

1.3.1 The Limitations of Observations

Despite many remarkable advances in technology over the last century, we are unable to view the early universe. Observational surveys reveal much about the universe's evolution, with, for example, the James Webb Space Telescope hoping to show the formation of the first stars and galaxies, 100 million years after the Big Bang [28]. However, the earliest epoch we can image is that of photon decoupling, around 10^{13} years after the Big Bang, when photons began travelling unimpeded to form what we now detect as the cosmic-microwave background (CMB). Whilst the COBE, WMAP and Planck surveys [29, 30] produced ever-crisper images of the CMB, accompanied by an ever-deeper understanding of the universe at this time, we are unable to rewind any further. We remain, quite literally, in the dark, when it comes to the phase transitions discussed in Sections 1.1-1.2.

1.3.2 Analogue Systems

Instead, we may make use of analogue systems. Such systems need not replicate the exact conditions of the event under consideration; indeed we cannot hope to recreate the early universe itself in a laboratory. For example, as we will soon see, it is possible to simulate

the very hot with the very cold. Rather, analogue systems need only capture the key features of the problem at hand.

The first such system was proposed by Bill Unruh in the 1981 paper “*Experimental Black-Hole Evaporation?*” [31]. This work draws analogy between the event horizon of a black hole and the sonic horizons of a transonic fluid flow. Following the lines of Hawking’s original paper, Unruh showed that like a rotating black hole, sonic horizons should emit thermal radiation, in the form of sound waves. Much like the early universe, the centre of a black hole is unobservable, whereas a laboratory fluid is highly probeable. Thus, Unruh predicted that such a flow could provide a new insight into Hawking radiation. Unfortunately, Unruh found the analogue Hawking temperature to be around 10^{-7}K ; colder than any fluid at hand in 1981.

Fortunately, the creation of Bose-Einstein condensates at the turn of the century, as detailed in Section 1.4, rendered fluid temperatures of this magnitude attainable. In 2007, Jain *et al.* [32] suggested using a toroidally trapped BEC with a pair of de Laval nozzles to observe analogue Hawking radiation. However, this phenomenon was first observed experimentally by Steinhauer in 2014 [33, 34], and instead made use of a potential step. A deeper numerical analysis of this scenario followed in 2017 [35]. Many other analogue models of Hawking radiation have been proposed, as summarised in Ref. [36], alongside analogues to test additional ideas in perturbative quantum field theory, such as superradiance and cosmological particle production. Analogue systems have also been used to model the expanding universe [37] and boson star formation [38].

1.3.3 False Vacuum Decay

Whilst we cannot directly observe the progression of early-universe vacuum decay, we are able to observe relativistic vacuum decay in cold-atom systems. By examining first-order decay in the laboratory, we are able to infer the consequences and likelihood of first-order decay in the early universe. The first such experiment was proposed by Fialko *et al.* in 2015 [39]. In this work, following the famous methodology for the stabilisation of the inverted Kapitza pendulum [40], Fialko *et al.* construct a metastable state in the relative phase of a two-component cold atom system coupled by a modulated microwave field. Here, the sound speed is analogous to the speed of light. They perform zero-temperature simulations of systems with one to three spatial dimensions and successfully observe relativistic bubble nucleation in all. A more comprehensive study of the feasibility of such experiments followed in 2017 [41], sparking increased interest in this research area. The progress to date is summarized in the following timeline:

- 2019 • Braden *et al.* [42–44] found that at zero temperature, the oscillatory potential of Fialko *et al.* induces a parametric instability at short wavelengths, which causes the false vacuum state to decay by classical means. They postulated that thermal effects could damp out the instability. Hertzberg *et al.* refined this methodology in Ref. [45].
- The question was raised as to whether bubbles would nucleate at a fast enough rate to be observed in experiments, given the limited lifespan of Bose-gases. Billam *et al.* [46] showed that the nucleation process can be accelerated, by imprinting phase defects into the system, which seed vacuum decay.
- 2020 • Abed & Moss [27] calculated the theoretical instanton decay rate for both zero and finite temperature systems with a range of spatial dimensions.
- The investigations of this thesis began. Billam *et al.* [47] incorporated finite temperature effects into the one-dimensional, two-component system with static interaction potential, as detailed in Chapter 2. This work primarily focused on the rate of false vacuum decay. Meanwhile, Ng *et al.* [48] made use of a contrasting finite-temperature approach to examine the phase entropy of this system.
- 2021 • Billam *et al.* [49] applied their finite-temperature methodology to the full oscillatory potential, and investigated the role of damping, as detailed in Chapter 3. Uncertainty arose as to whether or not damping out the instability was feasible under realistic conditions.
- With this in mind, they began to investigate vacuum decay in an alternative system: a one-dimensional, three-component, spin-1 Bose gas at zero temperature [50], as detailed in Chapter 4.
- 2022 • Pirvu *et al.* [51] examined the clustering of bubbles in the one-dimensional, zero-temperature system, and found bubble nucleation sites to be correlated.
- From the research efforts thus far, it became clear that renormalization effects were occurring, whereby the inputted potential varies from the potential “seen” by particles. Braden *et al.* [52] undertook an in-depth investigation into these effects.

- Billam *et al.* [53] extended their spin-1 investigations to a two-dimensional system at finite temperature, as detailed in Chapter 5. They went on to explore boundary effects.
- 2023 The first experimental observation of relativistic bubble nucleation was made by Zenesini *et al.* [54] in Trento.
- In preparation for upcoming experiments at the Cavendish Laboratory in Cambridge, Jenkins *et al.* [55] improved the initialization protocol of simulations of the two-component system at zero temperature. This involved correcting the conventionally-used initial white noise to accurately reflect the Bogoliubov (see Section 1.6.2) power-spectrum.

1.3.4 QSimFP Consortium

The progress detailed above spans just one branch of a greater research effort. The majority of this work was carried out as part of the Quantum Simulators for Fundamental Physics (QSimFP) consortium³; a UK based collaboration involving seven native research institutes, alongside a number of international partners. With four experimental facilities across the country, this consortium aims to build a number of analogue systems. The collective aim of this partnership is to investigate both early-universe processes, such as vacuum decay, as well as the evolution of black holes.

1.4 Bose-Einstein Condensation

Here, we give a brief introduction to Bose-Einstein condensation for the cosmologists' benefit. The expert reader may opt to skip this section, or enjoy a refresher.

1.4.1 The Prediction of Bose-Einstein Condensation

At the end of the nineteenth century, the formulation of Planck's law [56] set the wheels of quantum theory in motion. In the two decades which followed, many attempts were made to produce a satisfactory derivation of this empirical formula. However, all combined ideas from both classical and quantum mechanics: two fields deemed generally incompatible. That was until 1924, when Satyendra Nath Bose arrived at Planck's law via statistical mechanics alone, by treating photons as a three-dimensional gas of identical particles [57]. Bose sent his work to Einstein, who, impressed, translated his findings to German and

³<https://qsimfp.org/>

facilitated their publication.

Einstein explored Bose's ideas further and applied them to a three-dimensional gas of non-interacting, massive bosons. He showed that in the micro-canonical picture, for which the total number of particles and total energy of the gas is conserved, the average number of particles of energy ϵ_i in the system follows the Bose-Einstein distribution [58, 59]:

$$n_i(\epsilon_i) = \frac{1}{e^{(\epsilon_i - \mu)/(k_B T)} - 1}, \quad (1.23)$$

where $\mu < 0$ is the chemical potential, T is temperature, and k_B is Boltzmann's constant. In Einstein's derivation, the quantities μ and T appear as Lagrange multipliers [60]. However, Equation (1.23) can also be derived more directly in the grand-canonical picture, where the total particle number and total energy may vary. The average particle density can be found by integrating n_i :

$$n = \int n_i(\epsilon_i) d\epsilon_i. \quad (1.24)$$

An examination of formula (1.23) led Einstein to conjecture that below the critical temperature,

$$T_c = \frac{2\pi\hbar^2}{mk_B} \left(\frac{n}{\zeta(3/2)} \right)^{2/3}, \quad (1.25)$$

where $\zeta(3/2) \approx 2.612$ is the Riemann zeta function, three-dimensional, untrapped, ideal bosonic gases undergo a phase transition, characterised by the sudden macroscopic occupation of their ground state. The prediction of this phenomenon, known as Bose-Einstein condensation, foretold of an exciting window into the realm of quantum mechanics, should cold enough temperatures ever be reached for such a phase to be realised.

1.4.2 What is Bose-Einstein Condensation?

Unlike fermions, bosons are free to cohabit. Thus as we cool an ideal gas of bosons towards absolute zero, particles flock towards the lowest energy modes. Below the critical temperature, T_c , we find a macroscopic occupation of the system's ground state, as shown in Figure 1.5. Meanwhile, the de-Broglie wavelength [61] increases:

$$\lambda_{dB} \sim T^{-1/2}. \quad (1.26)$$

This quantifies the wave-like behaviour of matter; at high temperatures λ_{dB} is minuscule, and so individual particles are highly distinguishable. Below T_c however, λ_{dB} grows much larger than the mean inter-particle distance, as shown in Figure 1.6. The ensemble of wavepackets overlap to such an extent that individual particles cannot be identified, and the ground state bosons behave as one entity, described by a single wavefunction. This is

Bose-Einstein condensation.

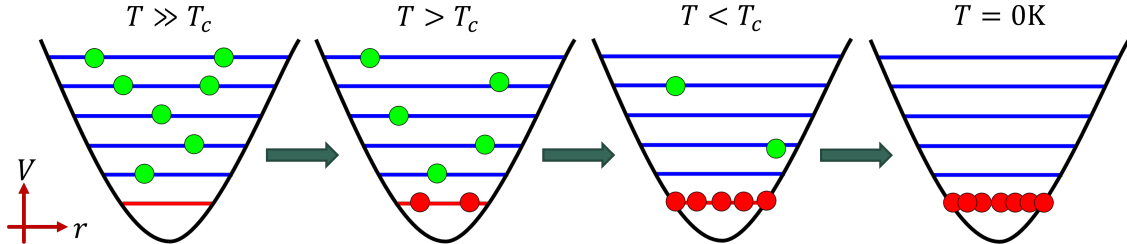


Figure 1.5: A schematic demonstrating the process of Bose-Einstein condensation in an ideal gas. Here, particles are confined to some potential, V . The horizontal lines represent the modes of the system, with red used to highlight the ground state. At high temperatures, many modes are populated. As the system cools, particles navigate towards the lower energy modes. Below some critical temperature, T_c , particles begin to rapidly accumulate in the ground state.

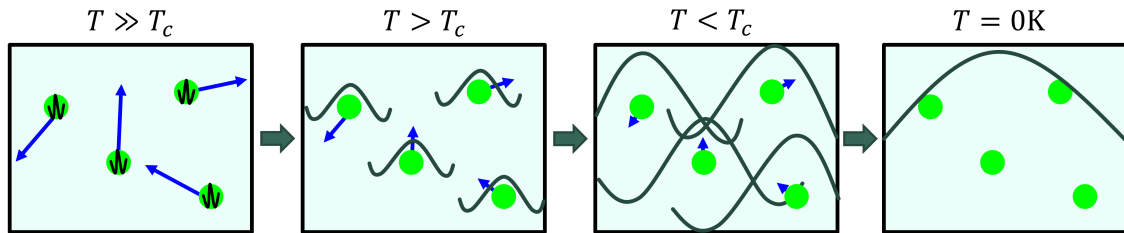


Figure 1.6: A schematic demonstrating the wave-like behaviour of matter. An ensemble of particles is shown over a range of temperatures, with the de-Broglie wavelength, λ_{dB} , superimposed in black, and velocity indicated with a blue arrow. At high temperatures, the particle-like behaviour of matter dominates. However, as we cool, λ_{dB} grows and the wave-like behaviour becomes apparent. As we cool towards 0K, the matter waves grow and overlap to such an extent that all particles behave as one entity.

Einstein predicted the condensation of an ideal gas. However, such a gas takes infinite time to reach thermal equilibrium. Thus, in practice, a weakly interacting gas is required. Incorporating interactions causes a shift in the condensate temperature, T_c , away from Equation (1.25). The direction of the shift depends on the geometry of the trap used to confine the condensate, but for a uniform system, T_c increases with interaction strength [62].

1.4.3 The First Bose-Einstein Condensate

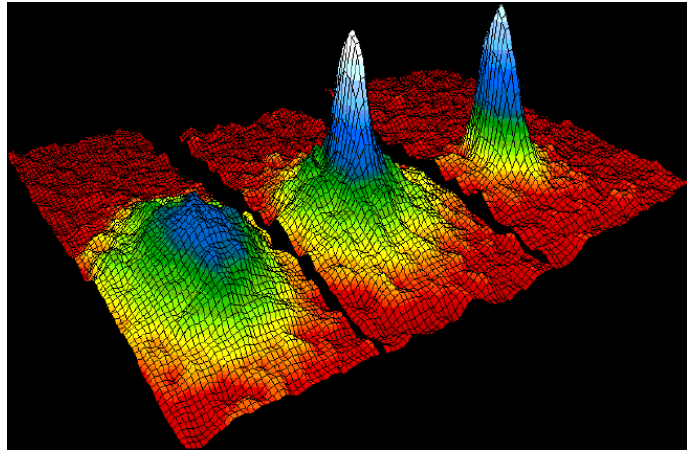


Figure 1.7: The first realisation of Bose-Einstein condensation. Here, the velocity distribution of a gas of ^{87}Rb atoms is shown at three temperatures. Colour indicates density, with red-orange corresponding to low density regions and blue-white corresponding to high density regions. Left: $T > T_c$ - there is notable spread in the velocity distribution. Centre: $T \lesssim T_c$ - there is a sudden macroscopic occupation of the lowest momentum modes. Right: $T < T_c$ - the velocity distribution tightens, as the condensate grows. (Image originally from the cover of Ref. [63]. This image is in the public domain.)

Cooling a dilute gas towards absolute zero is no easy feat, thus Bose-Einstein condensation remained a pipedream for much of the 20th century. However, alongside ever-advancing magnetic trapping technologies, the development of laser cooling techniques in the mid-1970s changed the game [64–66]. In 1995, through a combination of laser and evaporative cooling, the group of Eric Cornell and Carl Wieman achieved Bose-Einstein condensation in a harmonically trapped gas of ^{87}Rb atoms [63], as shown in Figure 1.7. Shortly after this initial success, the group of Wolfgang Ketterle realized Bose-Einstein condensation in a gas of ^{23}Na atoms [67]. In 2001, Cornell, Wieman and Ketterle were awarded the Nobel Prize in Physics for their pioneering efforts. Nowadays, Bose-Einstein condensation has been achieved using many different atomic species, and many laboratories across the globe produce condensates routinely. Condensates can now be controlled and measured with high precision, and so make an ideal analogue system, as discussed in Section 1.3.2.

1.4.4 Quasi Condensation

A true Bose-Einstein condensate, signified by the macroscopic occupation of a single state, is both density and phase coherent. In practical terms, this means that fluctuations in density and phase are minimal, and so density and phase are each highly spatially correlated. Theory dictates that for an infinite, uniform system, phase coherence may only be

achieved in a three-dimensional gas, or a two-dimensional gas at absolute zero. In practice, Bose-gases are not infinite, nor necessarily homogeneous; they are confined by magnetic and optical fields within some small experimental cavity. Thus, phase coherent states have been realised even in one-dimensional systems [68], just at much lower temperatures than the typical condensate temperature of Equation (1.25).

Quasi-condensates on the other hand can be more easily produced in reduced dimensional systems [68] and have proven to be versatile mediums for probing many-body quantum dynamics [69–72]. Such density coherent gases are similar to true condensates, but are not phase coherent and extend to modes neighbouring the ground state. The exact temperature at which quasi-condensation occurs varies with trap geometry and the extent of interactions, but in general, one-dimensional quasi-condensates form in the vicinity of [68, 73–75]:

$$T_{Q1} = \frac{\hbar c \rho_0}{k_B}, \quad (1.27)$$

where c is the sound speed of the condensate and ρ_0 is the particle density, and in two-dimensional systems:

$$T_{Q2} = \frac{2\pi\rho_0\hbar^2}{mk_B} \ln\left(\frac{\mathcal{C}\hbar^2}{mg_{2D}}\right), \quad (1.28)$$

where g_{2D} is the two-dimensional interaction strength, derived in Appendix A, and $\mathcal{C} = 380 \pm 3$ is a dimensionless constant [76].

The above temperature thresholds are only approximate. Thus in practice, in order to ensure the quasi-condensate regime has been reached, it is advisable to work well below T_Q . Throughout this thesis, we always consider temperatures at least one order of magnitude below T_Q .

1.5 Spin

1.5.1 Angular Momentum Formalism

Let $\mathbf{O} = (O_x, O_y, O_z)$ denote some angular momentum operator which satisfies the fundamental commutation relations:

$$[O_x, O_y] = i\hbar O_z, \quad [O_y, O_z] = i\hbar O_x, \quad [O_z, O_x] = i\hbar O_y. \quad (1.29)$$

It then follows that $O^2 = \mathbf{O} \cdot \mathbf{O}$ is compatible with each component of \mathbf{O} :

$$[O^2, \mathbf{O}] = 0. \quad (1.30)$$

As a result, it is possible for simultaneous eigenstates of O^2 and any component of \mathbf{O} to exist. Without loss of generality, we consider the mutual eigenstates of O^2 and O_z . The eigenvalues of O^2 are given by:

$$\hbar^2 o(o+1), \quad \text{where } o = 0, 1/2, 1, 3/2, \dots, \quad (1.31)$$

and the eigenvalues of O_z are given by:

$$\hbar m_o, \quad \text{where } m_o = -o, -o+1, \dots, o-1, o. \quad (1.32)$$

Hence, the simultaneous eigenstates of O^2 and O_z are characterized by two quantum numbers; the primary quantum number, o , and the magnetic quantum number, m_o . Thus, we label the eigenstates $|o, m_o\rangle$.

The angular momentum of an atom is described using three such vector operators; the orbital angular momentum operator, \mathbf{L} , the electron spin operator, \mathbf{S} , and the nuclear spin operator, \mathbf{I} .

We may also construct the total electron angular momentum operator, $\mathbf{J} = \mathbf{L} + \mathbf{S}$, and the total angular momentum operator, $\mathbf{F} = \mathbf{I} + \mathbf{J}$, with eigenstates $|j, m_j\rangle$ and $|f, m_f\rangle$, respectively. Note that both operators themselves satisfy the commutation relations (1.29). For any given values of ℓ and s , the permitted values of j are:

$$j = \{|l-s|, |l-s|+1, \dots, l+s-1, l+s\}. \quad (1.33)$$

Similarly, for any given values of i and j , the permitted values of f are:

$$f = \{|i-j|, |i-j|+1, \dots, i+j-1, i+j\}. \quad (1.34)$$

The allowed values of m_j and m_f follow from Equation (1.32).

1.5.2 The Alkali Metals

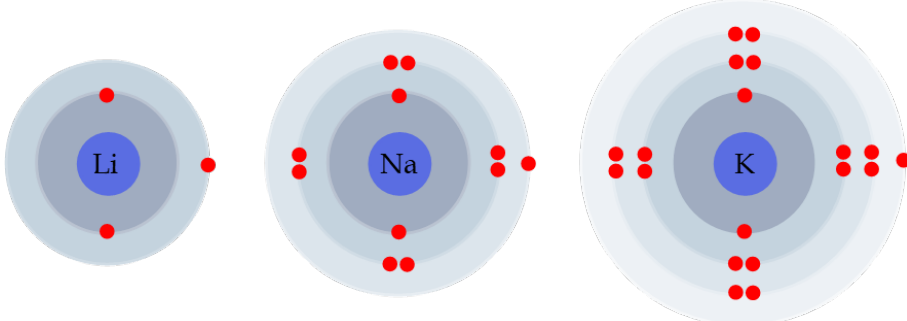


Figure 1.8: A schematic showing the electron configuration of the first three alkali metals: lithium (Li), sodium (Na) and potassium (K). Alkali atoms have a single electron in their outermost shell.

The investigations of this thesis make use of the alkali metals; a standard choice for ultracold gases, since alkali gases laser cool efficiently. This property arises due to the electron structure of such atoms. As shown in Figure 1.8, alkali atoms possess only a single valence electron. This characteristic is favourable, since it greatly simplifies the energy level structure under consideration.

The orbital angular momentum, L , of an alkali atoms is simply that of its valence electron. This orbits the nucleus in a spherically symmetric potential, $V(r)$. Thus, from the angular Schrödinger Equation [77], we know the angular motion of the outer electron to follow the spherical harmonics. In particular, this prevents ℓ from taking half integer values:

$$\ell = 0, 1, 2, \dots \quad (1.35)$$

Whilst ℓ varies with energy, and the nuclear spin quantum number, i , depends on the isotope under consideration, all alkali atoms have an electron spin quantum number of $s = 1/2$.

1.5.3 Energy Level Notation

The configuration of the electron spin, S , and the orbital angular momentum, L , of an atom can be described by the term symbol, $^{2s+1}\ell_j$. Note that the orbital component of the term is expressed not as a number, but as a capital letter, in line with spectroscopic conventions [78]:

$\ell =$	0	1	2	3	4	\dots
	S	P	D	F	G	

The investigations which follow predominantly consider the ground state manifold of alkali atoms, for which $\ell = 0$, $s = 1/2$, and consequently, $j = 1/2$. The term of interest is then $^2S_{1/2}$.

1.5.4 Hyperfine Structure

We must also consider the total nuclear spin, I , and subsequently, the total angular momentum, F . The nuclear angular momentum lifts the degeneracy between states with equal j but differing f , via the nuclear dipole Hamiltonian:

$$H_{\text{Dipole}} = A_{\text{HFS}} \mathbf{I} \cdot \mathbf{J}, \quad (1.36)$$

where the hyperfine structure constant, A_{HFS} , is measured experimentally. For a ground state alkali atom, this is the only intrinsic hyperfine effect. The energies of the resultant states satisfy:

$$E = \frac{1}{2} A_{\text{HFS}} [F(F+1) - I(I+1) - J(J+1)]. \quad (1.37)$$

1.5.5 The Zeeman Effect

In the presence of an external magnetic field, \mathbf{B} , the magnetic moment of an atom aligns preferentially with the applied field, giving rise to additional energy corrections. This is known as the Zeeman effect. Without loss of generality, we assume the magnetic field to be applied in the z -direction, $\mathbf{B} = B_z \hat{\mathbf{z}}$. Provided that the resultant energy corrections are small compared to fine-structure effects, this is described to leading order by the Hamiltonian:

$$H_{\text{Zeeman}} = g_J \mu_B J_z B_z, \quad (1.38)$$

where g_J is the Landé g -factor:

$$g_J = 1 + \frac{j(j+1) - \ell(\ell+1) + s(s+1)}{2j(j+1)}. \quad (1.39)$$

1.5.6 Breit-Rabi Diagrams

For any given term, we may visualise the Zeeman effect by plotting the eigen-energies of the hyperfine-Zeeman Hamiltonian, H_{HFSZ} , as a function of B_z . For a ground state alkali atom, this is given by:

$$H_{\text{HFSZ}} = H_{\text{Dipole}} + H_{\text{Zeeman}}, \quad (1.40)$$

where H_{Dipole} and H_{Zeeman} are given by Equations (1.36) and (1.38), respectively. The eigen-energies can be found by diagonalizing the matrix representation of H_{HFSZ} . The eigen-energies of Hydrogen are plotted as a function of B_z in Figure 1.9. This is known as a Breit-Rabi diagram. At low magnetic fields, where H_{Dipole} dominates, states group according to the value of F ; F is a good quantum number. However, as B_z increases, energy lines instead group according to the value of m_j ; F is no longer a good quantum number.

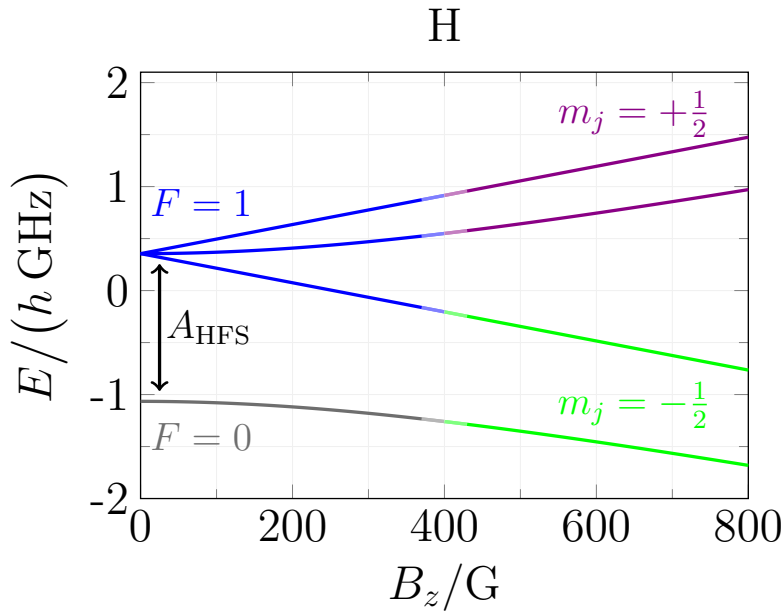


Figure 1.9: A Breit-Rabi diagram showing the Zeeman splitting of the ground state of hydrogen. For weak magnetic fields, states group according to F , whereas at stronger magnetic fields, states group according to m_j . In line with Equation (1.37), at zero magnetic field, $\Delta E_{\text{HFS}} = A_{\text{HFS}}$.

The investigations of Chapters 4-5 concern the $F = 1$ hyperfine ground state manifolds of ^{41}K and ^7Li . The corresponding Breit-Rabi diagrams are shown in Figure 1.10, with the $F = 2$ manifolds included for completeness. The nuclear spin, I , and hyperfine structure constant, A_{HFS} , are also tabulated for each species in Table 1.2.

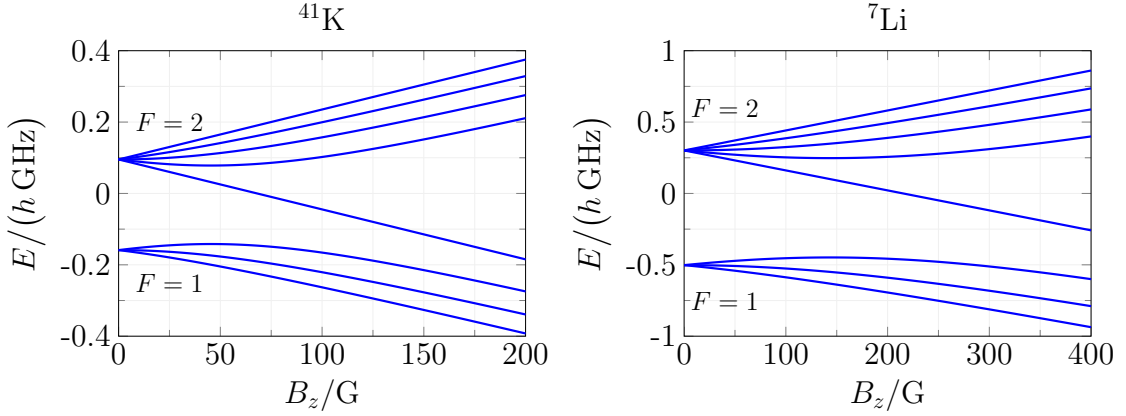


Figure 1.10: Breit-Rabi diagrams showing the Zeeman splitting of the ground states of potassium-41 and lithium-7. In line with Equation (1.37), at zero magnetic field, $\Delta E_{\text{HFS}} = 2A_{\text{HFS}}$.

Species	I	A_{HFS} [h MHz]
H	1/2	1420.405
^{41}K	3/2	127.007
^7Li	3/2	401.752

Table 1.2: The nuclear spin, I , and hyperfine structure constant, A_{HFS} , of alkali isotopes, obtained from Ref. [79].

In the low field regime, where F is a good quantum number, we may treat H_{Zeeman} as a perturbation of H_{Dipole} and approximate H_{HFSZ} , to quadratic order, by:

$$\tilde{H}_{\text{HFSZ}} = \hbar\omega_l F_z + \hbar\omega_q F_z^2, \quad (1.41)$$

where $\omega_l = \frac{g_F \mu_B B_z}{\hbar}$ and $\omega_q = -\frac{g_S^2 \mu_B^2 B_z^2}{\hbar A_{\text{HFS}} (1 + 2I)^2}$ (See Equation (25) of Ref. [80]). Here, $g_S \approx 2$ is the spin g -factor.

1.6 Modelling a Bose Gas

1.6.1 The Gross-Pitaevskii Equation

The theoretical description of a Bose gas may be constructed using the field operators, $\hat{\Psi}^\dagger(\mathbf{r}, t)$ and $\hat{\Psi}(\mathbf{r}, t)$, which respectively act to create or annihilate a single particle at

position \mathbf{r} and time t . They satisfy the equal-time commutation relations:

$$[\hat{\Psi}(\mathbf{r}, t), \hat{\Psi}^\dagger(\mathbf{r}', t)] = \delta(\mathbf{r} - \mathbf{r}'), \quad (1.42)$$

$$[\hat{\Psi}^\dagger(\mathbf{r}, t), \hat{\Psi}^\dagger(\mathbf{r}', t)] = [\hat{\Psi}(\mathbf{r}, t), \hat{\Psi}(\mathbf{r}', t)] = 0. \quad (1.43)$$

The Hamiltonian operator of an ultracold gas may then be expressed in terms of the field operators as follows [81]:

$$\hat{H} = \int d\mathbf{r} \hat{\Psi}^\dagger(\mathbf{r}, t) \hat{H}_0 \hat{\Psi}(\mathbf{r}, t) + \frac{1}{2} \int d\mathbf{r} d\mathbf{r}' \hat{\Psi}^\dagger(\mathbf{r}, t) \hat{\Psi}^\dagger(\mathbf{r}', t) V_{\text{int}}(\mathbf{r} - \mathbf{r}') \hat{\Psi}(\mathbf{r}', t) \hat{\Psi}(\mathbf{r}, t), \quad (1.44)$$

where,

$$\hat{H}_0 = -\frac{\hbar^2 \nabla^2}{2m} + V_{\text{trap}}(\mathbf{r}, t), \quad (1.45)$$

is the single particle Hamiltonian, and V_{trap} and V_{int} denote the external trapping potential and the internal two-body interaction potential, respectively.

At very cold temperatures, provided that the mean inter-particle distance is suitably large, it is reasonable to assume that interactions are well described by low-energy scattering processes. Then, the interaction potential can be well approximated by the contact potential:

$$V_{\text{int}}(\mathbf{r} - \mathbf{r}') \approx g\delta(\mathbf{r} - \mathbf{r}'), \quad (1.46)$$

where the prefactor $g = 4\pi\hbar^2 a_s/m$ is the interaction strength, and a_s is the species-dependent s-wave scattering length. In this case, the Hamiltonian (1.44) reduces to:

$$\hat{H} = \int d\mathbf{r} \left\{ \hat{\Psi}^\dagger(\mathbf{r}, t) \hat{H}_0 \hat{\Psi}(\mathbf{r}, t) + \frac{g}{2} \hat{\Psi}^\dagger(\mathbf{r}, t) \hat{\Psi}^\dagger(\mathbf{r}', t) \hat{\Psi}(\mathbf{r}, t) \hat{\Psi}(\mathbf{r}', t) \right\}. \quad (1.47)$$

The majority of investigations in this thesis concern systems for which particle number and energy are not conserved. Thus, at this stage it is convenient to move from the microscopic Hamiltonian, \hat{H} , to the grand-canonical Hamiltonian:

$$\hat{K} = \hat{H} - \mu \hat{N}, \quad (1.48)$$

where $\hat{N} = \int d\mathbf{r} \hat{\Psi}^\dagger \hat{\Psi}$ is the number operator and μ is the chemical potential, which can be thought of as the energy required to add a particle to a system.

We may examine the behaviour of such a system by considering the Heisenberg equation of motion for $\hat{\Psi}$:

$$i\hbar \frac{\partial \hat{\Psi}(\mathbf{r}, t)}{\partial t} = [\hat{\Psi}(\mathbf{r}, t), \hat{K}]. \quad (1.49)$$

By taking advantage of relations (1.42)-(1.43), this simplifies to:

$$i\hbar \frac{\partial \hat{\Psi}(\mathbf{r}, t)}{\partial t} = \hat{H}_0 \hat{\Psi}(\mathbf{r}, t) + g \hat{\Psi}^\dagger(\mathbf{r}, t) \hat{\Psi}(\mathbf{r}, t) \hat{\Psi}(\mathbf{r}, t) - \mu \hat{\Psi}(\mathbf{r}, t). \quad (1.50)$$

As demonstrated in Figure 1.5, close to absolute zero, the majority of particles occupy the lowest energy modes and form a condensate. Thus, at such temperatures, we make the mean field approximation:

$$\hat{\Psi}(\mathbf{r}, t) \rightarrow \psi(\mathbf{r}, t), \quad (1.51)$$

where $\psi(\mathbf{r}, t) = \langle \hat{\Psi}(\mathbf{r}, t) \rangle$. Equation (1.50) transforms accordingly:

$$i\hbar \frac{\partial \psi(\mathbf{r}, t)}{\partial t} = \left[-\frac{\hbar^2 \nabla^2}{2m} + V_{\text{trap}}(\mathbf{r}, t) + g|\psi|^2 - \mu \right] \psi(\mathbf{r}, t). \quad (1.52)$$

The above is known as the Gross-Pitaevskii equation (GPE), named for the physicists Eugene Gross [82] and Lev Pitaevskii [83], who first made use of this approach in their independent studies of quantized vortices in 1961.

In the case of a static trapping potential, $V_{\text{trap}} = V_{\text{trap}}(\mathbf{r})$, stationary solutions of the GPE are permitted. These satisfy the time-independent GPE:

$$\left[-\frac{\hbar^2 \nabla^2}{2m} + V_{\text{trap}}(\mathbf{r}) + g|\psi|^2 - \mu \right] \psi(\mathbf{r}) = 0. \quad (1.53)$$

The above derivation of the GPE assumed a three-dimensional condensate. However, we may reduce the dimensions of the GPE so that it may be applied to a lower-dimensional condensate. The form of the GPE remains unchanged, but as shown in Appendix A, corrections must be made to the interaction strength, g , and chemical potential, μ .

1.6.2 Bogoliubov Expansion

The mean-field replacement $\hat{\Psi}(\mathbf{r}, t) \rightarrow \psi(\mathbf{r}, t)$ used to derive the GPE assumes all atoms to be in the ground state. However, in the presence of interactions, we expect some population of non-condensate modes, even at absolute zero, so it is often necessary to go beyond this classical approach. Diagonalizing the grand-canonical Hamiltonian, \hat{K} , is non-trivial and impractical, due to the interaction terms of Equation (1.47). Thus, the convention is to make the higher order, Bogoliubov approximation [84–86].

Here, the first step is to make the expansion:

$$\hat{\Psi}(\mathbf{r}, t) = \psi(\mathbf{r}) + \delta\hat{\psi}(\mathbf{r}, t), \quad (1.54)$$

where ψ is the usual ground state wavefunction, which we assume to be stationary, and $\delta\hat{\psi}$ accounts for fluctuations about the ground state. By substituting the above into Equation (1.48), we may express \hat{K} as follows:

$$\hat{K} = \sum_{j=0}^4 \hat{K}_j, \quad (1.55)$$

where $\hat{K}_j = \mathcal{O}(\delta\hat{\psi}^j)$. In particular,

$$\hat{K}_0 = \int d\mathbf{r} \left\{ \psi^* \hat{H}_0 \psi + \frac{g}{2} |\psi|^4 - \mu |\psi|^2 \right\}, \quad (1.56)$$

$$\hat{K}_1 = \int d\mathbf{r} \left\{ \delta\hat{\psi}^\dagger [\hat{H}_0 \psi + g|\psi|^2 \psi - \mu \psi] + [\hat{H}_0 \psi^* + g|\psi|^2 \psi^* - \mu \psi^*] \delta\hat{\psi} \right\}, \quad (1.57)$$

$$\hat{K}_2 = \int d\mathbf{r} \left\{ \delta\hat{\psi}^\dagger \hat{H}_0 \delta\hat{\psi} + \frac{g}{2} \psi^2 \delta\hat{\psi}^\dagger \delta\hat{\psi}^\dagger + \frac{g}{2} \psi^{*2} \delta\hat{\psi} \delta\hat{\psi} + (2g|\psi|^2 - \mu) \delta\hat{\psi}^\dagger \delta\hat{\psi} \right\}. \quad (1.58)$$

We neglect higher order corrections \hat{K}_3 and \hat{K}_4 . Given that ψ is stationary, and so obeys the time-independent GPE, it follows that $\hat{K}_1 = 0$. Thus, the dominant corrections to the mean-field approach lie in \hat{K}_2 .

Going forward, for simplicity we neglect V_{trap} and consider a finite sized box of volume V . At this stage, it is convenient to move to momentum space, for which:

$$\delta\hat{\psi} = \frac{1}{\sqrt{V}} \sum_{\mathbf{p} \neq 0} \hat{a}_{\mathbf{p}} e^{i\mathbf{p}\cdot\mathbf{r}/\hbar}, \quad \delta\hat{\psi}^\dagger = \frac{1}{\sqrt{V}} \sum_{\mathbf{p} \neq 0} \hat{a}_{\mathbf{p}}^\dagger e^{-i\mathbf{p}\cdot\mathbf{r}/\hbar}. \quad (1.59)$$

Here, $\hat{a}_{\mathbf{p}}^\dagger$ and $\hat{a}_{\mathbf{p}}$ are the creation and annihilation operators in momentum space, respectively, which obey the bosonic commutation relations:

$$[\hat{a}_{\mathbf{p}}, \hat{a}_{\mathbf{q}}^\dagger] = \delta_{\mathbf{p}, \mathbf{q}}, \quad (1.60)$$

$$[\hat{a}_{\mathbf{p}}, \hat{a}_{\mathbf{q}}] = [\hat{a}_{\mathbf{p}}^\dagger, \hat{a}_{\mathbf{q}}^\dagger] = 0. \quad (1.61)$$

Then, the integral (1.58) becomes:

$$\hat{K}_2 = \sum_{\mathbf{p} \neq 0} \left\{ \hat{a}_{\mathbf{p}}^\dagger \hat{a}_{\mathbf{p}} \mathcal{L}_p + \frac{g}{2} \psi^{*2} \hat{a}_{\mathbf{p}} \hat{a}_{-\mathbf{p}} + \frac{g}{2} \psi^2 \hat{a}_{\mathbf{p}}^\dagger \hat{a}_{-\mathbf{p}}^\dagger \right\}, \quad (1.62)$$

where,

$$\mathcal{L}_p = \frac{p^2}{2m} + 2g|\psi|^2 - \mu. \quad (1.63)$$

The goal is to diagonalize \hat{K}_2 . Thus, we expand $\hat{a}_{\mathbf{p}}$ and $\hat{a}_{\mathbf{p}}^\dagger$ in terms of quasi-particle

creation and annihilation operators $\hat{b}_{\mathbf{p}}$ and $\hat{b}_{\mathbf{p}}^\dagger$:

$$\hat{a}_{\mathbf{p}} = u_p \hat{b}_{\mathbf{p}} + v_p \hat{b}_{-\mathbf{p}}^\dagger, \quad \hat{a}_p^\dagger = u_p \hat{b}_{\mathbf{p}}^\dagger + v_p \hat{b}_{-\mathbf{p}}, \quad (1.64)$$

where for the uniform system in question, we may assume the quasi-particle amplitudes u_p and v_p to be real [85]. This is known as a Bogoliubov transformation. Furthermore, since ψ is time-independent, we may assume ψ to be real. The quasi-particle operators $\hat{b}_{\mathbf{p}}$ and $\hat{b}_{\mathbf{p}}^\dagger$ are themselves bosonic, and so must obey the commutation relations:

$$[\hat{b}_{\mathbf{p}}, \hat{b}_{\mathbf{q}}^\dagger] = \delta_{\mathbf{p}, \mathbf{q}}, \quad (1.65)$$

$$[\hat{b}_{\mathbf{p}}, \hat{b}_{\mathbf{q}}] = [\hat{b}_{\mathbf{p}}^\dagger, \hat{b}_{\mathbf{q}}^\dagger] = 0. \quad (1.66)$$

We may then express Equation (1.62) in terms of u and v as follows:

$$\begin{aligned} \hat{K}_2 = \sum_{\mathbf{p} \neq 0} & \left\{ \left(\mathcal{L}_p u_p^2 + g\psi^2 u_p v_p \right) \hat{b}_{\mathbf{p}}^\dagger \hat{b}_{\mathbf{p}} + \left(\mathcal{L}_p u_p v_p + \frac{g}{2}\psi^2 (u_p^2 + v_p^2) \right) \left[\hat{b}_{-\mathbf{p}} \hat{b}_{\mathbf{p}} + \hat{b}_{-\mathbf{p}}^\dagger \hat{b}_{\mathbf{p}}^\dagger \right] \right. \\ & \left. + \left(\mathcal{L}_p v_p^2 + g\psi^2 u_p v_p \right) \hat{b}_{\mathbf{p}} \hat{b}_{\mathbf{p}}^\dagger \right\}. \end{aligned} \quad (1.67)$$

In order for \hat{K}_2 to be diagonal, we require the off-diagonal coefficients to vanish:

$$\mathcal{L}_p u_p v_p + \frac{g}{2}\psi^2 (u_p^2 + v_p^2) = 0. \quad (1.68)$$

We go in search of such u_p and v_p . We may progress by returning to relation (1.65), which enforces the condition:

$$u_p^2 - v_p^2 = 1, \quad (1.69)$$

and so favors the ansatz:

$$u_p = \cosh(\alpha_p), \quad v_p = \sinh(\alpha_p), \quad (1.70)$$

for some real α_p . Substituting the above into Equation (1.68) and applying the hyperbolic double angle formulae yields:

$$\tanh(2\alpha_p) = -\frac{g\psi^2}{\mathcal{L}_p}. \quad (1.71)$$

Then, by applying the identity $1 - \tanh^2(x) = \operatorname{sech}^2(x)$ and making further use of the double angle formulae, we find:

$$u_p = \left(\frac{\mathcal{L}_p}{2\epsilon(p)} + \frac{1}{2} \right)^{1/2}, \quad v_p = -\left(\frac{\mathcal{L}_p}{2\epsilon(p)} - \frac{1}{2} \right)^{1/2}, \quad (1.72)$$

where,

$$\epsilon(p) = (\mathcal{L}_p^2 - g^2\psi^4)^{1/2}, \quad (1.73)$$

is the dispersion relation of the Bogoliubov modes. Consequently, Equation (1.67) reduces to:

$$\hat{K}_2 = \sum_{\mathbf{p} \neq \mathbf{0}} \left\{ (\mathcal{L}_p u_p^2 + g\psi^2 u_p v_p) \hat{b}_{\mathbf{p}}^\dagger \hat{b}_{\mathbf{p}} + (\mathcal{L}_p v_p^2 + g\psi^2 u_p v_p) \hat{b}_{\mathbf{p}} \hat{b}_{\mathbf{p}}^\dagger \right\}, \quad (1.74)$$

$$= \sum_{\mathbf{p} \neq \mathbf{0}} \left\{ (\mathcal{L}_p(u_p^2 + v_p^2) + 2g\psi^2 u_p v_p) \hat{b}_{\mathbf{p}}^\dagger \hat{b}_{\mathbf{p}} + (\mathcal{L}_p v_p^2 + g\psi^2 u_p v_p) \right\}. \quad (1.75)$$

The scalar term of Equation (1.75) may be absorbed into \hat{K}_0 , provided that \hat{K}_0 is then renormalized accordingly [86]. The quadratic contribution:

$$\hat{K}'_2 = \sum_{\mathbf{p} \neq \mathbf{0}} (\mathcal{L}_p(u_p^2 + v_p^2) + 2g\psi^2 u_p v_p) \hat{b}_{\mathbf{p}}^\dagger \hat{b}_{\mathbf{p}}, \quad (1.76)$$

remains. Upon inserting the full expressions for u_p and v_p , and rearranging, this becomes:

$$\hat{K}'_2 = \sum_{\mathbf{p} \neq \mathbf{0}} \epsilon(p) \hat{b}_{\mathbf{p}}^\dagger \hat{b}_{\mathbf{p}}. \quad (1.77)$$

We have successfully diagonalized the quadratic correction to the mean-field Hamiltonian and expressed the result in terms of independent, orthogonal quasi-particle modes with eigenenergies $\epsilon(p)$. The expected occupation of each Bogoliubov mode increases with temperature, following a Bose-Einstein distribution:

$$\bar{n}_{\mathbf{p}} = \langle \hat{b}_{\mathbf{p}}^\dagger \hat{b}_{\mathbf{p}} \rangle = \frac{1}{e^{\epsilon(p)/(k_B T)} - 1}. \quad (1.78)$$

1.6.3 Truncated-Wigner Approximation

With the Bogoliubov dispersion relation $\epsilon(p)$, as given by Equation (1.73), at our disposal, we are able to adapt our methodology to account for fluctuations about the condensate mode. We make the truncated-Wigner approximation (TWA), whereby the initial conditions of the GPE are replaced with an ensemble of stochastic initial conditions, sampled from an appropriate Wigner distribution [87, 88]. We then solve the GPE for each realisation and obtain key statistics by averaging over trajectories.

We may sample the Bogoliubov state by replacing the operators $\hat{b}_{\mathbf{p}}$ with random variables

$\beta_{\mathbf{p}}$, drawn from the Wigner distribution:

$$W_{\mathbf{p}}(\beta_{\mathbf{p}}, \beta_{\mathbf{p}}^*) = \frac{2}{\pi} \tanh\left(\frac{\epsilon(p)}{k_B T}\right) \exp\left[-2|\beta_{\mathbf{p}}|^2 \tanh\left(\frac{\epsilon(p)}{k_B T}\right)\right], \quad (1.79)$$

which have the properties:

$$\overline{\beta_{\mathbf{p}}} = \overline{\beta_{\mathbf{p}} \beta_{\mathbf{q}}} = 0, \quad \overline{\beta_{\mathbf{p}}^* \beta_{\mathbf{q}}} = \delta_{pq} \left(\overline{n}_{\mathbf{p}} + \frac{1}{2} \right). \quad (1.80)$$

Here, bars denote ensemble averaging, and $n_{\mathbf{p}}$ is the average mode occupation, as defined in Equation (1.78). In practice, we may obtain $\beta_{\mathbf{p}}$ more simply, by first drawing new variables $x_{\mathbf{p}}$ and $y_{\mathbf{p}}$ from the unit normal distribution, and constructing:

$$\beta_{\mathbf{p}} = \sqrt{\overline{n}_{\mathbf{p}} + 1/2} \left(\frac{x_{\mathbf{p}} + iy_{\mathbf{p}}}{\sqrt{2}} \right). \quad (1.81)$$

The truncated-Wigner initial conditions are then given, in terms of $\beta_{\mathbf{p}}$, by:

$$\psi(t=0) = \sqrt{N_0} + \sum_{\mathbf{p} \neq 0} [u_{\mathbf{p}} \beta_{\mathbf{p}} + v_{\mathbf{p}}^\dagger \beta_{\mathbf{p}}^*], \quad (1.82)$$

where u and v are the Bogoliubov coefficients and N_0 is the initial density of the condensate mode.

Interestingly, as we approach the zero-temperature limit, for which $\overline{n}_p \rightarrow 0$, we still expect some occupation of the Bogoliubov modes:

$$\lim_{T \rightarrow 0} \overline{|\beta_p|^2} = \frac{1}{2}. \quad (1.83)$$

This result will prove useful in Chapter 4, when we apply the truncated Wigner prescription to a zero-temperature spin-1 gas.

We propagate the initial state using the usual GPE, as given by Equation (1.52). However, now that we are populating modes beyond the ground state, care must be taken when solving the GPE numerically. In this thesis, all simulations make use of some periodic grid of size L in position space, divided into N lattice points. We then Fourier transform, carrying out integration algorithms in momentum space. Here, the non-linear interaction term of the GPE can cause problems, by populating modes outside of the grid range. This ghost population is then mapped back in range by the periodic boundary conditions, artificially altering the population of modes of interest. To avoid this aliasing effect, described in more detail in Appendix B.2 of Ref. [88], it proves necessary to incorporate

a projector, \mathcal{P} , into the GPE:

$$i\hbar \frac{\partial \psi(\mathbf{r}, t)}{\partial t} = \mathcal{P} \left\{ \left[-\frac{\hbar^2 \nabla^2}{2m} + V_{\text{trap}}(\mathbf{r}, t) + g|\psi|^2 - \mu \right] \psi(\mathbf{r}, t) \right\}. \quad (1.84)$$

This is known as the projected-GPE, or PGPE. In general a projector serves to eliminate modes above some cutoff, k_{cut} :

$$\mathcal{P} = \begin{cases} 1 & \text{if } |k| \leq k_{\text{cut}}, \\ 0 & \text{otherwise.} \end{cases} \quad (1.85)$$

Aliasing is prevented by taking:

$$k_{\text{cut}} = \frac{N\pi}{2L}. \quad (1.86)$$

It is important to keep this cut-off in mind when choosing grid parameters in the first place, since it acts to eliminate a significant portion of momentum space.

1.6.4 The Stochastic Projected GPE

The truncated-Wigner approximation applies to systems for which the majority of atoms lie in the ground state, but some sparse occupation of neighbouring modes is expected. Under such conditions, we are safe to assume that thermal modes have minimal influence on the condensate. However, as we go to higher temperatures, for which a range of modes are substantially occupied, it becomes necessary to include thermal effects. Here, we turn to the stochastic projected GPE (SPGPE) [88]:

$$i\hbar \frac{\partial \psi}{\partial t} = \mathcal{P} \left\{ (1 - i\gamma) \left[-\frac{\hbar^2 \nabla^2}{2m} + V_{\text{trap}} + g|\psi|^2 - \mu \right] \psi + \eta(\mathbf{r}, t) \right\}. \quad (1.87)$$

This closely resembles Equation (1.84), but includes two additional terms, which will be defined momentarily.

When using the SPGPE, which is widely used for modelling gases at and below the condensate temperature [88–95], we explicitly divide the system into a coherent region, comprising of all substantially occupied, low-momentum modes, and an incoherent region, comprising of the remaining sparsely occupied, high momentum modes. We use a single wavefunction, $\psi(\mathbf{r}, t)$, to model the coherent region as a whole, and treat the incoherent region as a thermal bath. Similarly to the truncated-Wigner approximation, we make use of a projector, \mathcal{P} , as defined in Equation (1.85), which here acts to preserve the distinction between the coherent and incoherent regions. The choice of k_{cut} typically corresponds to

the lowest mode that has an average occupation of less than one. However, in order to avoid aliasing, we still must ensure that k_{cut} never exceeds $N\pi/(2L)$.

Two important effects arise at finite temperature. The first is dissipation; the exchange of energy and matter between the coherent and incoherent regions. The second is fluctuations; changes in the configuration of atoms within the coherent region due to random internal collisions. We make use of the simple-growth SPGPE, given by Equation (1.87), where the dissipation of energy from the condensate is quantified by a dimensionless parameter, γ . Fluctuations, $\eta(\mathbf{r}, t)$, are assumed to be Gaussian, with correlations:

$$\langle \eta^*(\mathbf{r}, t) \eta(\mathbf{r}', t') \rangle = 2\gamma\hbar k_B T \delta(\mathbf{r} - \mathbf{r}') \delta(t - t'). \quad (1.88)$$

Here, the fluctuation amplitude increases with both temperature, T , and the dissipation parameter, γ .

The simple-growth SPGPE is an approximation of the full SPGPE, which has additional scattering terms. Since we do not make use of the latter in this thesis, we refrain from including this lengthy equation here, and instead refer the interested reader to Ref. [88], where a derivation using quantum optics may also be found.

1.6.5 The Spinor GPE

In the investigations of this thesis, we make use of spinor Bose gases; condensates for which the spin of constituent particles gives rise to additional degrees of freedom. More specifically, a gas of atoms with total spin F , may be split into $2F + 1$ components; one for each permitted value of the magnetic quantum number, m_F , as introduced in Section 1.5.1. This splitting is achieved via the magnetic Zeeman effect, as discussed in Section 1.5.5. The GPE derived in Section 1.6.1, given by equation (1.52), only accounts for scalar condensates, for which all atoms are in the same spin state. Thus, in order to model a multi-component Bose gas, the GPE requires some alterations. The modifications which we make to the GPE follow through to the PGPE and SPGPE accordingly, as shown explicitly in later chapters.

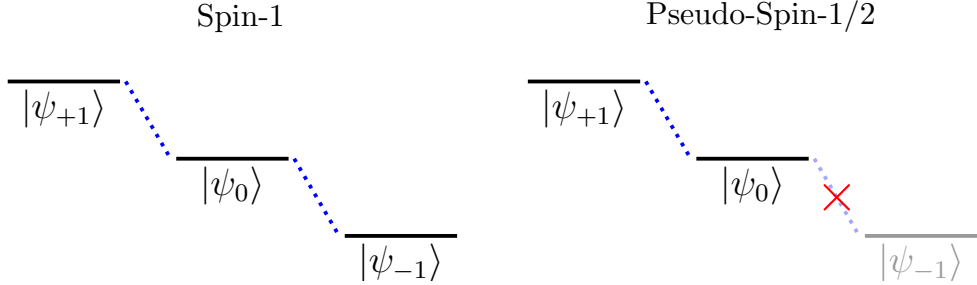


Figure 1.11: Level coupling diagrams for a simple spin-1 (left) and pseudo-spin-1/2 (right) system. Adjacent components interact via dipole-dipole interactions. The pseudo-spin-1/2 system is derived from the spin-1 system, by severing the communication between states $|\psi_0\rangle$ and $|\psi_{-1}\rangle$.

We first consider a spin-1 system; the most complicated system that appears in this thesis. Here, the scalar mean-field wavefunction ψ is replaced by the three component wavefunction $\psi = (\psi_{+1}, \psi_0, \psi_{-1})^\top$, where the subscript indicates the value of m_F . In order to adapt the GPE, we require the relevant spin matrices:

$$F_x = \frac{1}{\sqrt{2}} \begin{pmatrix} 0 & 1 & 0 \\ 1 & 0 & 1 \\ 0 & 1 & 0 \end{pmatrix}, \quad F_y = \frac{1}{\sqrt{2}i} \begin{pmatrix} 0 & 1 & 0 \\ -1 & 0 & 1 \\ 0 & -1 & 0 \end{pmatrix}, \quad F_z = \begin{pmatrix} 1 & 0 & 0 \\ 0 & 0 & 0 \\ 0 & 0 & -1 \end{pmatrix},$$

$$F_+ = \sqrt{2} \begin{pmatrix} 0 & 1 & 0 \\ 0 & 0 & 1 \\ 0 & 0 & 0 \end{pmatrix}, \quad F_- = \sqrt{2} \begin{pmatrix} 0 & 0 & 0 \\ 1 & 0 & 0 \\ 0 & 1 & 0 \end{pmatrix}. \quad (1.89)$$

We require two extra terms in the GPE; one to account for the Zeeman splitting that generates a spinor condensate in the first place, and another to account for inter-component dipole-dipole interactions. As derived in Ref. [96], the spin-1 GPE then takes the form:

$$i\hbar \frac{\partial \psi}{\partial t} = \left[-\frac{\hbar^2 \nabla^2}{2m} + V_{\text{trap}} - \mu + \tilde{H}_{\text{HFSZ}} \right] \psi + \frac{\partial}{\partial \psi^\dagger} \left[\frac{1}{2} c_0 (\psi^\dagger \psi)^2 + \frac{1}{2} c_1 (\psi^\dagger \mathbf{F} \psi)^2 \right], \quad (1.90)$$

where $(\psi^\dagger \mathbf{F} \psi)^2 \equiv (\psi^\dagger F_x \psi)^2 + (\psi^\dagger F_y \psi)^2 + (\psi^\dagger F_z \psi)^2$. The first term in the right-hand brackets corresponds to the usual intra-component dipole-dipole interactions and the second term is the new inter-component contribution. The scattering parameters are given by:

$$c_0 = \frac{g_0 + 2g_2}{3}, \quad c_1 = \frac{g_2 - g_0}{3}, \quad (1.91)$$

where $g_F = 4\pi\hbar^2 a_F/m$ and a_F is the s-wave scattering length of the total spin- F channel.

Here, \mathcal{F} is the vector sum of the total spins of the pair of particles involved in a collision. Due to angular momentum conservation, only even channels are permitted:

$$\mathcal{F} = 0, \dots, 2F. \quad (1.92)$$

Equation (1.90) may be written explicitly in terms of components as follows:

$$i\hbar \frac{\partial \psi_{+1}}{\partial t} = \left[-\frac{\hbar^2 \nabla^2}{2m} + V_{\text{trap}} - \mu + \hbar(\omega_q + \omega_l) + c_0 \boldsymbol{\psi}^\dagger \boldsymbol{\psi} + c_1 (|\psi_{+1}|^2 - |\psi_{-1}|^2) \right] \psi_{+1} + c_1 (\psi_0^\dagger \psi_{+1} + \psi_{-1}^\dagger \psi_0) \psi_0, \quad (1.93)$$

$$i\hbar \frac{\partial \psi_0}{\partial t} = c_1 (\psi_{+1}^\dagger \psi_0 + \psi_0^\dagger \psi_{-1}) \psi_{+1} + \left[-\frac{\hbar^2 \nabla^2}{2m} + V_{\text{trap}} - \mu + c_0 \boldsymbol{\psi}^\dagger \boldsymbol{\psi} \right] \psi_0 + c_1 (\psi_0^\dagger \psi_{+1} + \psi_{-1}^\dagger \psi_0) \psi_{-1}, \quad (1.94)$$

$$i\hbar \frac{\partial \psi_{-1}}{\partial t} = c_1 (\psi_{+1}^\dagger \psi_0 + \psi_0^\dagger \psi_{-1}) \psi_0 + \left[-\frac{\hbar^2 \nabla^2}{2m} + V_{\text{trap}} - \mu + \hbar(\omega_q - \omega_l) + c_0 \boldsymbol{\psi}^\dagger \boldsymbol{\psi} - c_1 (|\psi_{+1}|^2 - |\psi_{-1}|^2) \right] \psi_{-1}. \quad (1.95)$$

Note that this is the simplest form of the GPE we may have for a spin-1 system. As we will see in later chapters, we may add additional terms to manipulate the interactions between components.

We may use Equations (1.93)-(1.95) to derive the GPE for a pseudo-spin-1/2 system. To arrive at such a two-level system, we may simply assume that one level of the spin-1 system is unpopulated. Thus, here we set $\psi_{-1} = 0$. Then, we arrive at:

$$i\hbar \frac{\partial \psi_{+1}}{\partial t} = \left[-\frac{\hbar^2 \nabla^2}{2m} + V_{\text{trap}} - \mu + \hbar(\omega_q + \omega_l) + c_{11} |\psi_{+1}|^2 + c_{01} |\psi_0|^2 \right] \psi_{+1}, \quad (1.96)$$

$$i\hbar \frac{\partial \psi_0}{\partial t} = \left[-\frac{\hbar^2 \nabla^2}{2m} + V_{\text{trap}} - \mu + c_{00} |\psi_0|^2 + c_{01} |\psi_1|^2 \right] \psi_0, \quad (1.97)$$

where $c_{00} = c_0$ and $c_{11} = c_{01} = c_0 + c_1$.

1.7 Numerics

1.7.1 XMDS2

In the chapters which follow, we solve a number of coupled, stochastic partial differential equations numerically, in a range of spatial dimensions. This was achieved using the software package XMDS2 [97]; an XML-based code generator which makes use of pseudo-

spectral methods to optimize and facilitate the error-proofing of the equation solving process. Given the scale of simulations required to obtain meaningful statistics when solving stochastic equations numerically, the simulations of this thesis were carried out using the Rocket high performance computing service at Newcastle University.

1.7.2 Bootstrap Resampling Approach

Throughout this thesis, error bars are commonly calculated using a bootstrap resampling approach [98]. To avoid repetition, we describe this method here for later reference. Let X be some random variable and T be some statistic of X that we wish to obtain, with corresponding sample statistic t . Then, given an ensemble of \mathcal{N} realisations of X ; $\mathbf{x} = (x_1, x_2, \dots, x_{\mathcal{N}})$, we proceed as follows:

1. Sample N realisations from \mathbf{x} with replacement, which we will call $\mathbf{x}^{(1)}$. As a simple example, if $\mathcal{N} = 10$ and $N = 5$, we might obtain $\mathbf{x}^{(1)} = (x_9, x_3, x_7, x_1, x_7)$.
2. Calculate the sample statistic t of $\mathbf{x}^{(1)}$. We'll label this t_1 .
3. Repeat steps 1-2 M times, to obtain $\mathbf{t} = (t_1, t_2, \dots, t_M)$.
4. Then, we can approximate T by the sample mean, $\bar{\mathbf{t}}$, with error bars given by the sample standard deviation, $s(\mathbf{t})$.

Bootstrap methods are advantageous over standard frequentist approaches, since they do not assume Gaussian error distributions [99]. In fact, they can be used to derive an uncertainty on any statistic from any distribution. Whilst Bayesian inference offers similar benefits, this approach requires the determination of an appropriate prior distribution. Bootstrap methods have no such barrier.

1.7.3 The Mollweide Projection

In Chapter 4, we examine some functions of a spherical surface. Given access to a globe, visualizing such a function is simple. However, this thesis is restricted to two dimensions. Therefore, whenever such a function, f , arises, we make use of the Mollweide projection [100]. This pseudo-cylindrical projection transforms the surface of a sphere into an ellipse, with width-to-height ratio of 2:1. Commonly used to model the surface of the Earth, as shown in Figure 1.12, and the celestial sphere, the Mollweide projection prioritises relative-area preservation over shape and angle conservation.

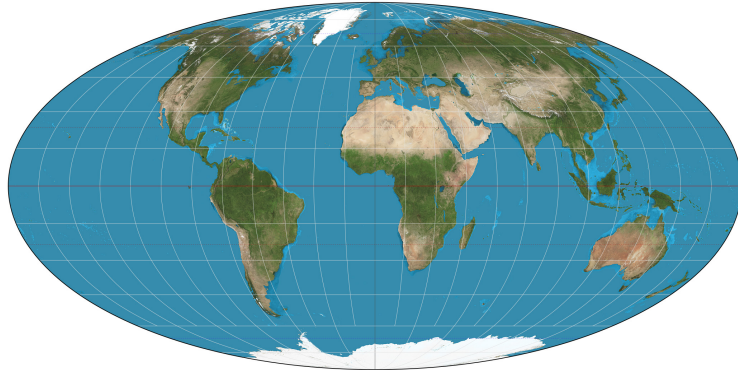


Figure 1.12: A Mollweide projection of the globe. (Image obtained from https://en.wikipedia.org/wiki/File:Mollweide_projection_SW.jpg under CC BY-SA 3.0 licence).

In line with Chapter 4, let $(\zeta_{+1}, \zeta_0, \zeta_{-1})$ denote the Cartesian coordinates of a sphere of radius 1, such that:

$$\zeta_{+1}^2 + \zeta_0^2 + \zeta_{-1}^2 = 1, \quad (1.98)$$

and let (X, Y) be the Cartesian coordinates of the ellipse we wish to map to:

$$\frac{X^2}{4} + Y^2 = 1. \quad (1.99)$$

We may move from (X, Y) coordinates to $(\zeta_{+1}, \zeta_0, \zeta_{-1})$ coordinates by making the transformations:

$$\phi = \sin^{-1}(Y), \quad (1.100)$$

$$\alpha = \cos^{-1}\left(\frac{2\phi + \sin(2\phi)}{\pi}\right), \quad (1.101)$$

$$\beta = \frac{\pi X}{2 \cos(\phi)}, \quad (1.102)$$

and

$$\zeta_{-1} = \sin(\alpha) \sin(\beta), \quad (1.103)$$

$$\zeta_0 = \cos(\alpha), \quad (1.104)$$

$$\zeta_{+1} = \sin(\alpha) \cos(\beta). \quad (1.105)$$

This allows us to visualize $f(X, Y)$ in place of $f(\zeta_{+1}, \zeta_0, \zeta_{-1})$.

1.8 Thesis Outline

This thesis is outlined as follows:

- In Chapter 1, we gave an overview of early-universe phase transitions, with an emphasis on those which may have been first order. We then formally introduced the notion of vacuum decay, before describing the instanton methodology used to calculate the decay rate. Next, we introduced the idea of analogue systems, and detailed the efforts that have been made thus far to model bubble nucleation using cold-atom systems. We went on to give an introduction to Bose-Einstein condensation and spin, before detailing the theoretical framework necessary to model spinor condensates numerically. Finally, we highlighted key numerical tools utilised throughout this work.
- In Chapter 2, we examine a one-dimensional quasi spin-1/2 Bose gas at finite temperature. Here, the scalar of interest is the relative phase between the two components. We adopt the time averaged potential of Fialko *et al.* [39, 41] and model the system using the SPGPE. We measure the spatial correlation function of fluctuations in the true vacuum state and compare with Klein-Gordon predictions. We then simulate bubble nucleation at a range of temperatures and barrier heights, and compare the numerical rate of false vacuum decay with instanton predictions.
- In Chapter 3, we replace the stationary interaction potential of Chapter 2 with the full oscillatory potential to be implemented experimentally. In line with the work of Braden *et al.* [42–44], we find this to give rise to a parametric instability. We go on to investigate whether thermal effects can overcome this instability.
- In Chapter 4, we move on to construct an alternative spin-1 system, whereby atomic components interact via Raman and radio-frequency coupling. We perform simulations of a one-dimensional system at zero temperature and observe bubble nucleation. We investigate the relationship between the rate of false vacuum decay and density for a number of atomic species, and once again compare findings to instanton predictions.
- In Chapter 5, we extend our investigations of false vacuum decay in spinor condensates to two spatial dimensions. We use a finite temperature approach to first model a spin-1 gas with periodic boundaries, and as usual, compare the simulated rate of decay with theoretical predictions. We then incorporate a trapping potential into the system and investigate the impact of boundaries on nucleation rate.

- In Chapter 6, we summarize the key findings of each chapter and highlight some interesting avenues for future work.

1.9 List of Publications

The investigations of this thesis appear in the following list of publications, with authors ordered alphabetically according to a popular convention in cosmology:

- *Simulating cosmological supercooling with a cold-atom system*
TP Billam, K Brown, IG Moss
Physical Review A **102** (4), 043324, 2020
- *Simulating cosmological supercooling with a cold-atom system II*
TP Billam, K Brown, A Groszek, IG Moss
Physical Review A **104** (5), 053309, 2021
- *False-vacuum decay in an ultracold spin-1 Bose gas*
TP Billam, K Brown, IG Moss
Physical Review A **105** (4), L041301, 2022
- *Bubble nucleation in a cold spin 1 gas*
TP Billam, K Brown, IG Moss
New Journal of Physics **25** (4), 043028, 2023

Chapter 2

Simulating False Vacuum Decay in a Pseudo-Spin-1/2 Bose Gas at Finite Temperature: Static Interaction Potential

2.1 Introduction

In this chapter, we investigate the false vacuum decay of the relative phase of a two-component Bose gas. We consider a one-dimensional, homogeneous system at finite temperature, with each component given by a different spin state of a shared atomic species, and make use of the static interaction potential of Fialko *et al.* [39, 41]. We first test the validity of the SPGPE, by examining the correlation of fluctuations about the true-vacuum state and comparing with Klein-Gordon predictions. We then go on to observe bubble nucleation in this system, and investigate the relationship between the rate of false vacuum decay, temperature and barrier height. We use Coleman’s instanton methodology [23, 24] to derive an analytic formula for the decay rate, which we fit to the simulated curves.

2.2 System

We begin with the baseline pseudo-spin-1/2 system introduced in Section 1.6.5. We make the assumption that inter-component dipole-dipole interactions are negligible and that each component has the same intra-component s-wave scattering length. Furthermore, in

order to isolate the physics of vacuum decay, we omit the trapping potential, V_{trap} , used to confine the condensate. Then the Hamiltonian density is given by:

$$H_{\text{baseline}} = -\frac{\hbar^2}{2m}\psi^\dagger \nabla^2 \psi + \frac{g}{2} \sum_{j=1,2} (\psi_j^\dagger \psi_j)^2 - \mu \psi^\dagger \psi, \quad (2.1)$$

where $\psi = (\psi_1, \psi_2)^\top$ ¹ is the two-component field operator, m is the atomic mass, g is the intra-component interaction strength and μ is the chemical potential.

The degeneracy between components is lifted by a static magnetic field B_z along the z -axis. We work in the strong-field regime, outside the range of validity of the linear and quadratic approximations discussed in Section 1.5.5. Thus, the Zeeman Hamiltonian takes the form:

$$H_{\text{Zeeman}} = \begin{pmatrix} \hbar\omega_z & 0 \\ 0 & 0 \end{pmatrix}, \quad (2.2)$$

where the Zeeman frequency ω_z is measured experimentally.

We couple states extrinsically using a radio frequency (RF) field with frequency ω_{RF} and Hamiltonian:

$$H_{\text{RF}} = \hbar\Omega(t) \cos(\omega_{\text{RF}}t) \sigma_x, \quad (2.3)$$

where $\sigma_{\{x,y,z\}}$ are the Pauli rotation matrices and $\Omega(t)$ is the Rabi frequency, which we assume to be real.

We may combine these effects in a single mixing Hamiltonian:

$$H_{\text{mix}} = H_{\text{Zeeman}} + H_{\text{RF}} = \begin{pmatrix} \hbar\omega_z & \hbar\Omega(t) \cos(\omega_{\text{RF}}t) \\ \hbar\Omega(t) \cos(\omega_{\text{RF}}t) & 0 \end{pmatrix}. \quad (2.4)$$

It is convenient to move to a rotating frame, by making the transformation:

$$\psi_{+1} \rightarrow \psi_{+1} e^{-i\omega_{\text{RF}}t}. \quad (2.5)$$

The mixing Hamiltonian transforms accordingly:

$$\tilde{H}_{\text{mix}} = \begin{pmatrix} \Delta & \hbar\Omega(t) \cos(\omega_{\text{RF}}t) e^{i\omega_{\text{RF}}t} \\ \hbar\Omega(t) \cos(\omega_{\text{RF}}t) e^{-i\omega_{\text{RF}}t} & 0 \end{pmatrix}, \quad (2.6)$$

where,

$$\Delta = \hbar(\omega_z - \omega_{\text{RF}}), \quad (2.7)$$

is the detuning. If we choose $\Delta = 0$ and make the rotating wave approximation, by

¹Here, components do not necessarily come from the $F = 1$ manifold of a spin-1 system, thus we have modified the notation of Section 1.6.5, replacing $\psi = (\psi_{+1}, \psi_0)^\top$ with the more general form, $\psi = (\psi_1, \psi_2)^\top$.

averaging over timescales longer than $2\pi/\omega_{\text{RF}}$, this simplifies to:

$$\tilde{H}_{\text{mix}} \approx \begin{pmatrix} 0 & \hbar\Omega(t)/2 \\ \hbar\Omega(t)/2 & 0 \end{pmatrix} = \frac{\hbar\Omega(t)}{2}\sigma_x. \quad (2.8)$$

The Rabi frequency modulates in time with an oscillation of frequency ω , as:

$$\Omega(t)/2 = -(\mu\epsilon^2 + \delta\hbar\omega \cos(\omega t)), \quad (2.9)$$

where $\mu\epsilon^2$ is the microwave-induced interaction strength and δ sets the modulation amplitude. The total Hamiltonian may then be written as:

$$H = \int dx \left\{ -\frac{\hbar^2}{2m}\psi^\dagger \nabla^2 \psi + V_{\text{int}}(\psi, \psi^\dagger) \right\}, \quad (2.10)$$

with interaction potential,

$$V_{\text{int}} = \frac{g}{2} \sum_{j=1,2} (\psi_j^\dagger \psi_j)^2 - \mu\psi^\dagger \psi - (\mu\epsilon^2 + \delta\hbar\omega \cos(\omega t))\psi^\dagger \sigma_x \psi. \quad (2.11)$$

Following the procedure of Fialko *et al.* [39, 41], we average over timescales longer than the modulation period and replace V_{int} with the stationary interaction potential:

$$V_{\text{stat}} = \frac{g}{2} \sum_{j=1,2} (\psi_j^\dagger \psi_j)^2 - \mu\psi^\dagger \psi - \mu\epsilon^2 \psi^\dagger \sigma_x \psi + \frac{g}{4}\epsilon^2 \lambda^2 (\psi^\dagger \sigma_y \psi)^2. \quad (2.12)$$

The right-most term arises as a result of the time-averaging procedure. Here, λ is a relic of the original modulation amplitude, as detailed further in Chapter 3.

We may reformulate V_{stat} in terms of the relative phase between components,

$$\varphi = \theta_1 - \theta_2. \quad (2.13)$$

We achieve this by making the Madelung transformation, under the assumption of approximately equal component particle densities, $n_1 \approx n_2 = n$:

$$\psi_1 \approx \sqrt{n}e^{i\theta_1}, \quad \psi_2 \approx \sqrt{n}e^{i\theta_2}. \quad (2.14)$$

As detailed in Appendix B.1, we arrive at:

$$V_{\text{stat}}(\varphi) \approx \frac{\mu^2}{g} \left[-1 - 2\epsilon^2 \cos(\varphi) + \epsilon^2 \lambda^2 \sin^2(\varphi) \right]. \quad (2.15)$$

This is shown for a selection of (ϵ, λ) values in Figure 2.1. From this, we learn that $V_{\text{stat}}(\varphi)$

has a true vacuum at $\varphi = 0$, corresponding to $\psi_1 = \psi_2$, and a false vacuum at $\varphi = \pi$, corresponding to $\psi_1 = -\psi_2$. The roles of ϵ^2 and λ become more apparent here; the value of ϵ sets the energy difference between vacua, whereas the value of λ determines the height of the potential barrier separating the vacua. It turns out that the component densities at the vacua at least, are indeed equal; at the true vacuum, $n = \rho_0(1 + \epsilon)$, and at the false vacuum, $n = \rho_0(1 - \epsilon)$, where $\rho_0 = \mu/g$ is the mean particle density.

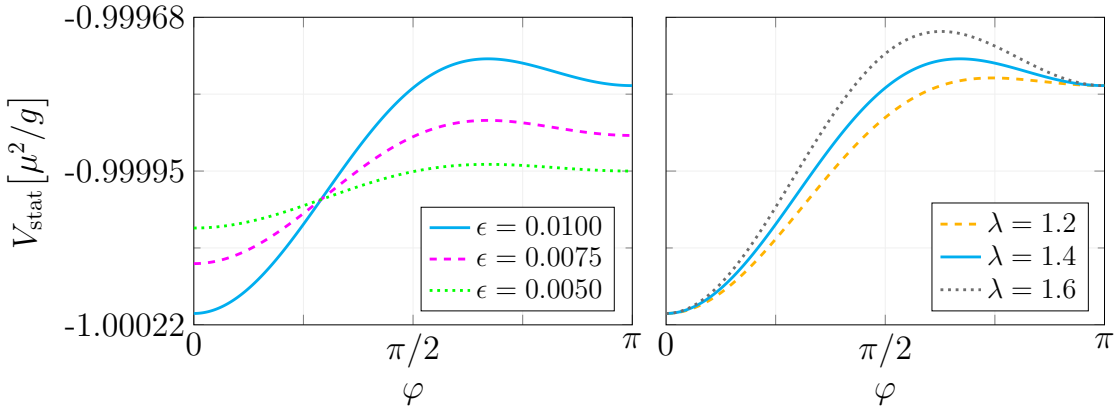


Figure 2.1: The dependence of V_{stat} on ϵ and λ . Left: Varying ϵ , with $\lambda = 1.4$, Right: Varying λ with $\epsilon = 0.01$. ϵ controls the energy difference between minima and λ controls the potential barrier height.

2.3 Numerical Modelling

We model our system numerically using the stochastic projected Gross-Pitaevskii equation (SPGPE):

$$i\hbar \frac{\partial \psi_j}{\partial t} = \mathcal{P} \left\{ \left(1 - i\gamma \right) \left[-\frac{\hbar^2}{2m} \frac{\partial^2 \psi_j}{\partial x^2} + \frac{\partial V_{\text{stat}}}{\partial \psi_j^*} \right] + \eta_j(x, t) \right\}, \quad j = 1, 2, \quad (2.16)$$

where,

$$\langle \eta^*(x, t) \eta(x', t') \rangle = 2\gamma \hbar k_B T \delta(x - x') \delta(t - t') \delta_{jj'}, \quad (2.17)$$

as introduced in Section 1.6.4. At this point, it is convenient to rescale the SPGPE in terms of characteristic quantities and dimensionless variables (denoted by tildes). As detailed in Appendix B.2, we make the transformations:

$$\begin{aligned} x &= \xi \tilde{x}, & t &= \omega_0^{-1} \tilde{t}, & \psi &= \rho_0^{1/2} \tilde{\psi}, \\ V_{\text{stat}} &= \hbar \omega_0 \rho_0 \tilde{V}_{\text{stat}}, & \eta &= \hbar \omega_0 \rho_0^{1/2} \tilde{\eta}, & T &= T_{\text{CO}} \tilde{T}, \end{aligned} \quad (2.18)$$

where $\xi = \hbar/(mg\rho_0)^{1/2}$ is the healing length of the system, $\omega_0 = c/\xi$ is a characteris-

tic frequency, dependent on the speed of sound $c = \hbar/(m\xi)$, and T_{CO} is the cross-over temperature; the temperature below which a phase-fluctuating quasi-condensate forms, as detailed in Section 1.4.4. For the two-component system, we choose the characteristic density to be the mean particle density, $\rho_0 = \mu/g$. Then we arrive at:

$$i\frac{\partial\tilde{\psi}}{\partial\tilde{t}} = \mathcal{P}\left\{(1 - i\gamma)\left[-\frac{1}{2}\frac{\partial^2\tilde{\psi}}{\partial\tilde{x}^2} + \frac{\partial\tilde{V}_{\text{stat}}(\tilde{\psi})}{\partial\tilde{\psi}^*}\right] + \tilde{\eta}(\tilde{x}, \tilde{t})\right\}, \quad (2.19)$$

where,

$$\langle\tilde{\eta}^*(\tilde{x}, \tilde{t})\tilde{\eta}(\tilde{x}', \tilde{t}')\rangle = 2\gamma\tilde{T}\delta(\tilde{x} - \tilde{x}')\delta(\tilde{t} - \tilde{t}')\delta_{jj'}. \quad (2.20)$$

Subsequently, we often omit the tildes, and rely on the presence or absence of \hbar to determine whether the SPGPE is in its dimensional or dimensionless form.

Typically, we set the dimensionless dissipation parameter $\gamma = 10^{-2}$; values of γ from $\mathcal{O}(10^{-4})$ to $\mathcal{O}(10^{-2})$ have been used in previous works that made direct comparisons to experiment [101–104], making this a reasonable choice. We explore the role of γ in Figure 2.8. The projector, \mathcal{P} , was tuned to eliminate modes above the momentum cut-off:

$$k_{\text{cut}} = \sqrt{\frac{2mk_{\text{B}}T}{\hbar^2}}. \quad (2.21)$$

In dimensionless units, the momentum cut-off is given by:

$$\tilde{k}_{\text{cut}} = \sqrt{2\rho_0\xi\tilde{T}}. \quad (2.22)$$

In Section 2.5 we verify that our results are robust under reasonable variations in k_{cut} .

Our SPGPE simulations use a one-dimensional grid of size $L = 240\xi$, with periodic boundaries and spacing $\Delta x = 0.4\xi$. The system is evolved using the fourth-order Runge-Kutta algorithm, with time step $\Delta t = 10^{-3}\omega_0^{-1}$. We set $\rho\xi = 100$, $\epsilon = 0.1$ and unless otherwise stated, calculate averaged quantities over $\mathcal{N} = 1000$ stochastic realisations.

2.4 Equilibrium Correlations

In order to verify the validity of our model, we chose to examine the correlation function of fluctuations in φ about the stable, true-vacuum state. This correlation function is defined as follows:

$$g(r) = \langle\varphi(x)\varphi(x')\rangle - \langle\varphi(x)\rangle\langle\varphi(x')\rangle, \quad (2.23)$$

where $r = |x - x'|$. In practice, it is more convenient to work with an alternative correlation function:

$$G(r) = \langle e^{i\varphi(x)} e^{-i\varphi(x')} \rangle. \quad (2.24)$$

We can recover $g(r)$ from this alternative correlation function via the formula:

$$g(r) = \ln|G(r)| + A, \quad (2.25)$$

where the value of A is determined by enforcing the condition $g(r) \rightarrow 0$ as $r \rightarrow \infty$.

We first initiated our system in the pure (i.e. fluctuation-free) true vacuum state. We then let our system equilibrate, before calculating $g(r)$. This quantity was averaged not only over space, but over $\mathcal{N} = 100$ stochastic realisations and 400 time steps. After some trial and error, we determined the appropriate temperature range of our investigations to be around $T/T_{\text{CO}} = 0.01 - 0.1$; safely within the quasi-condensate regime, as prescribed in Section 1.4.4. The evolution of $g(r)$ with r for $\lambda = 1.4$ is shown in Figure 2.2.

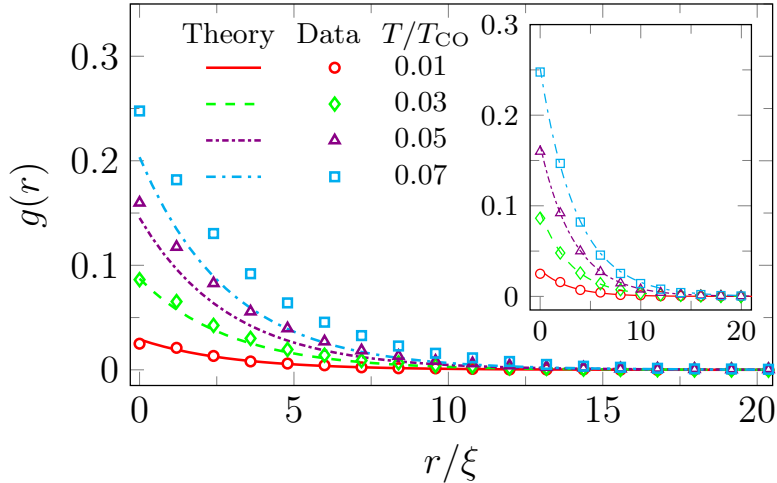


Figure 2.2: The correlation function, $g(r)$, of fluctuations in φ about the true vacuum state. This is shown at temperatures in the range $T/T_{\text{CO}} = 0.01 - 0.07$ for a potential with $\lambda = 1.4$ and $\epsilon = 0.1$. Marks indicate numerical data, which has been thinned in order to make clear comparison with theoretical curves. The main plot shows the Klein-Gordon correlation function for $\lambda = 1.4$, whereas the inset shows adjusted theoretical curves. The latter make use of temperature-dependent, effective values of λ , denoted λ_{eff} .

We are interested in the agreement between our numerical data and the theoretical, Klein-Gordon correlation function. To leading order, this is given by:

$$g_{\text{KG}}(r) = \frac{T}{\sqrt{2}m_{\text{T}}} e^{-\sqrt{2}m_{\text{T}}r} + \frac{T}{2}\delta(r), \quad (2.26)$$

where $m_T = \sqrt{2}\epsilon(\lambda^2 + 1)^{1/2}$ is the Klein-Gordon mass of the true-vacuum. The derivation of Equation (2.26) is detailed in Appendix B.3. As demonstrated in the main panel of Figure 2.2, at all temperatures investigated, there is reasonable agreement between the numerical and theoretical curves, particularly in shape. However, the agreement is notably stronger at lower temperatures. This is unsurprising, since nonlinear effects are expected to materialize as temperatures rise towards T_{CO} . Greater agreement can be achieved if we allow freedom in m_T and instead fit numerical data to the curve:

$$g_{\text{fit}}(r) = \frac{T}{a} e^{-ar}, \quad (2.27)$$

where a is a free parameter. We may then use the resultant values of a to obtain an effective value of λ for each temperature. We found that as temperature increases, λ_{eff} decreases away from 1.4, as shown in Figure 2.3. This is likely a renormalization effect, although an investigation into this is beyond the scope of this thesis. Our numerical data is plotted alongside the adjusted theoretical curves in the inset of Figure 2.2; we find excellent agreement at all temperatures investigated.

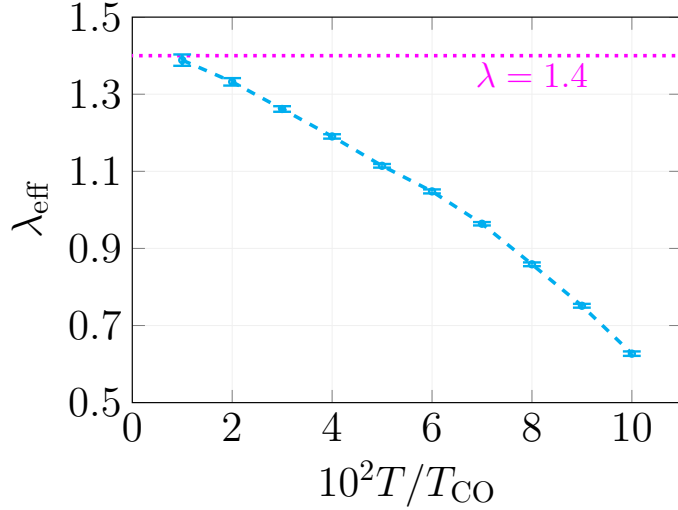


Figure 2.3: We may improve the agreement between numerical and theoretical $g(r)$ curves by replacing λ with temperature-dependent effective values, $\lambda_{\text{eff}}(T)$. The latter are obtained by fitting Equation (2.27) to the simulated data. Here, λ_{eff} is plotted against the dimensionless temperature, T , with 5% error bars (blue, dashed). A reference line (pink, dotted) is included to show the actual value of λ .

The alignment between numerical and theoretical results in this section indicates that the SPGPE is indeed an appropriate model choice for our investigations. We may proceed to simulate vacuum decay.

2.5 Bubble Nucleation

In order to model bubble nucleation using the SPGPE, we must first initialize the system in the metastable state. For the results which follow, we achieved this by simply placing the fields ψ_j in the pure false vacuum state at time $t = 0$, allowing thermal fluctuations to accumulate over time. However, we also verified that our results hold under a more experimentally realistic protocol. For this, the fields were again allowed to thermalize in

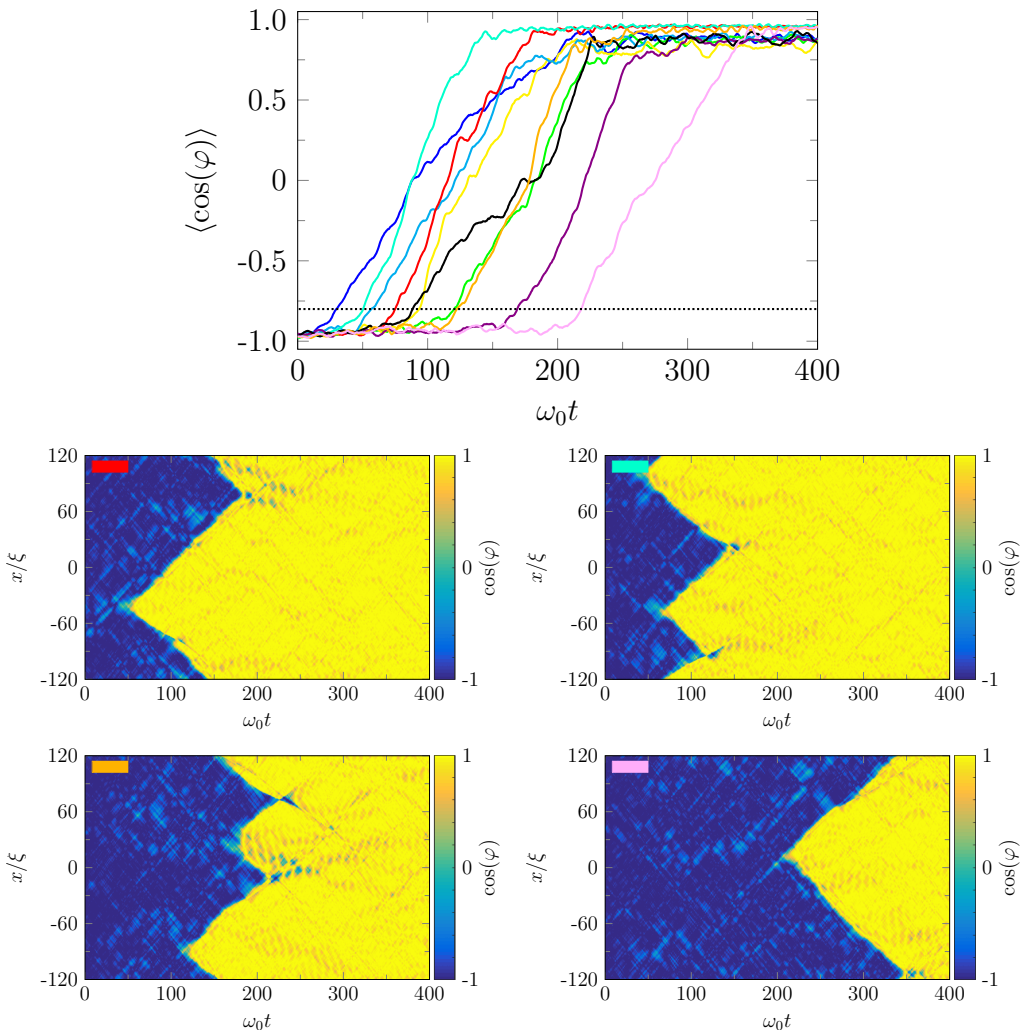


Figure 2.4: Examples of bubble growth at $T = 0.03T_{\text{CO}}$. Top: Trajectories of $\langle \cos(\varphi) \rangle$ for 10 simulation runs, where $\langle \dots \rangle$ denotes a spatial average. Bubble growth is characterised by a sudden increase in $\langle \cos(\varphi) \rangle$ from -1 to $+1$. Our threshold for bubble formation, $\langle \cos(\varphi) \rangle = -0.8$, is shown by a dotted line. Bottom: Plots of $\cos(\varphi)$ across space and time for four of the above trajectories. The coloured rectangle in the upper left-hand corner of each panel indicates which trajectory the panel corresponds to. Dark blue indicates a region of false vacuum, whereas bright yellow indicates a region of true vacuum.

the false vacuum state, but with a potential barrier high enough to inhibit vacuum decay. After a sufficient duration, the barrier height was then instantaneously lowered to that of interest. We improve upon this latter regime in subsequent chapters.

Bubble formation is shown for $T = 0.3T_{\text{CO}}$ in Figure 2.4. The top panel shows the evolution of $\langle \cos(\varphi) \rangle$ over time for 10 stochastic realisations. Here, $\langle \dots \rangle$ denotes spatial averaging only. Each trajectory fluctuates about $\langle \cos(\varphi) \rangle \approx -1$ initially, before rapidly increasing towards 1, signaling a nucleation event. The remaining panels of Figure 2.4 show the evolution of the spatial profile of $\cos(\varphi)$ for a selection of trajectories. From this small sample alone, we observe a clear variation in nucleation time; a positive indicator of first-order decay. Some profiles also exhibit multiple nucleation events, leading to bubble collisions. Whilst we do not examine the latter in detail in this thesis, they are certainly a feature of great interest.

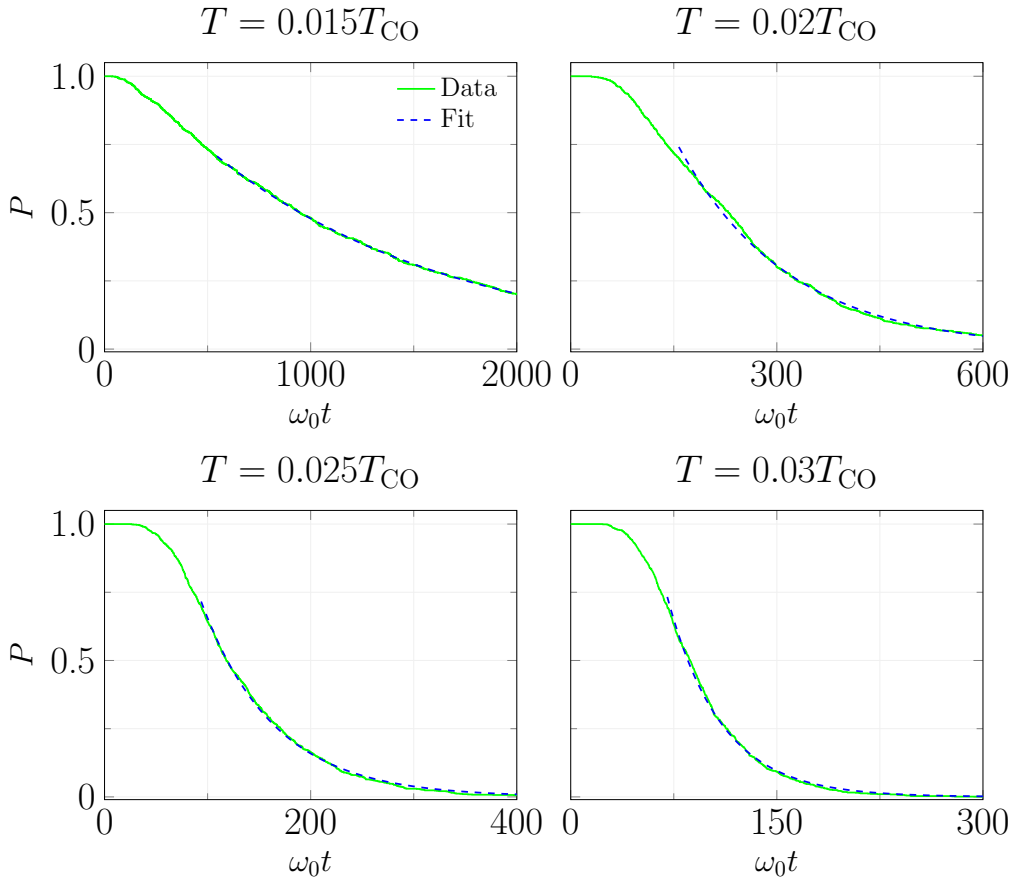


Figure 2.5: The probability, P , of remaining in the false-vacuum state over a range of temperatures, T , with $\lambda = 1.4$, $\epsilon = 0.1$ and $\rho\xi = 100$. The simulated curves (green, solid) are plotted alongside the corresponding fits to $P(t) = ae^{-\Gamma t}$ (blue, dashed). Fits are carried out over the region $P < 0.7$.

We can quantify the extent of vacuum decay in our system more precisely by examining

the probability, P , of remaining in the metastable state. This is given by the proportion of trajectories of $\langle \cos(\varphi) \rangle$ that are yet to cross the nucleation threshold, $-1 + \Delta$, where Δ must exceed the typical amplitude of thermal fluctuations. In practice, we averaged over an ensemble of $\mathcal{N} = 1000$ trajectories and selected $\Delta = 0.2$, as indicated in the top panel of Figure 2.4. Plots of $P(t)$ are shown for $T = (0.015 - 0.03)T_{\text{CO}}$ in Figure 2.5. Each curve exhibits an initial plateau, but subsequently decays; the higher the temperature, the faster the decay. The plateau - the length of which varies with both initialization protocol and Δ - is of little concern; our system simply takes time to thermalize. For a first-order transition, we expect P to decay exponentially with time. Therefore, each panel of Figure 2.5 also contains a fit to $P(t) = ae^{-\Gamma t}$, with freedom in both a and Γ . To avoid the plateau, each fit is carried out from the time at which $P < 0.7$ is first reached. The fits align very closely with the simulated data, providing further evidence that first-order vacuum decay has been achieved. We use these fits to examine the rate of vacuum decay, Γ .

Before proceeding, we verified that our results are not overly sensitive to the choice of momentum cut-off, k_{cut} . As detailed in Section 2.3, we generally set $k_{\text{cut}} = \sqrt{2\rho_0\xi T}$. Here, we instead used $k_{\text{cut}} \rightarrow \sqrt{2}k_{\text{cut}}$ to calculate $P(t)$. We compare the resultant curves to the previous results in Figure 2.6. At the lowest temperature investigated, we observe a minor shift in $P(t)$, but in general, raising k_{cut} has little effect.

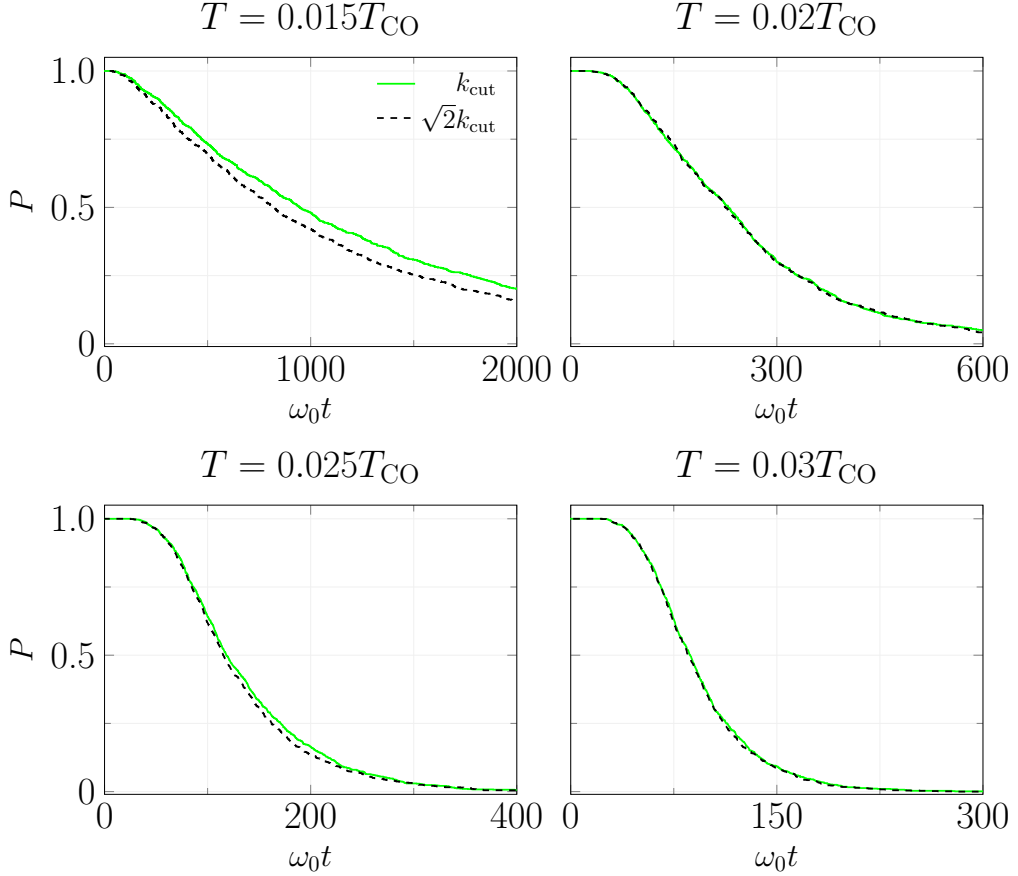


Figure 2.6: The effect of raising the momentum cut-off, k_{cut} , on the survival probability, P . Here, $\lambda = 1.4$, $\epsilon = 0.1$ and $\rho\xi = 100$. We compare the curves generated using the standard cut-off, $k_{\text{cut}} = \sqrt{2\rho_0\xi T}$ (green, solid), to those generated using $\sqrt{2}k_{\text{cut}}$ (black, dashed).

We may compare our simulated Γ values to those predicted by the semi-classical instanton approach of Coleman *et al.* [23, 24], as described in Section 1.2.1. For a one-dimensional thermal system, the theoretical rate of vacuum decay is given by:

$$\Gamma_{\text{inst}} = AB^{1/2}e^{-B}, \quad (2.28)$$

where the prefactor, A , is only mildly temperature dependent, and thus can be treated as an undetermined constant. We find the exponent, B , by following Coleman's methodology under a Klein-Gordon approximation, and making use of the results of Ref. [27]. As detailed in Appendix B.4, we obtain:

$$B = \frac{\alpha(\lambda)\epsilon}{T}, \quad (2.29)$$

where,

$$\alpha(\lambda) = 4 \left\{ (\lambda^2 - 1)^{1/2} - \lambda^{-1} \ln \left[(\lambda^2 - 1)^{1/2} + \lambda \right] \right\}. \quad (2.30)$$

Figure 2.7 examines the dependence of Γ on temperature, over a range of barrier heights. Here, the simulated data points are shown alongside the corresponding instanton curves. Error bars for the prior, which reflect the statistical uncertainties of ensemble averaging, were computed using the bootstrap resampling approach detailed in Section 1.7.2, taking $N = 1000$ and $M = 100$. Two variations of Γ_{inst} are included for each value of λ . The first, labelled $\text{KG}(A)$, is the result of fitting Equation (2.28) to the simulated data, using the $\alpha(\lambda)$ values obtained from Equation (2.30), whilst allowing freedom in the prefactor, A . In general, the resultant curves agree nicely with the simulated data. However, in light of the renormalization effects eluded to in Section 2.4, we also generated alternative fits, $\text{KG}(A, \alpha)$, obtained by allowing freedom in both A and α . These curves align more closely with the SPGPE results, but are not hugely dissimilar to the previous fits overall.

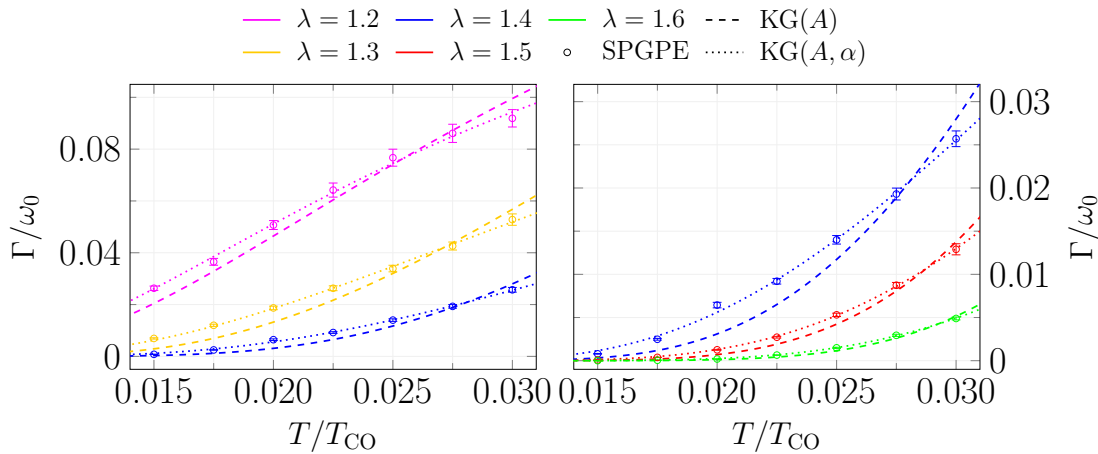


Figure 2.7: A comparison of the rate of bubble growth, Γ , as a function of temperature, T , between the SPGPE and instanton approaches at a range of barrier heights, λ . Dashed - only the pre-factor, A , of the instanton approach is fitted to our data. Dotted - both A and α are fitted. Here, $\epsilon = 0.1$ and $\rho\xi = 100$.

We repeated a sample of our SPGPE simulations with a reduced dissipation parameter, $\gamma = 5 \times 10^{-3}$. The result of this is shown in Figure 2.8. Unsurprisingly, we find the rate of false vacuum decay, Γ , to reduce with γ . This is particularly evident at lower barrier heights. However, the simulated results are still well fitted by the instanton approach, albeit with different values of A .

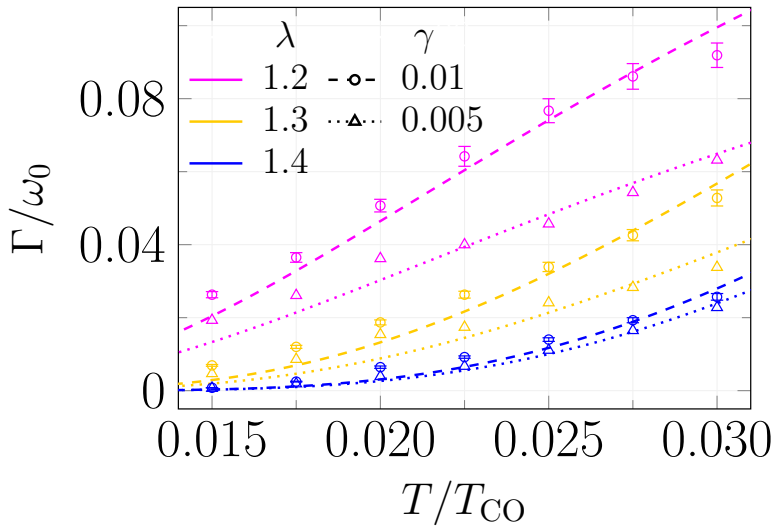


Figure 2.8: The effect of lowering the dissipation parameter, γ , on the rate of vacuum decay, Γ . We halve the usual value of $\gamma = 0.01$ to $\gamma = 0.005$ and compare the relationship between Γ and temperature, T , over a range of barrier heights, λ , for each. The points show the simulated data ($\gamma = 0.01$ - circles, $\gamma = 0.005$ - triangles) and the lines show the corresponding instanton fits ($\gamma = 0.01$ - dashed, $\gamma = 0.005$ - dotted), with $\alpha(\lambda)$ prescribed by Equation (2.30) and freedom in A . The error bars for $\gamma = 0.01$ were generated using the bootstrap resampling approach detailed in Section 1.7.2. Error bars for $\gamma = 0.005$ are omitted, since we deemed the least squares error bars to be sufficient for this brief investigation. These were contained within the data points. Note that the data for $\gamma = 0.01$ is identical to that plotted in the left panel of Figure 2.7. Here, $\epsilon = 0.1$ and $\rho\xi = 100$.

2.6 Experimental realization

Having successfully modelled first order vacuum decay in a finite temperature cold-atom system, we go on to consider experimental implementation.

We assume a quasi-one-dimensional Bose gas, tightly confined by a transverse harmonic trap of frequency ω_\perp . Assuming a three-dimensional thermal cloud, the one-dimensional SPGPE, given by Equation (2.16), with dimensionally-reduced interaction strength $g = 2\hbar a_s \omega_\perp$, as detailed in Appendix A.1, is a valid description provided that $\hbar\omega_\perp \lesssim k_B T$ [105]. In principle, the chemical potential should satisfy $\mu = \hbar\omega_0 \ll \hbar\omega_\perp$. However, in practice the condition $\omega_0 \lesssim \omega_\perp$ has been shown to suffice in one-dimensional SPGPE equilibrium studies [106, 107] of quasi-1D atom-chip experiments [108, 109]. The most direct realization of our simulations, which have periodic boundary conditions, would be to trap the Bose gas in a ring-shaped geometry. We expect that our general results would also apply qualitatively to linear quasi-one-dimensional experiments with a flat “box” trap [110] in the longitudinal direction or with a harmonic longitudinal trap, which gives rise to the classic “cigar-shaped” quasi-one-dimensional Bose gas. In either case, our results would

apply broadly in the bulk, but the effects of the boundaries would need to be considered in the former, and non-uniform background density would need to be accounted for in the latter.

As an example experimental configuration, we consider one of the experimental setups proposed by Fialko *et al.* [39, 41], which is based on tuning the interactions between two Zeeman states of ${}^7\text{Li}$. Note that in this example, the intracomponent scattering lengths of the spin states are asymmetrical and the potential has to be slightly modified. The interactions can be tuned using a Feshbach resonance to achieve the required close-to-zero inter-component scattering length. Based on the average intracomponent scattering length, suitable experimental parameters would be 5×10^4 atoms in a quasi-one-dimensional optical trap [111] of length $90\mu\text{m}$ and transverse frequency $2\pi \times 66\text{kHz}$, with interaction parameter $\zeta = (\rho_0\xi)^{-2} = 10^{-4}$ and cross-over temperature $T_{\text{CO}} = 215\mu\text{K}$. The results of Figures 2.5-2.8 correspond to temperatures of around 3.2 to $6.4\mu\text{K}$. At such temperatures, the relative phase correlation length is larger than the average nucleated bubble.

2.7 Conclusion

In this chapter, we demonstrated that a quasi-condensed, 2-component, thermal Bose gas would serve as a laboratory analog to an early-universe, supercooled phase transition. We verified the validity of SPGPE simulations, by examining fluctuations about the true-vacuum state and comparing to Klein-Gordon predictions. We then succeeded in simulating vacuum-decay in this system, and found good agreement between the simulated rates of vacuum decay, and those predicted via instanton calculations.

Chapter 3

Simulating False Vacuum Decay in a Pseudo-Spin-1/2 Bose Gas at Finite Temperature: Oscillatory Interaction Potential

3.1 Introduction

In Chapter 2, we successfully simulated first-order vacuum decay in a finite-temperature, two-component Bose gas. Whilst indicative of experimental success, these results were obtained using the time-averaged interaction potential, V_{stat} , of Fialko *et al.* [39, 41]. In the zero-temperature work of Braden *et al.* [42–44], it was shown that upon replacing V_{stat} with its oscillatory predecessor, V_{osc} , a parametric instability can arise. This instability accelerates the decay of the false-vacuum state, inhibiting first-order behaviour. In this chapter, we demonstrate that by including thermal effects, it is possible to suppress the instability and recover first-order vacuum decay.

3.2 System

In this chapter, we proceed with the system of Chapter 2. Namely, a one-dimensional, homogeneous, 2-component Bose gas, as introduced in Section 2.2. However, we replace the stationary interaction potential of Chapter 2:

$$V_{\text{stat}} = \frac{g}{2} \sum_{j=1,2} (\psi_j^\dagger \psi_j)^2 - \mu \psi^\dagger \psi - \mu \epsilon^2 \psi^\dagger \sigma_x \psi + \frac{g}{4} \epsilon^2 \lambda^2 (\psi^\dagger \sigma_y \psi)^2, \quad (3.1)$$

with the time-dependent potential from which it was derived:

$$V_{\text{osc}} = \frac{g}{2} \sum_{j=1,2} (\psi_j^\dagger \psi_j)^2 - \mu \psi^\dagger \psi - (\mu \epsilon^2 + \delta \hbar \omega \cos(\omega t)) \psi^\dagger \sigma_x \psi. \quad (3.2)$$

Here, ω is the frequency of V_{osc} , and δ controls the modulation amplitude. Crucially, δ sets the geometry of V_{stat} , via the relation $\lambda = \sqrt{2}\delta/\epsilon$.

For the investigations which follow, it is convenient to return to the dimensionless units of Section 2.3. We proceed with parameterization (2.18), alongside the additional transformations:

$$\omega = \omega_0 \tilde{\omega}, \quad V_{\text{osc}} = \hbar \omega_0 \rho_0 \tilde{V}_{\text{osc}}. \quad (3.3)$$

Again, by making the Madelung transformation (2.14) we are able express \tilde{V}_{osc} in terms of the relative phase, φ :

$$\tilde{V}_{\text{osc}} \approx -1 - 2 \cos(\varphi) [\epsilon^2 + \delta \tilde{\omega} \cos(\tilde{\omega} \tilde{t})]. \quad (3.4)$$

The evolution of $V_{\text{osc}}(\varphi)$ is shown for a range of frequencies in Figure 3.1.

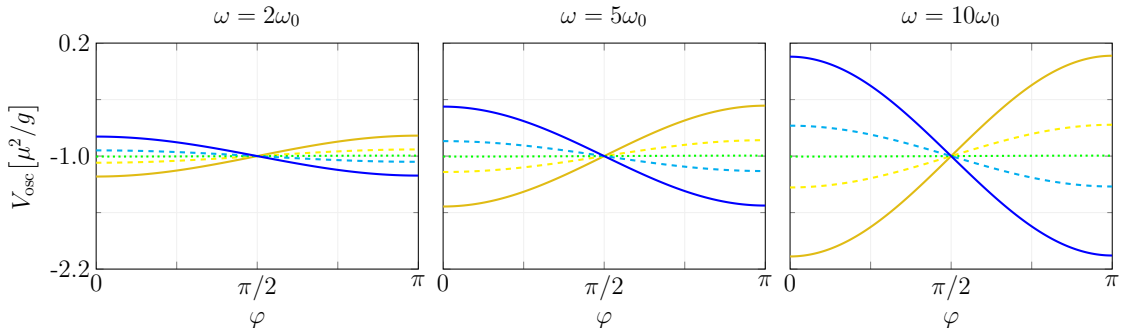


Figure 3.1: The evolution of V_{osc} for a range of modulation frequencies, ω . In each panel, the yellow, solid curve corresponds to $t = \{0, 2\pi/\omega, 4\pi/\omega, \dots\}$, the blue, solid curve corresponds to $t = \{\pi/\omega, 3\pi/\omega, 5\pi/\omega, \dots\}$, and the green, dotted curve corresponds to $t = \{\pi/(2\omega), 3\pi/(2\omega), 5\pi/(2\omega), \dots\}$. The blue and yellow dashed curves show intermediate behaviour. Here, $\epsilon = 0.05$ and $\lambda = 1.5$.

3.3 Time averaging

From Figures 2.1 and 3.1, it is not immediately obvious that upon time averaging, V_{osc} reduces to V_{stat} . At any given time, the prior exhibits both a local minimum and local maximum (or is constant), whereas the latter contains a global and local minimum. Furthermore, given the apparent symmetry of V_{osc} about $-\mu^2/g$, it is not outrageous to speculate that V_{osc} might entirely flatten upon averaging. In this section, we verify the correspondence between V_{osc} and V_{stat} , by means of a simple averaging procedure.

Our considerations are independent of the projection involved in the SPGPE, so for simplicity we remove it. The resultant stochastic GPE (SGPE), in dimensionless form, is given by:

$$i \frac{\partial \psi_j}{\partial t} = (1 - i\gamma) \left[-\frac{1}{2} \frac{\partial^2 \psi_j}{\partial x^2} + \frac{\partial \hat{V}_{\text{osc}}}{\partial \psi_j^*} \right] + \eta_j, \quad j = 1, 2. \quad (3.5)$$

In order to classify the extrema, we make the ansatz:

$$\psi_1 = e^{\chi/2} e^{\sigma/2} e^{i\varphi/2} e^{i\theta/2}, \quad (3.6)$$

$$\psi_2 = \pm e^{\chi/2} e^{-\sigma/2} e^{-i\varphi/2} e^{i\theta/2}, \quad (3.7)$$

where χ , σ , φ and θ represent fluctuations in global density, relative density, relative phase, and total phase, respectively. The positive and negative signs are chosen for expansion about $\varphi = 0$ and $\varphi = \pi$, respectively. As detailed in Appendix C.1, by linearizing in $\{\chi, \sigma, \varphi, \theta\}$, Fourier transforming in space, and assuming that $\delta = \mathcal{O}(\epsilon)$ and $\gamma = \mathcal{O}(\epsilon)$, we arrive at:

$$\frac{\partial \hat{\varphi}}{\partial t} = -(a \pm 2\delta\omega \cos(\omega t)) \hat{\sigma} - \gamma(b \pm 2\delta\omega \cos(\omega t)) \hat{\varphi} + \hat{\eta}_\varphi, \quad (3.8)$$

$$\frac{\partial \hat{\sigma}}{\partial t} = -\gamma(a \pm 2\delta\omega \cos(\omega t)) \hat{\sigma} + (b \pm 2\delta\omega \cos(\omega t)) \hat{\varphi} + \hat{\eta}_\sigma, \quad (3.9)$$

where $a = \frac{1}{2}k^2 + 2 \pm 2\epsilon^2$ and $b = \frac{1}{2}k^2 \pm 2\epsilon^2$. Here, hats are used to denote a spatial Fourier transform. Setting $\gamma = \delta = 0$ above reveals the natural frequency of the unmodulated system, $\omega_n = \sqrt{ab}$. Thus, whilst we delay discussions of stability to Section 3.4, we keep in mind the parametric resonance of the modulated system at $\omega = 2\omega_n$. Equations (3.8)-(3.9) are analogous to those which describe the stabilization of the inverted Kapitza pendulum [40], therefore we follow a similar line of analysis here to find a time-averaged effective description of V_{osc} . We set:

$$\varphi = \varphi_0 + \varphi_1 \cos(\omega t) + \varphi_2 \sin(\omega t), \quad (3.10)$$

$$\sigma = \sigma_0 + \sigma_1 \sin(\omega t) + \sigma_2 \cos(\omega t), \quad (3.11)$$

under the assumptions that $\varphi_{\{1,2\}}$ and $\sigma_{\{1,2\}}$ are small compared to φ_0 and σ_0 , vary slowly compared to the sinusoidal terms, and $\omega^2 \gg ab$. By substituting the above into Equations (3.8)-(3.9) and collecting coefficients of $\sin(\omega t)$ and $\cos(\omega t)$, we are able to express each of the prefactors in terms of φ_0 and σ_0 :

$$\varphi_1 = \pm \frac{2\delta a}{\omega} (\varphi_0 - \gamma\sigma_0), \quad (3.12)$$

$$\varphi_2 = \mp 2\delta(\sigma_0 + \gamma\varphi_0), \quad (3.13)$$

$$\sigma_1 = \pm 2\delta(\varphi_0 - \gamma\sigma_0), \quad (3.14)$$

$$\sigma_2 = \pm \frac{2\delta b}{\omega} (\sigma_0 + \gamma\varphi_0). \quad (3.15)$$

Then, upon taking the period averages of Equations (3.8)-(3.9) in the long wavelength limit, $k \ll 1$, and neglecting terms of order $\mathcal{O}(\gamma\delta^2)$, we obtain:

$$\dot{\varphi}_0 = -2\sigma_0 + \bar{\eta}_\varphi, \quad (3.16)$$

$$\dot{\sigma}_0 = \frac{1}{2}\omega_k^2\varphi_0 - 2\gamma\sigma_0 + \bar{\eta}_\sigma, \quad (3.17)$$

where $\omega_k^2 = k^2 + 4\epsilon^2(\lambda^2 \pm 1)$. Finally, by eliminating σ_0 , we arrive at:

$$\ddot{\varphi}_0 + 2\gamma\dot{\varphi}_0 + \omega_k^2\varphi_0 = \eta_{\text{eff}}. \quad (3.18)$$

This is a damped Klein-Gordon equation for the potential $V_{\text{KG}} = \frac{1}{2}\omega_k^2\varphi_0^2$, with noise n_{eff} . Provided that $\lambda > 1$, the quantity $V''_{\text{KG}}(\varphi_0) = \omega_k^2$ is positive for both $\varphi_0 = 0$ and $\varphi_0 = \pi$. Thus, over timescales longer than the modulation period, V_{osc} does indeed exhibit two minima.

3.4 Instability

We anticipate a parametric resonance when the modulation frequency, ω , approaches double the natural frequency of the system, ω_n [112]. From Equations (3.8)-(3.9) we may deduce $\omega_n = \sqrt{ab}$, and consequently identify a resonance at $\omega = 2\sqrt{ab}$. Close to this resonance, which is expected to accelerate the decay of the false vacuum state, we make the approximations:

$$\varphi = A(t) \cos(\omega t/2) + B(t) \sin(\omega t/2), \quad (3.19)$$

$$\sigma = C(t) \cos(\omega t/2) + D(t) \sin(\omega t/2), \quad (3.20)$$

where $A - D$ vary slowly in time. By substituting the above into Equations (3.8)-(3.9), and time averaging (see Appendix C.2 for details), we arrive at a system of equations for $A - D$:

$$\begin{pmatrix} \dot{A} \\ \dot{B} \\ \dot{C} \\ \dot{D} \end{pmatrix} = \begin{pmatrix} -\gamma b & -\omega/2 & -(a \pm \delta\omega) & 0 \\ \omega/2 & -\gamma b & 0 & \pm\delta\omega - a \\ b \pm \delta\omega & 0 & -\gamma a & -\omega/2 \\ 0 & -(\pm\delta\omega - b) & \omega/2 & -\gamma a \end{pmatrix} \begin{pmatrix} A \\ B \\ C \\ D \end{pmatrix}. \quad (3.21)$$

Let λ_+ denote the eigenvalue of system (3.21) with largest real part. Then, the growth rate of $A - D$ is given by $\Gamma_{PR} = \text{Re}(\lambda_+)$. The formula for λ_+ is given by Equation (C.39) of Appendix C.2. The growth rate about the false vacuum is shown for a range of modulation frequencies in the left panel of Figure 3.2.

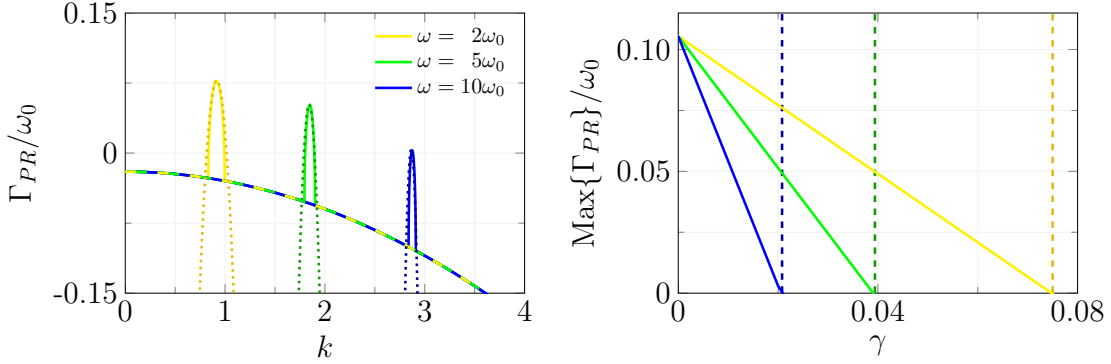


Figure 3.2: Left: The growth rate Γ_{PR} of the spatial Fourier modes, plotted as a function of wave number k . The microwave mixing is modulated with frequency ω and the damping is governed by the parameter γ . Here, $\gamma = 0.02$. The resonance band approximation, Equation (3.22), is shown by a dotted line. Right: the peak growth rate, $\text{Max}\{\Gamma_{PR}\}$, as a function of damping, γ . For each modulation frequency, the approximate value of γ_{damp} , as predicted by equation (3.24), is indicated by a dashed, vertical line. For both panels, $\epsilon = 0.05$ and $\lambda = 1.5$.

At each frequency, the solutions of (3.21) only grow within a narrow band of k values about some central value, $k_b(\omega)$. Inside the resonance band, we let $k = k_b \pm \Delta k$, where Δk is small. Inserting this into Equation (C.39), via the definitions of $a(k)$ and $b(k)$, gives, to leading order:

$$\Gamma_{PR} = 2\delta - \frac{1}{2}\gamma(k_b^2 + 2) - \frac{(k_b^2 + 2)^2}{4\delta(k_b^2 + 4)}\Delta k^2. \quad (3.22)$$

Thus, as expected, the growth rate peaks at the centre of the resonance band, where $\Delta k = 0$ and $\Gamma_{PR} = 2\delta - \gamma(k_b^2 + 2)/2$. This indicates that it is possible to suppress the resonance by raising the damping parameter γ above $4\delta/(k_b^2 + 2)$.

For the parametric resonance at $\omega = 2\sqrt{ab}$, the definitions of $a(k)$ and $b(k)$ yield:

$$k_b^2 = (4 + \omega^2)^{1/2} - 2 \mp 4\epsilon^2. \quad (3.23)$$

Therefore, we expect the parametric instability of the false vacuum state to be damped out when γ exceeds:

$$\gamma_{\text{damp}} = \frac{4\delta}{(\omega^2 + 4)^{1/2} + 4\epsilon^2}. \quad (3.24)$$

The approximate resonance bands given by Equation (3.22) are also included in the left panel of Figure 3.2. At each modulation frequency considered, these align well with the corresponding bands obtained directly from Equation (3.21). This verifies the validity of Equation (3.22) and, by extension, the damping condition (3.24). We may confirm the latter by examining the relationship between $\text{Max}\{\Gamma_{PR}\}$ and γ . The peak values of Γ_{PR} acquired by solving Equation (3.21) are shown for a range of γ values in the right panel of Figure 3.2. We find $\text{Max}\{\Gamma_{PR}\}$ to decrease linearly, reaching zero very close to the predicted values. The higher the modulation frequency, the lower the value of γ at which the instability is erased. Here, the range of ω values investigated was limited by the SPGPE, since in order to compare with this numerical approach later, we require the resonance bands to lie below the momentum cut-off of the SPGPE. However, in principle, it is experimentally feasible to raise the modulation frequency above $\omega = 10$, which would likely lower the amount of damping required to erase the instability.

With hope that the instability can be overcome, and an understanding of the parameter space for which this is likely, we proceed to simulate the oscillatory system.

3.5 Numerical Setup

We now perform numerical simulations of the SPGPE, in order to characterize the mechanism of false vacuum decay in the fully nonlinear system. We compare the dynamical phase transition for both the oscillatory potential, V_{osc} , and the static potential, V_{stat} , examined in Chapter 2. With Equation (3.24) in mind, we explore parameter ranges in which parametric instability is anticipated. By raising γ beyond γ_{damp} , we hope to see a progression towards the first-order behaviour observed for the stationary potential.

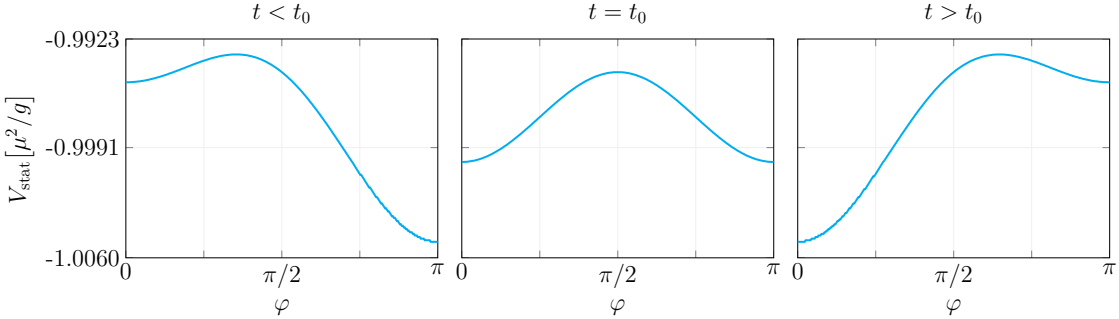


Figure 3.3: The role of the control parameter, $\alpha(t)$, as defined in Equation (3.25). Here, this is shown for the static potential, V_{stat} , for simplicity. Prior to the switching time, t_0 , the potential exhibits a local minimum at $\varphi = 0$ and a global minimum at $\varphi = \pi$. Beyond t_0 , we instead find a global minimum at $\varphi = 0$ and a local minimum at $\varphi = \pi$. The switch takes place over duration τ .

In line with experimental protocol, we first place the system in a stable state. We then raise the energy of this state, such that it becomes metastable. This methodology also draws greater analogy with the evolution of the early universe, for which particle fields are in a symmetric state at high temperature and a broken symmetry state at low temperatures [113–115]. More precisely, we introduce a control parameter:

$$\alpha(t) = \frac{\pi}{2} \left[1 - \tanh \left(\frac{t - t_0}{\tau} \right) \right], \quad (3.25)$$

which is incorporated into V_{osc} and V_{stat} via the modification:

$$\epsilon^2 \psi^\dagger \sigma_x \psi \rightarrow \epsilon^2 \cos(\alpha) \psi^\dagger \sigma_x \psi. \quad (3.26)$$

This acts to switch the nature of the vacua over time, as shown in Figure 3.3. Here, t_0 is the time about which the vacuum switch is centered and τ is the duration of the switch. Prior to t_0 , the true vacuum is located at $\varphi = \pi$ and the false vacuum, at $\varphi = 0$. Beyond t_0 , the opposite holds. In our simulations, we use $t_0 = 100$ and $\tau = 5$.

3.6 Numerical Results

In Chapter 2, we found that in the presence of the static potential, V_{stat} , the decay of the metastable state occurs via bubble nucleation. In contrast, in the oscillatory case, decay can also be caused by the exponential growth of fluctuations in the resonance band. If these fluctuations have an initial value $\varphi(t_0)$, then they grow beyond some critical amplitude σ_c and fall into the stable state at time t if $|\varphi(t_0) - \pi| \exp\{\Gamma_{PR}(t - t_0)\} > \sigma_c$. In this context, σ_c is given by the width of the potential barrier. Since the initial fluctuations are small, and in the linear regime, they have an initial Gaussian distribution with standard

deviation σ . The probability of remaining in the metastable state at time t is therefore:

$$P = \operatorname{erf}\left(\frac{\sigma_c}{\sqrt{2}\sigma} e^{-\Gamma_{PR}(t-t_0)}\right). \quad (3.27)$$

In the large time limit, this reduces to exponential decay, with rate Γ_{PR} .

The impact of the instability becomes apparent upon examining the relationship between φ and γ , as explored qualitatively in Figure 3.5. Here, the evolution of $\cos(\varphi)$ is shown for the oscillatory potential, V_{osc} , with modulation frequency $\omega = 5\omega_0$, over a range of γ values. A clear dependence on γ emerges. At low γ , the instability is obvious; $\cos(\varphi)$ fluctuates erratically, leaving no sign of bubble formation. However, as γ increases, fluctuations lessen, allowing larger true-vacuum regions to form. At high enough γ , the oscillatory-potential phase profile becomes highly resemblant of the static-potential profiles shown in Figure 2.4; a promising indicator that first-order behaviour can be recovered.

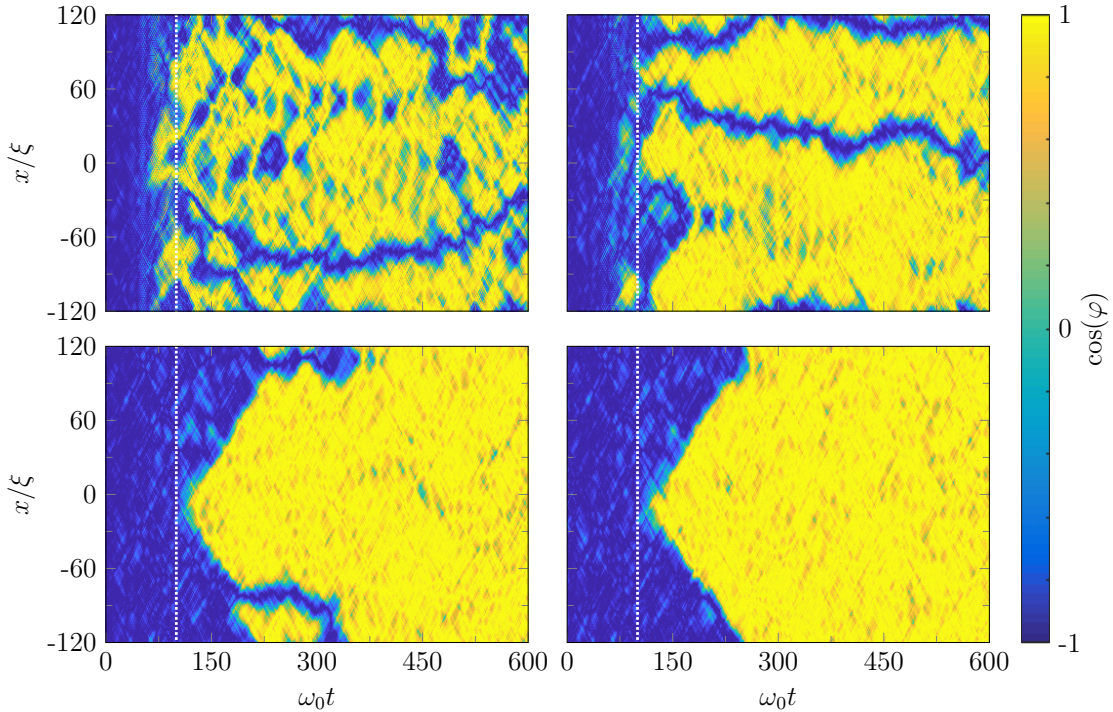


Figure 3.4: The evolution of $\cos(\varphi)$ for a range of values of the damping parameter, γ . The system is prepared in a stable, thermal state, which is converted to a metastable state by means of the control parameter $\alpha(t)$ (see Eq. (3.25)). Here, the vacuum switch occurs about $\omega_0 t = 100$ (white, vertical line), with switch duration $\omega_0 \tau = 5$. The top row, with $\gamma = 0.005$ (left) and $\gamma = 0.01$ (right), shows no evidence of bubble nucleation. The second row, with $\gamma = 0.02$ (left) and $\gamma = 0.03$ (right), clearly shows bubbles nucleating. The final profile is indistinguishable from a static-potential nucleation event. Here, $\epsilon = 0.05$, $\lambda = 1.5$, $\omega = 5\omega_0$ and $T = 0.25T_{\text{CO}}$.

In order to make a quantitative comparison between the oscillatory and static potentials,

we examine the rate of false vacuum decay, Γ , for each. We obtain this via the methodology of Section 2.5, but in light of the instability, raise Δ from 0.2 to 0.9. The decay rate is plotted as a function of damping in Figure 3.5, for a range of modulation frequencies and temperatures.

As expected from both the theoretical discussion of Section 3.4 and the preliminary results of Figure 3.4, the decay rate observed in the presence of the oscillatory potential converges to that of the stationary potential; the higher the modulation frequency, the less dissipation required to achieve this. Furthermore, the values of γ at which agreement is found are suitably consistent with Equation (3.24) and Figure 3.2.

For the parameter space explored in this section, the resonance band always resides below the momentum cutoff, k_{cut} . The question of what happens when the resonance lies significantly above k_{cut} is left open.

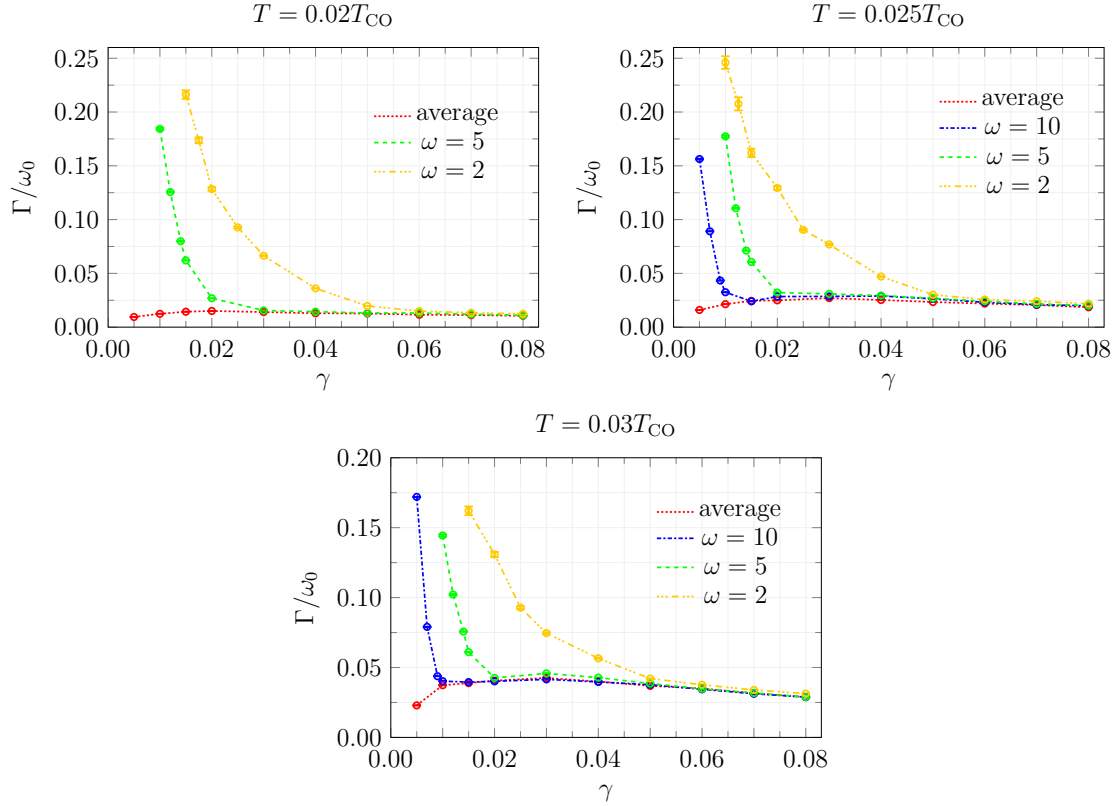


Figure 3.5: The rate of vacuum decay, Γ , as a function of the damping parameter, γ , for both the oscillatory potential, V_{osc} , with a range of modulation frequencies, and the static potential, V_{stat} . At small γ , the values of Γ for each oscillatory potential are significantly larger than those of the static potential. As γ rises, the curves converge. Here, $\epsilon = 0.05$ and $\lambda = 1.5$.

3.7 Experimental Realization

As in Chapter 2, we favour the experimental setups of Fialko *et al.* [39, 41]. One such example involves tuning the interactions between two Zeeman states of ^{41}K , using a Feshbach resonance to achieve the required close-to-zero inter-component scattering length. Assuming an intra-component scattering length of $a_s = 60$ Bohr radii, suitable experimental parameters would be 2.4×10^4 atoms in a quasi-1D optical trap [111] of length $218\text{ }\mu\text{m}$ and transverse frequency $\omega_\perp = 2\pi \times 428\text{ Hz}$. Here, the characteristic frequency ω_0 takes a value around $2\pi \times 300\text{ Hz}$, which satisfies the constraint $\omega_0 \lesssim \omega_\perp$. In addition, the interaction parameter $\zeta = (\rho_0\xi)^{-2} = 10^{-4}$, and the cross-over temperature $T_{CO} = 44\text{ }\mu\text{K}$. In this context, the results of Figure 3.5 correspond to temperatures of 28.8 nK , 36 nK and 43.1 nK . For these parameters, the bubbles in Figures 3.4 and 3.5 nucleate around 25 milliseconds after the potential is rendered metastable.

Another realisation could be achieved with two Zeeman states of ^7Li . In this case, as mentioned in Section 2.6, the intra-component scattering lengths of each state varies, requiring our analysis to be adjusted. However, using the mean scattering length $a_s = 10$ Bohr radii as a guide, a gas of 4.8×10^4 atoms in a trap of length $102\text{ }\mu\text{m}$, with transverse frequency $\omega_\perp = 2\pi \times 16.1\text{ kHz}$, has cross-over temperature $T_{CO} = 77.3\text{ }\mu\text{K}$, interaction parameter $\zeta = 2.5 \times 10^{-5}$, and frequency scale $\omega_0 = 2\pi \times 8.06\text{ kHz}$.

Whilst we have shown in this work that thermal damping can, in principle, suppress the unwanted resonance effects, this viability of this solution rests on the experimental value of γ . For equilibrium experiments, γ can be predicted *a priori* within the SPGPE theory [88, 91], and near-equilibrium experiments have been quantitatively described using this *a priori* value of γ [103]. However, further from equilibrium, SPGPE studies have typically achieved a better match to experiments by treating γ as a free parameter that may vary significantly from the *a priori* value. Effective γ values up to $\gamma = 0.02$ have been employed to match experiments in this way [101, 102, 104].

In the experiments proposed here, bubbles nucleate from a thermal equilibrium state that has been raised to metastability by our control parameter protocol. This would appear to be a reasonably near-equilibrium scenario up until the point a bubble is nucleated and begins to grow. With the above example experimental parameters for ^{41}K , the *a priori* prediction for our two-component SPGPE model is $2.5 \times 10^{-5} \leq \gamma \leq 4.7 \times 10^{-5}$. This stated range includes the temperature difference from $0.02T_{CO}$ to $0.03T_{CO}$, and the difference between the “bare” rate and the rate adjusted by the Lerch transcendent formula of Refs. [88, 105, 91]. In practice, the adjustment to the “bare” rate is small (of order 1) for these parameters. For ^7Li the range is $3.4 \times 10^{-6} \leq \gamma \leq 1.2 \times 10^{-5}$. This suggests suppression of the resonance by thermal damping would not be achieved. However, this conclusion

rests on the model we employed and the assumption that the scenario is sufficiently near-equilibrium for the *a priori* prediction of γ to be relevant. As mentioned in the previous paragraph, effective γ values that would be sufficient to suppress some resonances have been used in previous SPGPE modelling of non-equilibrium experiments. Furthermore, as stated in Section 3.4, it is possible that by raising the modulation frequency beyond the remit of the SPGPE, less damping may be required to erase the instability than observed in this chapter. Additional considerations outside our model that might affect this conclusion include three-dimensional effects in the quasi-condensate not captured by our quasi-one-dimensional model, energy-damping terms due to scattering not captured by our simple-growth SPGPE model [116], and the possibility of the resonance driving dynamics of the thermal cloud not captured in the SPGPE model. These may all alter the effective γ value.

3.8 Conclusion

In this chapter, we showed that by taking into account dissipative effects, first order vacuum decay can be recovered in the presence of the unstable, oscillatory potential. We first carried out a theoretical analysis, to locate the parametric resonance band and determine the dependence of its peak value on the damping parameter, γ . We then went on to model the system numerically. The results of this aligned well with predictions; at low values of γ , we observed disorder, but upon raising the damping rate, bubble nucleation prevailed.

Despite our success in evading the instability, our results suggest that in practice, the oscillatory potential is unlikely to yield bubble growth. The damping rates required to suppress the instability are significantly above any measured or predicted value. Some hope remains, since all existing measurements of γ were taken in equilibrium systems. Therefore, before proceeding, it would be worthwhile to measure γ in a similar, non-equilibrium system.

Chapter 4

Simulating False Vacuum Decay in a Spin-1 Bose Gas at Zero Temperature

4.1 Introduction

With lingering instabilities casting doubt on the viability of the two-component system, it would be desirable to find an ultracold atom system able to simulate vacuum decay in the absence of a modulating microwave field. In this chapter, we propose such an alternative; a three level system with sophisticated external coupling fields. The inclusion of an additional component introduces a number of complexities, which we navigate to achieve bubble nucleation. Furthermore, by examining the rate of vacuum decay, we show this first-order transition to occur in the manner of a Klein-Gordon system. In contrast to previous chapters, here we adopt a zero-temperature approach.

4.2 System

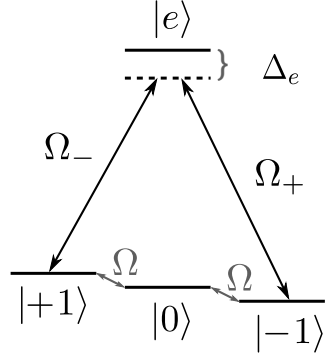


Figure 4.1: A level coupling diagram of the spin-1 system. Here, states $|+1\rangle$ and $|0\rangle$, and states $|0\rangle$ and $| -1 \rangle$, are coupled by a resonant RF beam of frequency ω_q , with Rabi frequency Ω . States $|+1\rangle$ and $| -1 \rangle$ interact via two-photon Raman coupling, induced by off-resonant optical beams with Rabi frequencies Ω_{\pm} , zero two-photon detuning, and detuning Δ_e from the excited state $|e\rangle$.

Here, we consider a one-dimensional, homogeneous condensate of alkali atoms, occupying their $F = 1$ hyperfine ground state manifold. Such a system has three internal spin states; $|m_F\rangle = | -1 \rangle, |0\rangle, | +1 \rangle$, which we refer to interchangeably as ψ_{m_F} , or more compactly; $\psi = (\psi_{-1}, \psi_0, \psi_{+1})^T$. The relevant dimensionless spin matrices are then:

$$F_x = \frac{1}{\sqrt{2}} \begin{pmatrix} 0 & 1 & 0 \\ 1 & 0 & 1 \\ 0 & 1 & 0 \end{pmatrix}, \quad F_y = \frac{1}{\sqrt{2}i} \begin{pmatrix} 0 & 1 & 0 \\ -1 & 0 & 1 \\ 0 & -1 & 0 \end{pmatrix}, \quad F_z = \begin{pmatrix} 1 & 0 & 0 \\ 0 & 0 & 0 \\ 0 & 0 & -1 \end{pmatrix},$$

$$F_+ = \sqrt{2} \begin{pmatrix} 0 & 1 & 0 \\ 0 & 0 & 1 \\ 0 & 0 & 0 \end{pmatrix}, \quad F_- = \sqrt{2} \begin{pmatrix} 0 & 0 & 0 \\ 1 & 0 & 0 \\ 0 & 1 & 0 \end{pmatrix}. \quad (4.1)$$

We assume states to be intrinsically coupled via rotationally-invariant dipole-dipole interactions, as described by the quartic Hamiltonian:

$$H_{\text{collision}} = \frac{1}{2}g(\psi^\dagger\psi)^2 + \frac{1}{2}g'(\psi^\dagger\mathbf{F}\psi)^2, \quad (4.2)$$

$$= \frac{1}{2}g(\psi^\dagger\psi)^2 + \frac{1}{2}g'\left[(\psi^\dagger F_x\psi)^2 + (\psi^\dagger F_y\psi)^2 + (\psi^\dagger F_z\psi)^2\right]. \quad (4.3)$$

For a one-dimensional system, the scattering parameters of the above are given by:

$$g = \frac{2}{3}\hbar\omega_r(a_0 + 2a_2), \quad g' = \frac{2}{3}\hbar\omega_r(a_2 - a_0), \quad (4.4)$$

where $a_{\mathcal{F}}$ is the s-wave scattering length of total spin channel \mathcal{F} [96], and ω_r is the trap frequency of the symmetric transverse confinement.

The degeneracy between components is lifted by a static magnetic field B_z along the z axis, as described by the Zeeman Hamiltonian operator¹:

$$\hat{H}_{\text{Zeeman}} = \hbar\omega_l F_z + \hbar\omega_q F_z^2, \quad (4.5)$$

$$= \hbar \begin{pmatrix} \omega_q + \omega_l & 0 & 0 \\ 0 & 0 & 0 \\ 0 & 0 & \omega_q - \omega_l \end{pmatrix}. \quad (4.6)$$

Here, $\omega_l = g_F\mu_B B_z/\hbar$, and ω_q is the quadratic Zeeman shift, as defined in Section 1.5.6. We label the linear and quadratic terms of Equation (4.5) as \hat{H}_{LZ} and \hat{H}_{QZ} , respectively. Note that any Hamiltonian of the form:

$$\hat{H}_{\text{diagonal}} = \hbar \begin{pmatrix} a & 0 & 0 \\ 0 & 0 & 0 \\ 0 & 0 & b \end{pmatrix}, \quad (4.7)$$

may be absorbed into the Zeeman Hamiltonian via the transformations:

$$\omega_l \rightarrow \omega_l + \frac{1}{2}(a - b), \quad (4.8)$$

$$\omega_q \rightarrow \omega_q + \frac{1}{2}(a + b). \quad (4.9)$$

We propose the states be extrinsically coupled by both radio frequency fields (RF coupling) and by optical fields in a two-photon Raman scheme (Raman coupling). The RF mixing, which acts to couple states $| -1 \rangle \leftrightarrow | 0 \rangle$ and $| 0 \rangle \leftrightarrow | +1 \rangle$, is provided by a beam along the z -axis, tuned to the linear Zeeman frequency, ω_l . The RF Hamiltonian operator is then:

$$\hat{H}_{\text{RF}} = -\mu_B \mathbf{F} \cdot \mathbf{B}, \quad (4.10)$$

where the magnetic field, \mathbf{B} , is polarised along the x -axis:

$$\mathbf{B} = \frac{1}{2}(\mathcal{B}e^{-i\omega_l t} + \mathcal{B}^*e^{i\omega_l t})\mathbf{e}_x. \quad (4.11)$$

¹Note the inclusion of a hat on the Zeeman Hamiltonian. In this chapter, hats will be used to distinguish between Hamiltonian densities, like $H_{\text{collision}}$, and Hamiltonian density operators, like \hat{H}_{Zeeman} .

States $| -1 \rangle$ and $| +1 \rangle$ interact via an excited state, $\psi_e = | e \rangle$, with energy E_e , by means of a three-level A scheme, as shown in Figure 4.1. This excited state is actually the $m_F = 0$ state of the $F = 2$ manifold [117]. To achieve this, a pair of optical beams are also applied along the z -axis, which couple to the electric dipole moment, \mathbf{d} , of the wave function ψ , giving rise to the Raman Hamiltonian operator:

$$\hat{H}_{\text{Ram}} = -\mathbf{d} \cdot \mathbf{E}. \quad (4.12)$$

Here, the total electric field is given by:

$$\mathbf{E} = \frac{1}{2} (\mathcal{E}_+ e^{-i\omega_+ t} + \mathcal{E}_+^* e^{i\omega_+ t}) \mathbf{e}_+ + \frac{1}{2} (\mathcal{E}_- e^{-i\omega_- t} + \mathcal{E}_-^* e^{i\omega_- t}) \mathbf{e}_-, \quad (4.13)$$

where \mathbf{e}_\pm are unit vectors in the polarisation directions. The dipole strengths are given by:

$$d_{i,j}^\pm = \langle \psi_j | \mathbf{d} \cdot \mathbf{e}_\pm | \psi_i \rangle, \quad (4.14)$$

where the polarisation is chosen such that $d_{+1,e}^+ = d_{-1,e}^- = 0$. As shown in Figure 4.1, the beam polarised in the \mathbf{e}_+ direction then serves to couple states $| -1 \rangle$ and $| e \rangle$, and the beam polarised in the \mathbf{e}_- direction couples states $| +1 \rangle$ and $| e \rangle$.

The total mixing Hamiltonian operator, including the linear Zeeman term, \hat{H}_{LZ} , for latter convenience, is then given by:

$$\hat{H}_{\text{mix}_e} = \begin{pmatrix} & +1 & 0 & -1 & e \\ +1 & \hbar\omega_l & V_{\text{RF}} & 0 & V_- \\ 0 & V_{\text{RF}}^* & 0 & V_{\text{RF}} & 0 \\ -1 & 0 & V_{\text{RF}}^* & -\hbar\omega_l & V_+ \\ e & V_-^* & 0 & V_+^* & E_e \end{pmatrix}, \quad (4.15)$$

where indices have been highlighted for clarity. Here, the RF mixing matrix elements are given by:

$$V_{\text{RF}} = -\frac{1}{2\sqrt{2}} \mu_B (\mathcal{B} e^{-i\omega_l t} + \mathcal{B}^* e^{i\omega_l t}), \quad (4.16)$$

and the optical matrix elements are as follows:

$$V_- = -\frac{1}{2} (d_{+1,e}^- \mathcal{E}^- e^{-i\omega_- t} + d_{+1,e}^{-*} \mathcal{E}^{-*} e^{i\omega_- t}), \quad (4.17)$$

$$V_+ = -\frac{1}{2} (d_{-1,e}^+ \mathcal{E}^+ e^{-i\omega_+ t} + d_{-1,e}^{+*} \mathcal{E}^{+*} e^{i\omega_+ t}). \quad (4.18)$$

Ultimately, we wish to simplify \hat{H}_{mix} by making the rotating wave approximation [118, 77].

In order to prepare for this, we make the change of basis:

$$\psi_j \rightarrow \psi_j e^{-i\omega_j t}, \quad j = \{-1, 0, +1, e\}. \quad (4.19)$$

Then, matrix (4.15) becomes:

$$\hat{H}_{\text{mix}_e} = \begin{pmatrix} \hbar(\omega_l - \omega_{+1}) & V_{\text{RF}} e^{i(\omega_{+1} - \omega_0)t} & 0 & V_- e^{i(\omega_{+1} - \omega_e)t} \\ V_{\text{RF}}^* e^{i(\omega_0 - \omega_{+1})t} & -\hbar\omega_0 & V_{\text{RF}} e^{i(\omega_0 - \omega_{-1})t} & 0 \\ 0 & V_{\text{RF}}^* e^{i(\omega_{-1} - \omega_0)t} & -\hbar(\omega_l + \omega_{-1}) & V_+ e^{i(\omega_{-1} - \omega_e)t} \\ V_-^* e^{i(\omega_e - \omega_{+1})t} & 0 & V_+^* e^{i(\omega_e - \omega_{-1})t} & E_e - \hbar\omega_e \end{pmatrix}. \quad (4.20)$$

Note the distinction between ω_{\pm} and $\omega_{\pm 1}$. A simple regime occurs when we choose:

$$\omega_l = (\omega_+ - \omega_-)/2, \quad (4.21)$$

$$\omega_{+1} = \omega_l, \quad (4.22)$$

$$\omega_0 = 0, \quad (4.23)$$

$$\omega_{-1} = -\omega_l, \quad (4.24)$$

$$\omega_e = (\omega_+ + \omega_-)/2. \quad (4.25)$$

In this case, the above reduces to:

$$\hat{H}_{\text{mix}_e} = \begin{pmatrix} 0 & V_{\text{RF}} e^{i\omega_l t} & 0 & V_- e^{-i\omega_- t} \\ V_{\text{RF}}^* e^{-i\omega_l t} & 0 & V_{\text{RF}} e^{i\omega_l t} & 0 \\ 0 & V_{\text{RF}}^* e^{-i\omega_l t} & 0 & V_+ e^{-i\omega_+ t} \\ V_-^* e^{i\omega_- t} & 0 & V_+^* e^{i\omega_+ t} & \hbar\Delta_e \end{pmatrix}, \quad (4.26)$$

where we have introduced the excited state detuning:

$$\hbar\Delta_e = E_e - \hbar(\omega_+ + \omega_-)/2. \quad (4.27)$$

Note that to avoid population of $|e\rangle$, the detuning Δ_e should be large compared to relevant atomic linewidths [119]. By averaging over timescales longer than $2\pi/\omega_l$, we arrive at:

$$\hat{H}_{\text{RWA}} = \frac{\hbar}{2} \begin{pmatrix} 0 & \Omega/\sqrt{2} & 0 & \Omega_-^* \\ \Omega^*/\sqrt{2} & 0 & \Omega/\sqrt{2} & 0 \\ 0 & \Omega^*/\sqrt{2} & 0 & \Omega_+^* \\ \Omega_- & 0 & \Omega_+ & 2\Delta_e \end{pmatrix}. \quad (4.28)$$

Adiabatic elimination of the excited state (setting $\dot{\psi}_e = 0$) gives:

$$\hat{H}_{\text{mix}} = \frac{\hbar}{2} \begin{pmatrix} -\frac{|\Omega_-|^2}{2\Delta_e} & \frac{\Omega}{\sqrt{2}} & -\frac{\Omega^* \Omega_+}{2\Delta_e} \\ \frac{\Omega^*}{\sqrt{2}} & 0 & \frac{\Omega}{\sqrt{2}} \\ -\frac{\Omega_+^* \Omega_-}{2\Delta_e} & \frac{\Omega^*}{\sqrt{2}} & -\frac{|\Omega_+|^2}{2\Delta_e} \end{pmatrix}. \quad (4.29)$$

By making transformation (4.9) from the outset, with $a = -\frac{|\Omega_-|^2}{2\Delta_e}$ and $b = -\frac{|\Omega_+|^2}{2\Delta_e}$, the diagonal terms of \hat{H}_{mix} vanish. Then for real Ω and Ω_{\pm} , matrix (4.29) reduces to:

$$\hat{H}_{\text{mix}} = \frac{\hbar}{2} \begin{pmatrix} 0 & \frac{\Omega}{\sqrt{2}} & -\frac{\Omega_+ \Omega_-}{2\Delta_e} \\ \frac{\Omega}{\sqrt{2}} & 0 & \frac{\Omega}{\sqrt{2}} \\ -\frac{\Omega_+ \Omega_-}{2\Delta_e} & \frac{\Omega}{\sqrt{2}} & 0 \end{pmatrix}, \quad (4.30)$$

or more compactly:

$$\hat{H}_{\text{mix}} = \frac{1}{2} \hbar \Omega F_x + \frac{1}{2} \hbar \kappa (F_+^2 + F_-^2), \quad (4.31)$$

where $\kappa = -\frac{\Omega_+ \Omega_-}{4\Delta_e}$.

It is convenient to gather the interaction terms together into a single potential function:

$$\begin{aligned} V_{\text{int}}(\psi^\dagger, \psi) &= -\mu \psi^\dagger \psi + H_{\text{collision}} + \psi^\dagger \hat{H}_{\text{QZ}} \psi + \psi^\dagger \hat{H}_{\text{mix}} \psi, \\ &= -\mu \psi^\dagger \psi + \frac{1}{2} g (\psi^\dagger \psi)^2 + \frac{1}{2} g' (\psi^\dagger \mathbf{F} \psi)^2 + \hbar \omega_q (\psi^\dagger F_z^2 \psi) \\ &\quad + \frac{1}{2} \hbar \Omega \psi^\dagger F_x \psi + \frac{1}{2} \hbar \kappa \psi^\dagger (F_+^2 + F_-^2) \psi, \end{aligned} \quad (4.32)$$

so that the total Hamiltonian becomes:

$$H = \psi^\dagger \left[-\frac{\hbar^2}{2m} \frac{\partial^2}{\partial x^2} \right] \psi + V_{\text{int}}(\psi^\dagger, \psi). \quad (4.33)$$

4.3 Rescaling

Once again, it is convenient to work in dimensionless units. We make the usual transformations:

$$x = \xi \tilde{x}, \quad t = \omega_0^{-1} \tilde{t}, \quad \psi = \rho_0^{1/2} \tilde{\psi}, \quad V_{\text{int}} = \hbar \omega_0 \rho_0 \tilde{V}_{\text{int}}, \quad (4.34)$$

as introduced in Section 2.3. Here we leave the characteristic density scale, ρ_0 , unspecified until Section 4.4. The above transformations naturally give rise to additional rescalings:

$$\omega_q = \omega_0 \tilde{\omega}_q, \quad \mu = g \rho_0 \tilde{\mu}. \quad (4.35)$$

The Hamiltonian then reduces to:

$$\hat{H} = \tilde{\psi}^\dagger \left[-\frac{1}{2} \frac{\partial^2}{\partial \tilde{x}^2} \right] \tilde{\psi} + \tilde{V}_{\text{int}}(\tilde{\psi}^\dagger, \tilde{\psi}), \quad (4.36)$$

where,

$$\begin{aligned} \tilde{V}_{\text{int}}(\tilde{\psi}^\dagger, \tilde{\psi}) = & -\tilde{\mu} \tilde{\psi}^\dagger \tilde{\psi} + \frac{1}{2} (\tilde{\psi}^\dagger \tilde{\psi})^2 + \frac{1}{2} \frac{g'}{g} (\tilde{\psi}^\dagger \mathbf{J} \tilde{\psi})^2 + \tilde{\omega}_q (\tilde{\psi}^\dagger J_z^2 \tilde{\psi}) \\ & + \frac{1}{2} \epsilon^2 \tilde{\psi}^\dagger J_x \tilde{\psi} - \frac{1}{8} \epsilon^2 \lambda^2 \tilde{\psi}^\dagger (J_+^2 + J_-^2) \tilde{\psi}. \end{aligned} \quad (4.37)$$

Above, we have reparameterized the mixing components in terms of the dimensionless parameters:

$$\epsilon^2 = \frac{\hbar \Omega}{g \rho}, \quad \lambda^2 = \frac{\Omega_+ \Omega_-}{\Omega \Delta_e}. \quad (4.38)$$

4.4 Ground States

Given the complexity of Equation (4.32), locating the ground states of V_{int} is nontrivial. In order to identify and classify the stationary states, we make the parameterisation of Kawaguchi and Ueda [96]:

$$\psi_{\pm 1} = \sqrt{\rho} \zeta_{\pm 1} e^{i(\theta \pm \varphi)}, \quad (4.39)$$

$$\psi_0 = \sqrt{\rho} \zeta_0, \quad (4.40)$$

where $0 \leq \theta, \varphi \leq \pi$. Here, ρ is the total mass density and ζ_j quantify the proportion of mass in each component. The coordinates $(\zeta_{-1}, \zeta_0, \zeta_{+1})$ then lie on a sphere of radius 1:

$$\zeta_{+1}^2 + \zeta_0^2 + \zeta_{-1}^2 = 1. \quad (4.41)$$

The magnetization in the z -direction, $m_z = \psi^\dagger F_z \psi$, can be expressed in terms of ζ_j as follows:

$$m_z = \zeta_{+1}^2 - \zeta_{-1}^2. \quad (4.42)$$

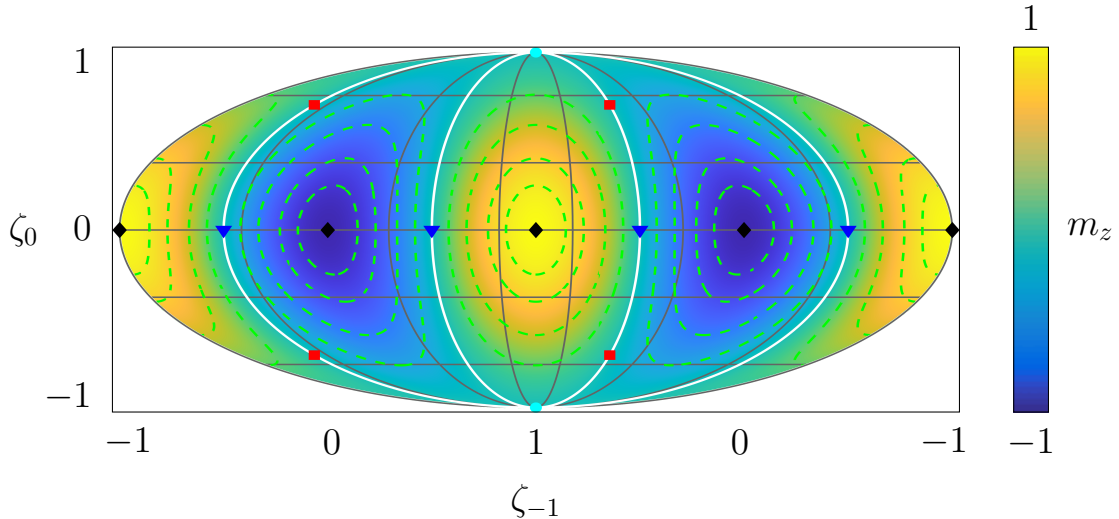


Figure 4.2: The Mollweide projection of the magnetization, $m_z = \zeta_{+1}^2 - \zeta_{-1}^2$, about the sphere $\zeta_{+1}^2 + \zeta_0^2 + \zeta_{-1}^2 = 1$. Note that the ζ_{-1} -axis corresponds to the equator, but is displayed below the plot to avoid congestion. Coloured markers are used to highlight magnetic phases; black diamonds indicate ferromagnetic coordinates, dark blue triangles indicate anti-ferromagnetic coordinates, and light blue circles distinguish the poles. In addition, white contours highlight the broken-axisymmetric phase. The minima of V_{nm} , marked by red squares for the parameters of Figure 4.3, lie on these contours. The dashed green curves show additional contours of constant magnetization.

The magnetization of the ζ -sphere is plotted in Figure 4.2, with key magnetic phases highlighted. More specifically, this figure shows the Mollweide projection of m_z , as defined in Section 1.7.3. The system is in a ferromagnetic (F) phase when $m_z = \pm 1$, an antiferromagnetic (AF) phase when $m_z = 0$ and $\zeta_0 = 0$, and a polar (P) phase when $m_z = 0$ and $\zeta_0 = \pm 1$. The remaining coordinates on the contours of zero magnetization are classified as broken-axisymmetric (BA).

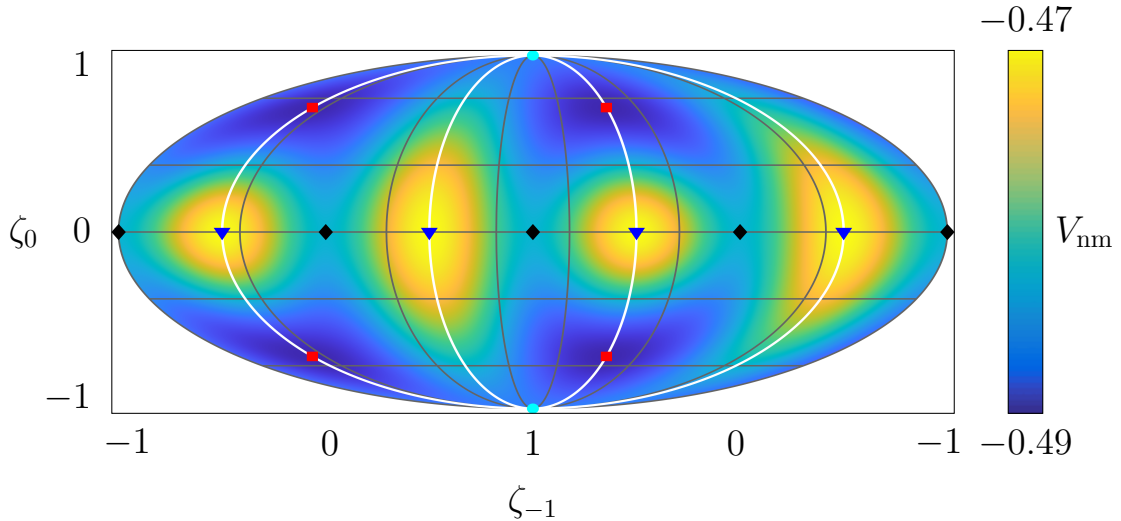


Figure 4.3: The Mollweide projection of the interaction potential in the absence of mixing, V_{nm} , with $\theta = 0$. Again, the ζ_{-1} -axis corresponds to the equator, but is displayed below the plot to avoid congestion. The stationary points of V_{nm} align with the magnetic phases highlighted in Figure 4.2, as indicated by the coloured markers. Saddle points lie at the polar (light blue circles) and ferromagnetic (black diamonds) phases, and maxima lie at the antiferromagnetic (dark blue triangles) coordinates. In addition, minima (red squares) lie on the broken-axisymmetric contours (white curves), at coordinates given by Equation (4.44). Here, $g'/g = -0.0256$, $\epsilon = 0.05$, and $\lambda = 1.7$.

The stationary points of the interaction potential align with the magnetic phases. For simplicity, we demonstrate this in the absence of mixing, and consider the potential:

$$V_{\text{nm}} = -\mu\psi^\dagger\psi + \frac{1}{2}g(\psi^\dagger\psi)^2 + \frac{1}{2}g'(\psi^\dagger\mathbf{J}\psi)^2 + \hbar\omega_q(\psi^\dagger J_z^2\psi), \quad (4.43)$$

given in full physical units, which is independent of φ . Only the quadratic Zeeman term depends on θ , via a term proportional to $-\cos(2\theta)$. In line with Kawaguchi and Ueda [96], we assume $g' < 0$, $g > 0$ and $0 < g\omega_q < -2g'$. Under condition (4.41), the two left-most terms of Equation (4.43) are constant in ζ -space, whereas the third term gives rise to saddle points at the polar and ferromagnetic coordinates, and degenerate maxima at the antiferromagnetic coordinates, as shown on the Mollweide projection of V_{nm} in Figure 4.3. Furthermore, in the vicinity of $\theta = \{0, \pi/2, \pi\}$, the quadratic-Zeeman term gives rise to four degenerate minima, which lie along the BA-contours. Given that we are searching for vacuum states, it is these minima that we are most interested in. By examining the derivatives of V_{nm} , for $\theta = \{0, \pi\}$ we find them to be located at:

$$(\zeta_{-1}, \zeta_0, \zeta_{+1}) = (+\zeta, \pm\zeta', +\zeta) \quad \text{and} \quad (\zeta_{-1}, \zeta_0, \zeta_{+1}) = (-\zeta, \pm\zeta', -\zeta), \quad (4.44)$$

where,

$$\zeta = \frac{1}{2} \left(1 + \frac{g\omega_q}{2g'} \right)^{1/2} \quad \text{and} \quad \zeta' = \sqrt{1 - 2\zeta^2}, \quad (4.45)$$

as shown in Figure 4.3. If we instead consider $\theta = \pi/2$, we find the four minima to switch contours and lie at:

$$(\zeta_{-1}, \zeta_0, \zeta_{+1}) = (+\zeta, \pm\zeta', -\zeta) \quad \text{and} \quad (\zeta_{-1}, \zeta_0, \zeta_{+1}) = (-\zeta, \pm\zeta', +\zeta). \quad (4.46)$$

An alternative projection of V_{nm} is shown in the left-hand panel of Figure 4.4. Here, we lift the restrictions on θ and instead fix $\zeta_{\pm 1} = +\zeta$ and $\zeta_0 = +\zeta'$. In line with Figure 4.3, $V_{\text{nm}}(\theta, \varphi)$ is minimized when $\theta = 0$, and also when $\theta = \pi$. A potential barrier at $\theta = \pi/2$ separates the minima; a system initialised on one side of this barrier is unlikely to find its way to the other.

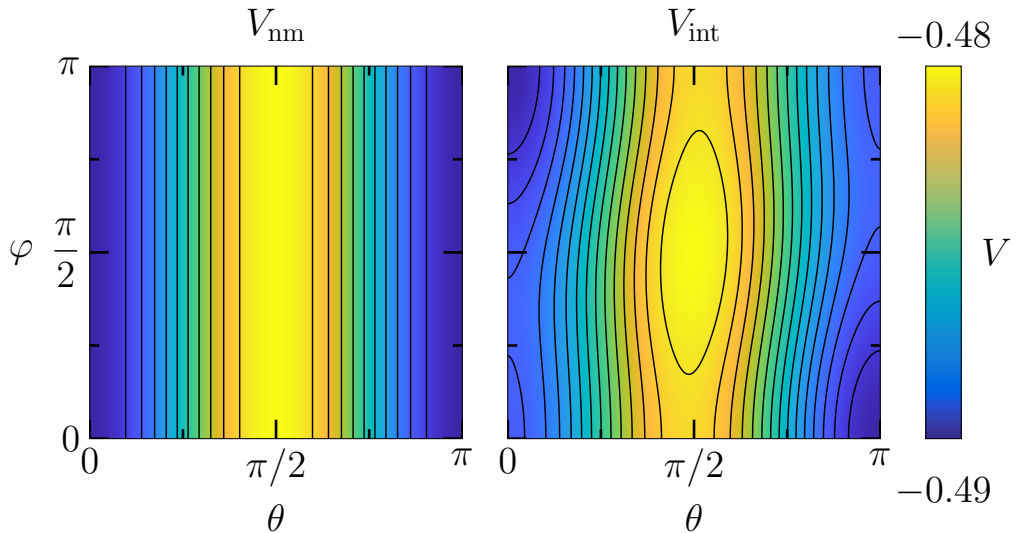


Figure 4.4: Plots of the interaction potential, V , in (θ, φ) -space, with $(\zeta_{+1}, \zeta_0, \zeta_{-1}) = (\zeta, \zeta', \zeta)$. Left: Mixing terms are omitted. There is no φ dependence, and degenerate minima arise at $\theta = 0$ and $\theta = \pi$. Right: Mixing terms are included. We find local minima, or false vacua, at $(\theta, \varphi) = (0, 0)$ and $(\theta, \varphi) = (\pi, \pi)$, and global minima, or true vacua, at $(\theta, \varphi) = (0, \pi)$ and $(\theta, \varphi) = (\pi, 0)$. Here, $g'/g = -0.0256$, $\epsilon = 0.05$, and $\lambda = 1.7$.

The importance of the mixing terms is highlighted in the right-hand panel of Figure 4.4, which shows the equivalent projection of V_{int} . Here, provided that $\epsilon^2 \lesssim -2g'/g$ and $\lambda \gtrsim 1$, the symmetry in φ is broken, giving rise to global minima at $(\theta, \varphi) = (0, \pi)$ and $(\pi, 0)$, and metastable local minima at $(\theta, \varphi) = (0, 0)$ and (π, π) .

Going forward, without loss of generality, we proceed with $(\zeta_{+1}, \zeta_0, \zeta_{-1}) = (\zeta, \zeta', \zeta)$ and choose $\theta = 0$. The characteristic density is then given by the density at the global mini-

mum:

$$\rho_0 = \rho|_{\varphi=\pi}. \quad (4.47)$$

This relates to the chemical potential, μ , of the BA state via:

$$\mu \approx \rho_0(g + g') + \frac{\hbar\omega_q}{2}, \quad (4.48)$$

which allows us to express the dimensionless chemical potential, $\hat{\mu}$, introduced in Section 4.4, as:

$$\hat{\mu} \approx 1 + \frac{g'}{g} + \frac{\hat{\omega}_q}{2}. \quad (4.49)$$

Figure 4.5 shows a slice through $V_{\text{int}}(\theta, \varphi)$ at $\theta = 0$, for a range of λ and ϵ values. Similarly to the spin-1/2 system, the primary role of ϵ is to set the energy difference between minima, and the primary role of λ is to set the size of the potential barrier between $\varphi = 0$ and $\varphi = \pi$. However, in contrast to the spin-1/2 system, there is some crossover between the roles of each here, as can be seen by comparing Figure 4.5 to Figure 2.1.

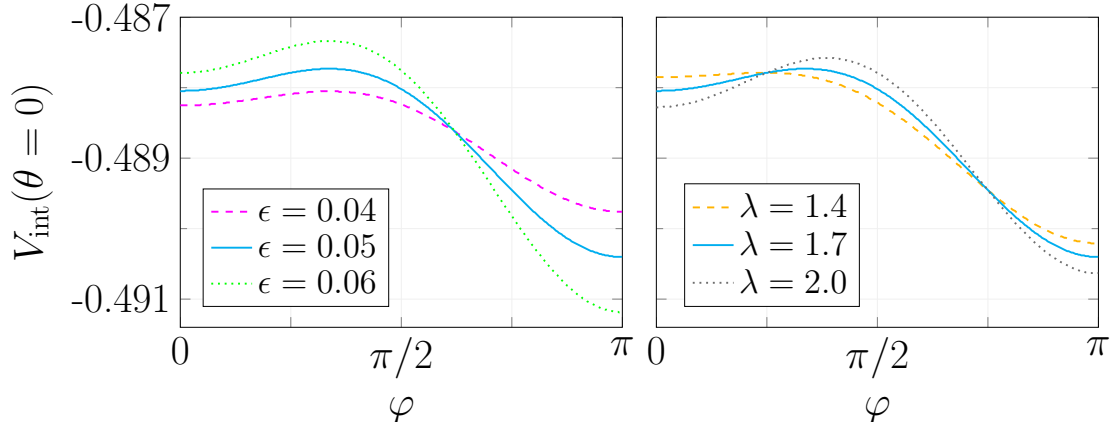


Figure 4.5: The dependence of V_{int} on ϵ and λ at $\theta = 0$. Left: Varying ϵ , with $\lambda = 1.7$. Right: Varying λ , with $\epsilon = 0.05$. Here, ϵ primarily sets the energy difference between global and local minima and λ primarily sets the size of the potential barrier. However, there are some crossover effects. In both panels, $g'/g = -0.0256$.

4.5 Klein-Gordon Limit

The system has Lagrangian density:

$$\mathcal{L} = i\psi^\dagger \frac{\partial\psi}{\partial t} - \frac{1}{2}(\nabla\psi^\dagger) \cdot (\nabla\psi) - V_{\text{int}}. \quad (4.50)$$

We expand the wavefunctions about the false vacuum state, $\varphi = 0$, under the assumption that $\theta \approx 0$, and make the ansatz:

$$\zeta_{\pm 1} = \zeta e^{\pm \sigma/2}, \quad (4.51)$$

where σ represents fluctuations in the relative density of $|+1\rangle$ and $| -1\rangle$. Going forward, we fix ρ and assume $\sigma = \mathcal{O}(\epsilon)$, where $\epsilon \ll 1$.

By substituting Equation (4.51) into \mathcal{L} , to leading order, we obtain:

$$\mathcal{L} = \rho \zeta^2 \left[-2\sigma\dot{\varphi} - (\nabla\varphi)^2 - \frac{\omega_q}{2}\sigma^2 - \sqrt{2}\epsilon^2 \frac{\zeta'}{\zeta} \cos(\varphi) - \epsilon^2 \lambda^2 \sin^2(\varphi) \right]. \quad (4.52)$$

Varying the above with respect to σ yields:

$$\sigma = -\frac{2\dot{\varphi}}{\omega_q}. \quad (4.53)$$

We may then remove the σ -dependence from (4.52). We arrive at:

$$\mathcal{L}_{\text{eff}} = 2\rho\zeta^2 \left[\frac{\dot{\varphi}^2}{2c^2} - \frac{1}{2}(\nabla\varphi)^2 - V_{\text{eff}}(\varphi) \right], \quad (4.54)$$

where $c^2 = \omega_q/2$,

$$V_{\text{eff}} = \epsilon^2 \lambda_c^2 \cos(\varphi) + \frac{1}{2} \epsilon^2 \lambda^2 \sin^2(\varphi), \quad (4.55)$$

and

$$\lambda_c = \left(\frac{1 - g\omega_q/(2g')}{1 + g\omega_q/(2g')} \right)^{1/4}. \quad (4.56)$$

This is the Lagrangian density of a Klein-Gordon field with propagation speed c . Provided that $\lambda > \lambda_c$, the effective potential V_{eff} exhibits a false vacuum state at $\varphi = 0$ and a true vacuum state at $\varphi = \pi$, as shown in Figure 4.6. This is consistent with the findings of Section 4.4. The Klein-Gordon field has mass:

$$m_{\text{eff}}^2(\varphi) = \epsilon^2 \lambda^2 [2 \cos^2(\varphi) - 1] - \epsilon^2 \lambda_c^2 \cos(\varphi). \quad (4.57)$$

In particular, at the false vacuum, $m_{\text{eff}} = \epsilon(\lambda^2 - \lambda_c^2)^{1/2}$. Intermediate steps of this calculation can be found in Appendix D.

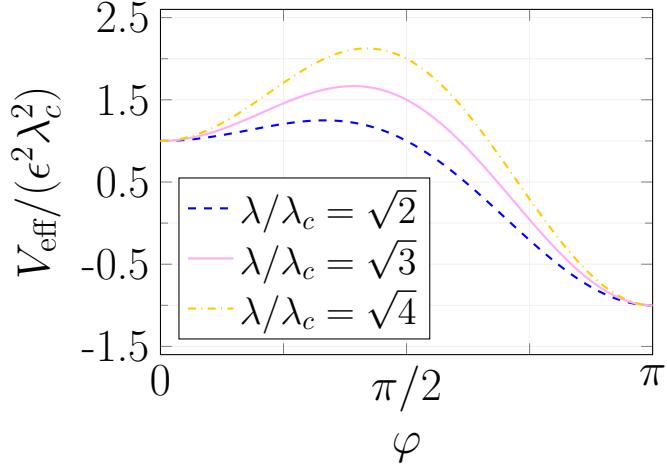


Figure 4.6: The effective Klein-Gordon potential, $V_{\text{eff}}(\varphi)$. A metastable local minimum is located at $\varphi = 0$ and a stable global minimum is located at $\varphi = \pi$. Provided $\lambda > \lambda_c$, a potential barrier separates the stationary points.

4.6 Dispersion Relation

We may use the effective Klein-Gordon Lagrangian, given by Equation (4.54), to approximate the dispersion relation of the spin-1 system in the vicinity of the false-vacuum state. We achieve this by expanding φ about the false vacuum state, $\varphi_{\text{FV}} = 0$:

$$\varphi = \varphi_{\text{FV}} + \delta\varphi, \quad (4.58)$$

where $\delta\varphi$ is a small perturbation. Then:

$$V_{\text{eff}}(\varphi_{\text{FV}} + \delta\varphi) \approx V_{\text{eff}}(\varphi_{\text{FV}}) + (\delta\varphi)V'_{\text{eff}}(\varphi_{\text{FV}}) + \frac{(\delta\varphi)^2}{2}V''_{\text{eff}}(\varphi_{\text{FV}}), \quad (4.59)$$

$$= V_{\text{eff}}(\varphi_{\text{FV}}) + \frac{(\delta\varphi)^2}{2}m_{\text{FV}}^2, \quad (4.60)$$

where $m_{\text{FV}}^2 = m_{\text{eff}}^2(\varphi_{\text{FV}})$. The Lagrangian then transforms as follows:

$$\mathcal{L}_{\text{eff}} = 2\rho\zeta^2 \left[\frac{1}{2c^2} \left(\frac{\partial}{\partial t}(\delta\varphi) \right)^2 - \frac{1}{2}(\nabla(\delta\varphi))^2 - V_{\text{eff}}(\varphi_{\text{FV}}) - \frac{(\delta\varphi)^2}{2}m_{\text{FV}}^2 \right]. \quad (4.61)$$

Varying \mathcal{L}_{eff} with respect to $\delta\varphi$ gives:

$$\left[\frac{1}{c^2} \frac{\partial^2}{\partial t^2} - \nabla^2 + m_{\text{FV}}^2 \right](\delta\varphi) = 0. \quad (4.62)$$

It remains to Fourier transform $\delta\varphi$:

$$\delta\varphi \rightarrow \widehat{\delta\varphi} e^{i(\mathbf{k}\cdot\mathbf{x}-\omega t)}. \quad (4.63)$$

This yields:

$$\left[-\frac{\omega^2}{c^2} + k^2 + m_{\text{FV}}^2 \right] (\widehat{\delta\varphi}) = 0. \quad (4.64)$$

Finally, by recalling that $c^2 = \omega_q/2$, we obtain:

$$\omega(k) = \frac{1}{2} (2\omega_q)^{1/2} (k^2 + m_{\text{FV}}^2)^{1/2}. \quad (4.65)$$

It turns out that by carrying out a full Bogoliubov analysis, as described in Section 1.6.2, a more precise dispersion relation can be derived. By examining the eigenvectors of the Hessian of $V_{\text{int}}(\psi^\dagger, \psi)$, we² find:

$$\omega(k) = \frac{1}{2} (k^2 + 2\omega_q)^{1/2} (k^2 + m_{\text{FV}}^2)^{1/2}. \quad (4.66)$$

Provided that $k \ll (2\omega_q)^{1/2}$, this reduces to the Klein-Gordon result. A comparison of the Klein-Gordon and Bogoliubov dispersion relations is shown in Figure 4.7

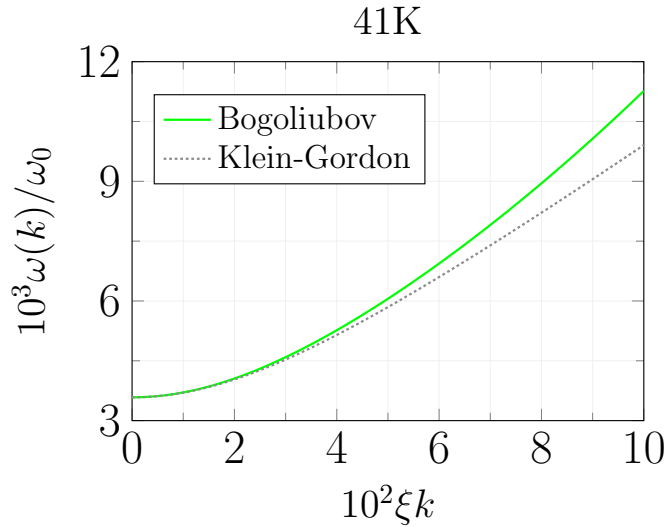


Figure 4.7: A comparison of the Klein-Gordon and Bogoliubov dispersion relations about the false vacuum state for 41K. We find agreement at short wavelengths. Here, $g'/g = -0.0256$, $\epsilon = 0.05$ and $\lambda = 1.42$.

²This analysis was carried out by Ian Moss.

4.7 Numerical Setup

In contrast to Chapters 2-3, we model our one-dimensional spin-1 system using the projected Gross-Pitaevskii equation (PGPE). In physical units:

$$i\hbar \frac{\partial \psi}{\partial t} = \mathcal{P} \left\{ -\frac{\hbar^2}{2m} \frac{\partial^2 \psi}{\partial x^2} + \frac{\partial V_{\text{int}}}{\partial \psi^*} \right\}, \quad (4.67)$$

where $\psi = (\psi_{-1}, \psi_0, \psi_{+1})^\top$. Parameterizations (4.34)-(4.35) yield the corresponding dimensionless equation:

$$i \frac{\partial \tilde{\psi}}{\partial \tilde{t}} = \mathcal{P} \left\{ -\frac{1}{2} \frac{\partial^2 \tilde{\psi}}{\partial \tilde{x}^2} + \frac{\partial \tilde{V}_{\text{int}}}{\partial \tilde{\psi}^*} \right\}. \quad (4.68)$$

We make the Truncated-Wigner approximation (TWA), whereby stochasticity is imprinted into the initial conditions of the system. The initial noise is described by the multivariate normal distribution of a simple harmonic oscillator Wigner function, constructed such that its amplitude matches the vacuum fluctuations in each Bogoliubov mode.

The majority of the fluctuations of the Spin-1 system are in the Bogoliubov modes, $\delta\varphi$, corresponding to the relative-phase direction, φ . Thus, we place noise in these modes only. The dispersion relation of these modes is given by Equation (4.66), and the fluctuations associated with these modes have power spectrum:

$$\langle \delta\varphi(k)\delta\varphi(k') \rangle = \frac{1}{8\rho\zeta^2} \left(\frac{k^2 + 2\omega_q}{k^2 + m_{\text{FV}}^2} \right)^{1/2} \delta_{kk'}. \quad (4.69)$$

We wish to initialise in the BA state, in the vicinity of the false vacuum at $(\theta, \varphi) = (0, 0)$. Thus, in dimensionless units, we set:

$$\psi_{+1}(t=0) = \zeta e^{i\delta\varphi}, \quad (4.70)$$

$$\psi_0(t=0) = \zeta', \quad (4.71)$$

$$\psi_{-1}(t=0) = \zeta e^{-i\delta\varphi}. \quad (4.72)$$

Under the TWA, the projector, \mathcal{P} , of the PGPE acts to eliminate modes with wavenumber $|k| > k_c/2$, where,

$$k_c = \frac{N\pi}{L}, \quad (4.73)$$

L is the length of the spatial lattice, and N is the number of lattice points. In words, k_c is the largest wave number that can be accommodated on the finite-sized grid. This choice of projector ensures that the time evolution of the field may be computed using a Fourier pseudo-spectral method, without any aliasing of the nonlinear terms, as detailed

in Section 1.6.3.

We proceed with the grid-geometry of the spin-1/2 system; a periodic system of size $L = 240\xi$ with grid spacing $\Delta x = 0.4\xi$. The system evolves in time via the fourth-order Runge-Kutta algorithm, with time step $\Delta t = 10^{-4}\omega_0^{-1}$. To reduce the possible parameter space, we fix $\omega_q/\omega_0 = -2g'/(3g)$ and $\epsilon = 0.05$. Finally, we continue to calculate averaged quantities using $\mathcal{N} = 1000$ stochastic realisations.

4.8 Numerical Results

As usual, we first investigated the qualitative behaviour of the system, by examining the spatial profile of $\cos(\varphi)$. We found the global phase of the system to drift as a result of initial energy adjustments. In order to examine φ , it proved necessary to subtract this background effect. Therefore in practice, we output $\varphi = \arg(\psi_{+1}/\psi_0)$. Figure 4.8 shows example realisations of $\cos(\varphi)$ for ${}^7\text{Li}$, with $\lambda = 1.7$ and $\rho\xi = 20$. The top panel shows a selection of $\langle \cos(\varphi) \rangle$ trajectories. In contrast to the spin-1/2 system, each trajectory begins at $\langle \cos(\varphi) \rangle \approx 1$, then drops suddenly towards -1 at a seemingly random time. Figure 4.8 also shows a sample of the $\cos(\varphi)$ profiles from which the trajectories were generated. A single bubble nucleation event is evident in each; true-vacuum regions form locally and expand, eventually undergoing self-collision as a result of the periodic boundaries of the system. Interestingly, energy is released at the collision sites, temporarily restoring a small metastable region. This accounts for the fluctuations in phase that are apparent in post-decay region of the trajectories. Here, the role of the initial noise is clear; in this small sample alone, we observe significant variation in the location and time of bubble nucleation.

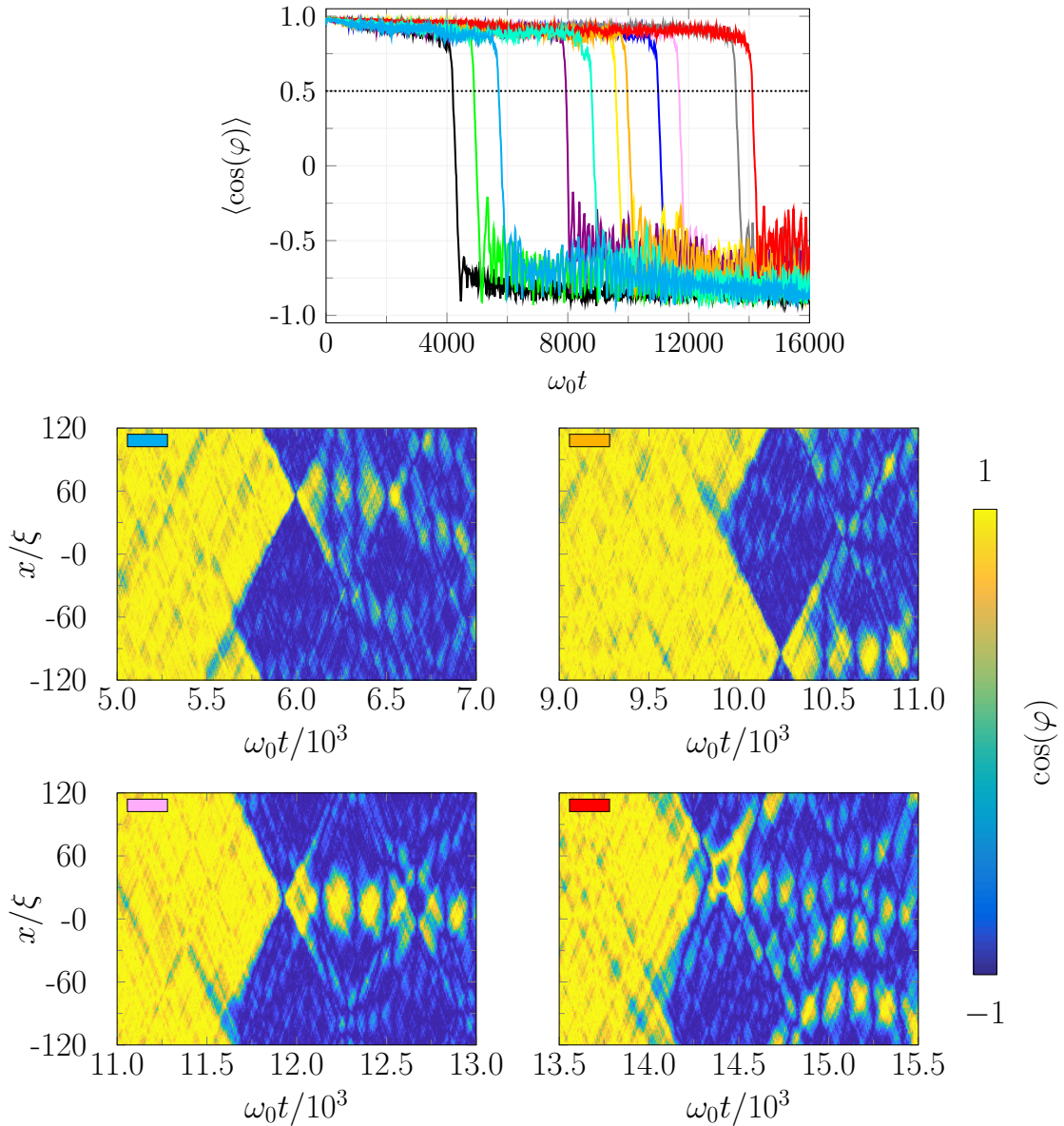


Figure 4.8: Examples of bubble growth for ${}^7\text{Li}$, with $\lambda = 1.7$ and $\rho\xi = 20$. Top: Trajectories of $\langle \cos(\varphi) \rangle$ for 10 simulation runs, where $\langle \dots \rangle$ denotes a spatial average. Bubble growth is characterised by a sudden decrease in $\langle \cos(\varphi) \rangle$ from +1 to -1. Our threshold for bubble nucleation, $\langle \cos(\varphi) \rangle = 0.5$, is shown by a dotted line. Bottom: The evolution of $\cos(\varphi)$ for four example trajectories. The coloured rectangle in the upper left-hand corner of each panel indicates which trajectory the panel corresponds to. Bright yellow indicates a region of false vacuum, whereas dark blue indicates a region of true vacuum.

We calculate the probability, P , of remaining in the false-vacuum state using a similar method to the spin-1/2 system. Here we again set a nucleation threshold, now given by $1 - \Delta$. The survival probability is then given by the proportion of stochastic trajectories yet to fall below the threshold. Henceforth, we set $\Delta = 0.5$. From this, we are able to

extract the rate of false vacuum decay, Γ , again by fitting:

$$P(t) = ae^{-\Gamma t}, \quad (4.74)$$

with freedom in a and Γ . Here, we fit over the region $P > 0.5$, but found results to be robust under reasonable variations in fitting region.

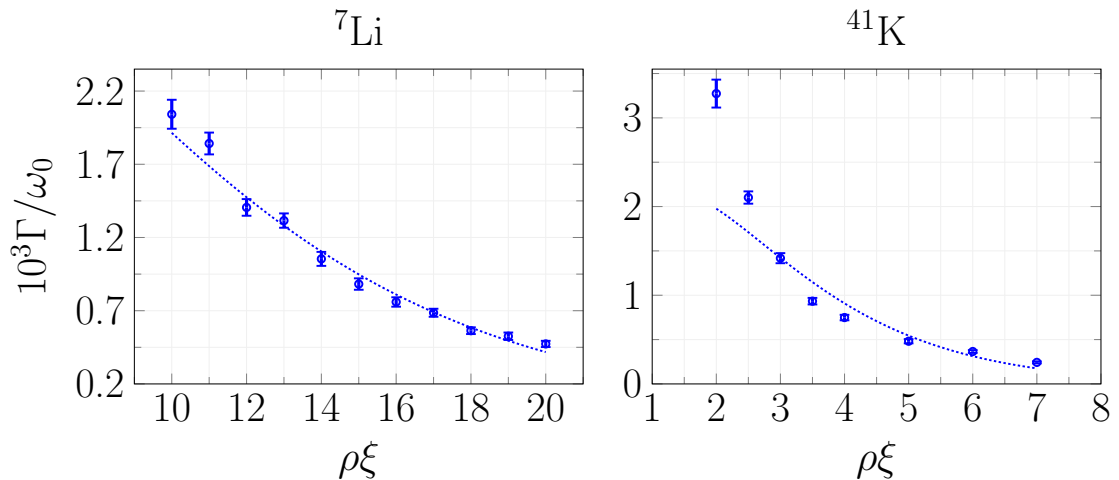


Figure 4.9: The rate of false vacuum decay, Γ , as a function of density, ρ , for two atomic species. The circular markers show the simulated data points, with error bars generated using the bootstrap methodology detailed in Section 1.7.2. The dotted curves show the corresponding instanton predictions, obtained by fitting Equation (4.82) to the data points. For ${}^7\text{Li}$, we found $A' = 0.0018$ and $B' = 0.2216$, and for ${}^{41}\text{K}$, $A' = 0.0043$ and $B' = 0.7351$. Here, $\lambda = 1.42$ and $\epsilon = 0.05$.

For this initial investigation of the spin-1 system, we focused primarily on the dependence of decay rate on density, as explored for ${}^7\text{Li}$ and ${}^{41}\text{K}$ in Figure 4.9. Here, error bars were again computed using the bootstrap resampling approach of Section 1.7.2, with $M = 100$ and $N = 1000$. For both species, we find Γ to decrease as density increases. Predictably, the strength of the exponential fit lessens as Γ increases, signalling deviation from first-order behaviour at lower densities.

We also compared our data to the instanton prediction. Since we are considering a one-dimensional system, for which the false vacuum decays via quantum fluctuations, this takes the form:

$$\Gamma_{\text{inst}} = AS_E[\varphi_b]e^{-S_E[\varphi_b]}, \quad (4.75)$$

as motivated in Section 1.2.2. As usual $S_E[\varphi_b]$ is the Euclidean action evaluated at the bounce. By applying the transformation $t = i\tau$ to Equation (4.54), we find:

$$S_E[\varphi] = 2\rho\xi^2 \int d\tau dx \left\{ \frac{1}{2c^2} \left(\frac{\partial \varphi}{\partial \tau} \right)^2 + \frac{1}{2} \left(\frac{\partial \varphi}{\partial x} \right)^2 + V_{\text{eff}}(\varphi) \right\}. \quad (4.76)$$

If we make the transformations:

$$x' = \epsilon \lambda_c x, \quad t' = c\epsilon \lambda_c t, \quad \lambda' = \lambda/\lambda_c, \quad (4.77)$$

this becomes:

$$S_E[\varphi] = \chi \int d\tau' dx' \left\{ \frac{1}{2} \left(\frac{\partial \varphi}{\partial \tau'} \right)^2 + \frac{1}{2} \left(\frac{\partial x'}{\partial \tau'} \right)^2 + \tilde{V}_{\text{eff}}(\varphi) \right\}, \quad (4.78)$$

where $\chi = 2\rho\zeta^2/c$ and

$$\tilde{V}_{\text{eff}}(\varphi) = \cos(\varphi) + \frac{1}{2} \lambda'^2 \sin^2(\varphi). \quad (4.79)$$

This is precisely the Euclidean action of Ref. [27]³. Thus, similarly to Section 2.5, we use the investigations of Ref. [27] to infer:

$$S_E[\varphi_b] = \chi f(\lambda'), \quad (4.80)$$

where $f(\lambda')$ is some function of $\lambda' = \lambda/\lambda_c$. Whilst we could use the methodology of Ref. [27] to specify $f(\lambda')$, given the renormalisation effects observed throughout Chapter 2, we instead treat f as a λ' -dependent constant, F , and fit:

$$\Gamma_{\text{inst}} = A(F\chi)e^{-F\chi}. \quad (4.81)$$

Furthermore, for our examinations of the relationship between decay rate and density, ζ and c are species-dependent constants. Thus, in practice, we fit:

$$\Gamma_{\text{inst}} = A'\rho e^{-B'\rho}, \quad (4.82)$$

with freedom in A' and B' .

The instanton fits are included alongside the PGPE data in Figure 4.9. We find good agreement between theory and data for ⁷Li, but only reasonable agreement for ⁴¹K. It is possible that the latter could be improved by considering larger values of $\rho\xi$.

³Well almost: Here, $\tilde{V}_{\text{eff}}(\varphi) = \cos(\varphi) + \lambda'^2 \sin^2(\varphi)/2$, whereas in Ref. [27], $V = -1 - \cos(\varphi) + \lambda^2 \sin^2(\varphi)/2$. We are free to shift \tilde{V}_{eff} by -1 without consequence, so this discrepancy is unimportant. Of greater concern is the sign of $\cos(\varphi)$. However, as shown in Ref. [27], the bounce, φ_b , is given by some integral over the region $\varphi = \varphi_{\text{FV}}$ to $\varphi = \varphi_*$ (see Figure 1.3 for a reminder of the definition of φ_*). A quick plot of V and \tilde{V}_{eff} shows the relevant segments of each potential to have equal area; our system is indeed equivalent!

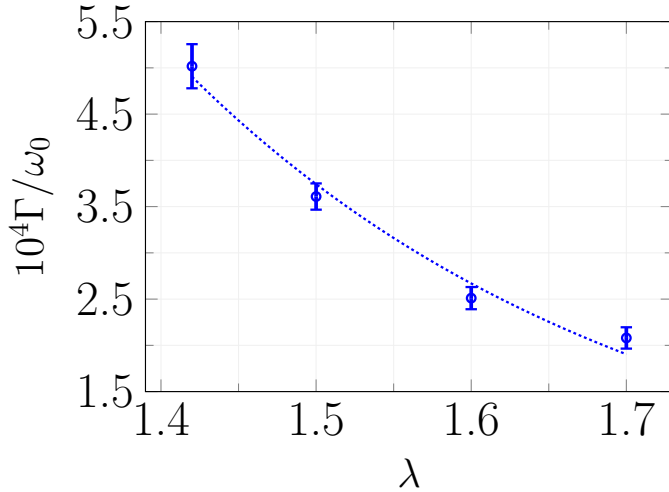


Figure 4.10: The rate of false vacuum decay, Γ , as a function of barrier height, λ , for ${}^7\text{Li}$. The circular markers show the simulated data points, with error bars for $\lambda > 1.42$ given by the 95% confidence intervals of the least squares fit to Equation (4.74). The dotted curve is a guide to the eye; there is not enough data to obtain a valid fit to Equation (4.75). Here, $\rho\xi = 20$ and $\epsilon = 0.05$.

As a sanity check, we also carried out a brief investigation into the relationship between decay rate and λ for ${}^7\text{Li}$, as shown in Figure 4.10. We find Γ to decrease as λ increases. This is to be expected from Figure 4.5 alone; the larger the value of λ , the taller and wider the potential barrier between $\varphi = 0$ and $\varphi = \pi$, and so the more difficult it is to tunnel through. We did not examine enough λ values to deem the effort required to calculate an instanton fit worthwhile. However, this would be an interesting avenue for future work.

4.9 Experimental Realisation

Finally, we comment on the experimental viability of our system. We tabulate relevant physical properties for alkali species with the required property $g'/g < 0$ in Table 4.1. The ground state hyperfine energy splitting, ΔE_{HFS} , which in line with Equation (1.37) satisfies $\Delta E_{\text{HFS}} = 2A_{\text{HFS}}$, determines the magnetic field needed to achieve a given quadratic Zeeman shift, as detailed in Section 1.5.5. While g'/g is fixed by the atomic species, considerable flexibility remains in the tuneable experimental parameters corresponding to our dimensionless parameters.

As an example, the parameters of Figure 4.8 and 4.9 (a), with $\rho\xi = 20$, would correspond to 2400 ${}^7\text{Li}$ atoms in a 260 μm circumference ring trap, with transverse frequency $\omega_r = 2\pi \times 25 \text{ kHz}$ and a bias field of $B_z = 0.39 \text{ Gauss}$. The timescale ω_0^{-1} corresponds to 0.52 ms. The parameters used in 4.9 (b), with $\rho\xi = 7$, would correspond to 840 ${}^{41}\text{K}$ atoms in a 24.4 μm circumference ring trap, with the same transverse frequency and a bias field of

$B_z = 0.23$ Gauss.

Table 4.1: Physical properties used to compute simulation parameters. Scattering lengths were obtained from the table in Ref. [80] and the hyperfine energy splitting values, which here satisfy $\Delta E_{\text{HFS}} = 2A_{\text{HFS}}$, were obtained from Ref. [79]

Species	a_0 (a_{Bohr})	a_2 (a_{Bohr})	g'/g	ΔE_{hfs} (h MHz)
^7Li	23.9	6.9	-0.456	803.5
^{41}K	68.5	63.5	-0.0256	254.0
^{87}Rb	101.8	100.4	-0.0046	6834.7

We assume there to be very wide experimental flexibility in terms of the coupling field Rabi frequencies and detuning (Ω , Ω_{\pm} , Δ_e). In practice, these would need to be tuned to give the desired ϵ and λ , by taking into account the additional smaller light shifts arising from the other states in the upper hyperfine manifold that we neglect here.

We note that the example parameter values suggested above require a very low temperature (2.5 nK for ^7Li and 16.6 nK for ^{41}K) to achieve complete phase coherence across the system in a single-component Bose gas. Crucially, however, the false vacuum state exists in the *relative* phase, and so the relevant condition for coherence is $T < m_{\text{eff}}(\varphi = 0)$, in dimensionless units. This sets the temperature for *relative* phase coherence to 53 nK for ^7Li and 352 nK for ^{41}K . In principle, false vacuum decay should be observable in ^{87}Rb , but we were unable to find a favourable parameter regime, likely as a result of the very small $|g'/g|$ ratio.

4.10 Conclusion

In this chapter, we identified a metastable state of an effective Klein-Gordon field in a radio frequency and optical Raman coupled spin-1 Bose gas. We proceeded to simulate false-vacuum decay in the system and successfully observed first-order behaviour. We went on to compare our results to instanton predictions and found reasonable agreement. Given its freedom from parametric instabilities, this system has a practical advantage over the analogous spin-1/2 setup. Therefore, the preliminary results presented in this chapter show the spin-1 system to be a promising candidate for observing relativistic bubble nucleation in the laboratory.

Chapter 5

Simulating False Vacuum Decay in a Spin-1 Bose Gas at Finite Temperature

5.1 Introduction

Thus far, we have only modelled false vacuum decay in one-dimensional systems. Whilst these are achievable in the laboratory, and economical to simulate, we are limited in the comparisons we can draw between such analogues and our three-dimensional universe. A three-dimensional analogue would be ideal, however such systems are difficult to probe experimentally, and expensive to simulate numerically. Therefore, in this chapter, we explore the middle ground; a two-dimensional Bose gas. We proceed with the spin-1 system of Chapter 4, but return to the finite-temperature approach of Chapters 2-3. We begin with the usual periodic system, but with experimental success on the horizon [54], we go on to investigate the impact of including a trapping potential.

5.2 System

Here, we extend the spin-1 system to two spatial dimensions and modify the Hamiltonian accordingly:

$$H = \psi^\dagger \left[-\frac{\hbar^2}{2m} \nabla^2 \right] \psi + V_{\text{int}}(\psi^\dagger, \psi), \quad (5.1)$$

where ∇ is the two-dimensional gradient operator. On the surface, V_{int} is unchanged, and remains as defined in Equation (4.32). However, the prefactor of the scattering parameters

varies. For a two-dimensional system:

$$g = \left(\frac{8\pi\hbar^3\omega_{\perp}}{3m} \right)^{1/2} (a_0 + 2a_2), \quad g' = \left(\frac{8\pi\hbar^3\omega_{\perp}}{3m} \right)^{1/2} (a_2 - a_0), \quad (5.2)$$

where ω_{\perp} is the trap frequency of the transverse confinement.

5.3 Numerical Setup: Periodic Boundaries

We return to the stochastic projected Gross-Pitaevskii equation (SPGPE), which for the three-component spin-1 system reads:

$$i\hbar \frac{\partial \psi_m}{\partial t} = \mathcal{P} \left\{ (1 - i\gamma) \left[-\frac{\hbar^2}{2m} \nabla^2 \psi_m + \frac{\partial V_{\text{int}}}{\partial \psi_m^\dagger} \right] + \eta_m \right\}, \quad m = -1, 0, +1, \quad (5.3)$$

where as usual, noise is uncorrelated between components:

$$\langle \eta_m^*(\mathbf{r}, t) \eta_{m'}(\mathbf{r}', t') \rangle = 2\gamma\hbar k_B T \delta(\mathbf{r} - \mathbf{r}') \delta(t - t') \delta_{mm'}. \quad (5.4)$$

By making transformations (4.34)-(4.35), we arrive at the dimensionless SPGPE:

$$i \frac{\partial \tilde{\psi}_m}{\partial \tilde{t}} = \mathcal{P} \left\{ (1 - i\gamma) \left[-\frac{1}{2} \tilde{\nabla}^2 \tilde{\psi}_m + \frac{\partial \tilde{V}}{\partial \tilde{\psi}_m^\dagger} \right] + \tilde{\eta}_m \right\}, \quad m = -1, 0, +1. \quad (5.5)$$

Since we are now working in two spatial dimensions, we modify our temperature rescaling in line with Ref. [76] as follows:

$$T = T^* \tilde{T}, \quad (5.6)$$

where $T^* = \hbar\omega_0/k_B$. The dimensionless correlation function must be adjusted accordingly:

$$\langle \tilde{\eta}_m^*(\tilde{\mathbf{r}}, \tilde{t}) \tilde{\eta}_{m'}(\tilde{\mathbf{r}'}, \tilde{t}') \rangle = \frac{2\gamma\tilde{T}}{\tilde{\rho}} \delta(\tilde{\mathbf{r}} - \tilde{\mathbf{r}'}) \delta(\tilde{t} - \tilde{t}') \delta_{mm'}, \quad (5.7)$$

where $\tilde{\rho} = \rho\xi^2$ is the dimensionless density. Consequently, we make a slight modification to the momentum cut-off used in Chapters 2-3. Here, the projector \mathcal{P} serves to disregard modes with momentum $k^2 > k_{\text{cut}}^2$ in dimensionless units, where $k_{\text{cut}} = (2\tilde{T})^{1/2}$. Finally, throughout this work, we fix the dimensionless dissipation parameter at $\gamma = 0.02$. Henceforth, as usual, we omit tildes.

Our baseline simulations use a two-dimensional grid of size $L = L_x = L_y = 300\xi$, with periodic boundaries and grid spacing $\Delta l = \Delta x = \Delta y = 0.4\xi$. We proceed with the fourth-order Runge-Kutta algorithm, but given the increase in computational cost that

comes with an additional spatial dimension, we increase the time step to $\Delta t = 0.04\omega_0^{-1}$. Agreement with tests at $\Delta t = 0.004$ proved the former to be sufficiently small. We set the geometry of V_{int} by fixing $\lambda = 1.7$ and $\epsilon = 0.1$, and as usual fix $\omega_q/\omega_0 = -2g'/(3g)$. In this chapter, we consider only ${}^7\text{Li}$, for which $g'/g = -0.456$. Finally, all average quantities are calculated using a minimum of $\mathcal{N} = 100$ stochastic realisations.

We use a similar initialization protocol as for the spin-1/2 SPGPE simulations; we place the system in a purely stable state and allow it to thermalize. Then, at some time t_0 , the system is coerced into a metastable state, by means of a control parameter:

$$\alpha(t) = \frac{\pi}{2} \left[1 - \tanh \left(\frac{t - t_0}{\tau} \right) \right], \quad (5.8)$$

where τ denotes the duration of the vacuum switch. Note that Equation (5.8) is identical to Equation (3.25). However, here α is incorporated in the RF-mixing term of the interaction potential V_{int} (see Equation (4.32)):

$$V_{\text{RF}} = \frac{1}{2} \epsilon^2 \psi^\dagger J_x \psi \rightarrow \frac{1}{2} \cos(\alpha) \epsilon^2 \psi^\dagger J_x \psi. \quad (5.9)$$

Going forward, we set $t_0 = 200$ and $\tau = 2.5$. The role of $\alpha(t)$ is shown in Figure 5.1.

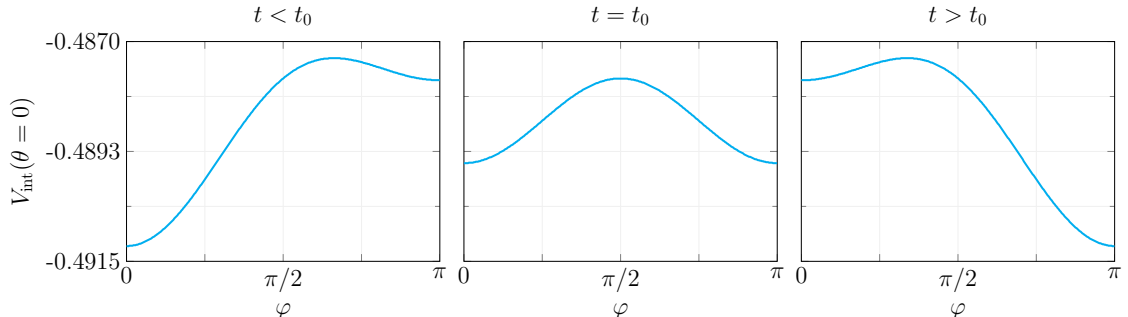


Figure 5.1: The role of the control parameter $\alpha(t)$, as defined in Equation (5.8). Prior to the switching time, t_0 , the potential exhibits a global minimum at $(\theta, \varphi) = (0, 0)$ and a local minimum at $(\theta, \varphi) = (0, \pi)$. Beyond t_0 , we instead find a local minimum at $(\theta, \varphi) = (0, 0)$ and a global minimum at $(\theta, \varphi) = (0, \pi)$. The switch takes place over duration τ .

5.4 Numerical Results: Periodic Boundaries

The evolution of $\cos(\varphi)$ is shown for a single stochastic realisation in Figure 5.2. This behaviour is typical; a bubble of true vacuum nucleates and expands roughly circularly. Further bubbles appear and collide with one another. Late snapshots hint that the likelihood of bubble nucleation may increase in the vicinity of a sufficiently large bubble. However, an investigation into this is beyond the scope of this thesis.

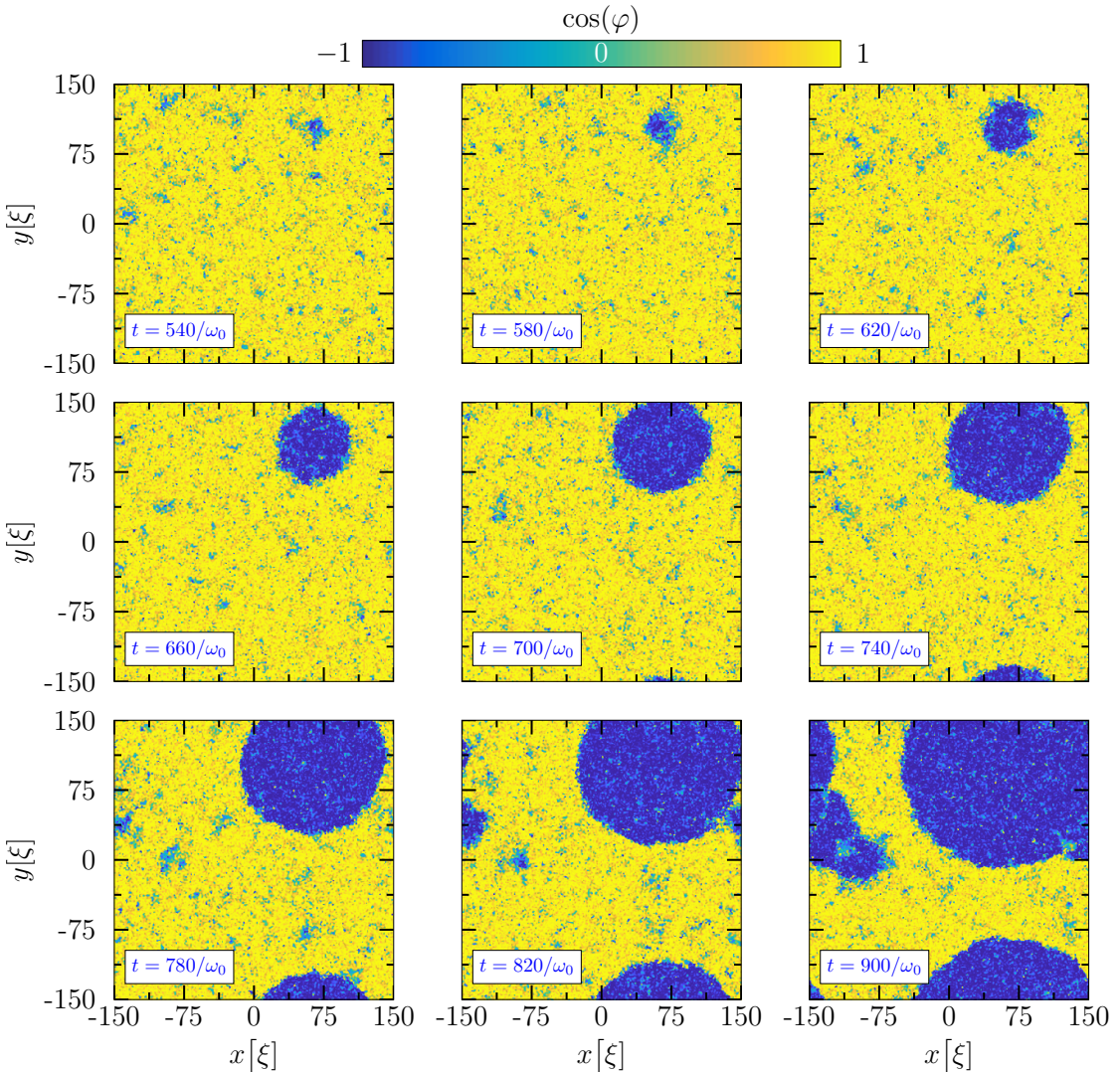


Figure 5.2: An example realisation of bubble nucleation in ${}^7\text{Li}$ with dimensionless coupling parameters $\lambda = 1.7$ and $\epsilon = 0.1$, density $\rho = 21/\xi^2$ and temperature $T = 2.4\mu/k_{\text{B}}$.

In line with Section 4.8, the survival probability $P(t)$ is given by the proportion of stochastic trajectories which satisfy $\langle \cos(\phi) \rangle > 0.5$ at any time. We slightly improve our method of obtaining the rate of false vacuum decay, Γ , from P . We continue to fit $P(t) = ae^{-\Gamma t}$, but in contrast to the procedure of earlier chapters, we restrict the fit to the region, $t_{\text{start}} \leq t \leq t_{\text{end}}$. Here, t_{start} is the first time which satisfies $P(t) \leq 0.6$ and $t_{\text{end}} = \tau_0 + 0.1(\tau_0 - t_{\text{start}})$, where τ_0 is the first time which satisfies $P(t) = 0$. This regime ensures that fit termination depends consistently on the duration of decay.

The dependence of Γ on both temperature and density is explored in Figure 5.3. In line with the instanton predictions of Section 1.2.2, we find that given a fixed temperature, the rate of vacuum decay decreases as density increases, whereas for fixed density, Γ increases

with temperature. As usual, error bars were calculated using the bootstrap procedure detailed in Section 1.7.2, but with $M = 100$ and $N = 100$. We once more find the uncertainty in decay rate to be largest for the highest values of Γ , which can be attributed to a shift from first to second order behaviour as density decreases or temperature increases.

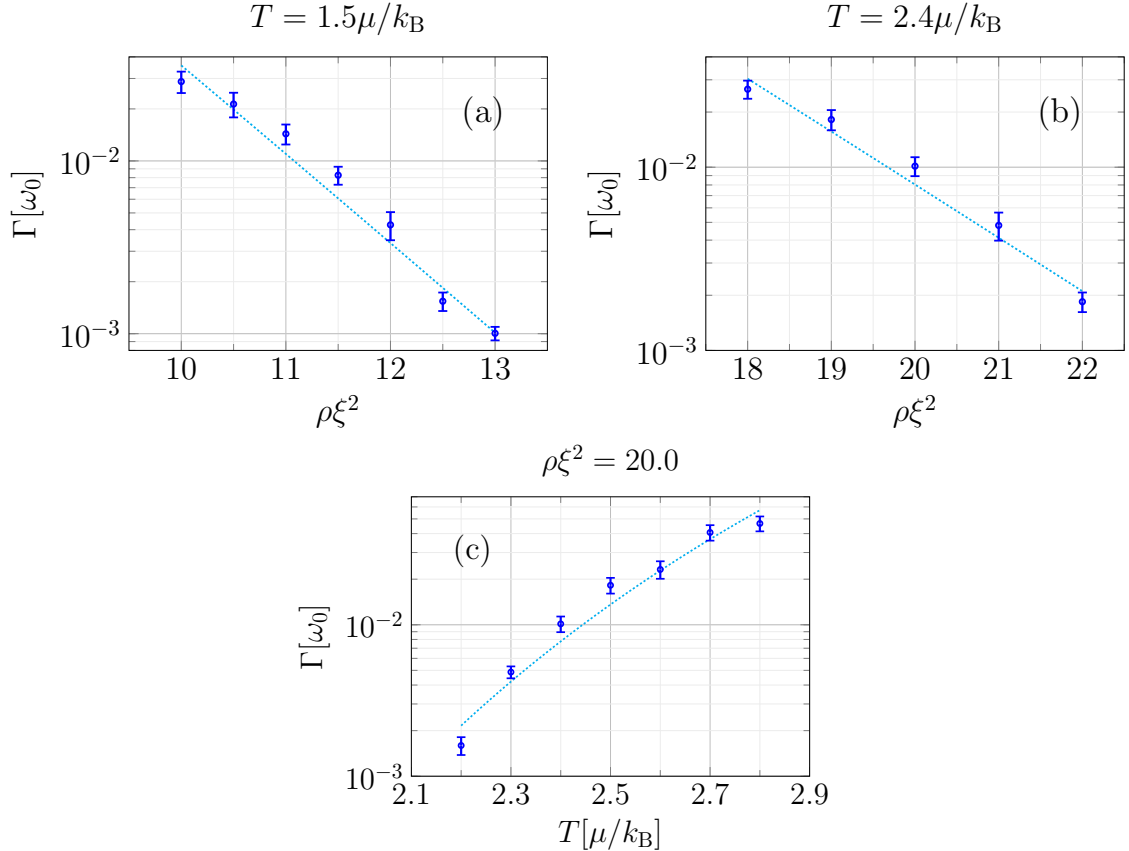


Figure 5.3: The vacuum decay rate Γ for ${}^7\text{Li}$, as a function of the density ρ (made dimensionless as $\rho\xi^2$) (a - b), and of temperature T (c). In these plots $\lambda = 1.7$ and $\epsilon = 0.1$. Each panel includes a comparison between the SPGPE results (data points) and their instanton fit (dotted line).

We once again compare our simulated results to the instanton prediction. As detailed in Section 1.2.2, for a two-dimensional thermal system, this is given by:

$$\Gamma_{\text{inst}} = AS_E[\varphi_b]e^{-S_E[\varphi_b]}. \quad (5.10)$$

Note that this is the same form as Equation (4.75). However, here:

$$S_E[\varphi] = \frac{2\rho\xi^2}{T} \int d^2x \left\{ \frac{1}{2} (\nabla_{2D}\varphi)^2 + V_{\text{eff}}(\varphi) \right\}. \quad (5.11)$$

Note the contrast with Equation (4.76); since the false vacuum decays via thermal fluctuations, S_E is time independent, as introduced in Section 1.2.1. By making transformations (4.77), the above reduces to:

$$S_E[\varphi] = \frac{\tilde{\chi}}{T} \int d^2x' \left\{ \frac{1}{2} (\nabla'_{2D} \varphi)^2 + \tilde{V}_{\text{eff}}(\varphi) \right\}, \quad (5.12)$$

where $\tilde{\chi} = 2\rho\zeta^2/(c\epsilon\lambda_c)$ and, as usual:

$$\tilde{V}_{\text{eff}}(\varphi) = \cos(\varphi) + \frac{1}{2}\lambda'^2 \sin^2(\varphi), \quad (5.13)$$

and $\lambda' = \lambda/\lambda_c$. Once again, we have reduced our system to that examined in Ref. [27]. Thus, we deduce:

$$\Gamma_{\text{inst}} = A(F\chi/T)e^{-F\chi/T}, \quad (5.14)$$

where F is once more a λ' -dependent constant. In line with Equation (4.82), we combine constants and fit:

$$\Gamma_{\text{inst}} = A'(\rho/T)e^{-B'\rho/T}, \quad (5.15)$$

to the simulated data, with freedom in A' and B' .

The instanton fits are also included in Figure 5.3. Note that in contrast to previous similar investigations, these fits are weighted by the numerical error bars. In general, we find good agreement between the SPGPE and instanton approaches.

5.5 Numerical Setup: Trapping Potential

In order to determine the experimental viability of our investigations, we examined the effects of adding a trapping potential to the system. We proceeded with a periodic setup in the numerics, but increased the width of the system from L to $L_{\text{trap}} = (3/2)L$, whilst conserving the grid spacing $\Delta l = \Delta x = \Delta y$, and introduced a square trapping potential of the form $V_{\text{trap}} = \max \{ V(x), V(y) \}$, where:

$$V(x) = \frac{1}{2} \left[2 + \tanh \left(\frac{x - l_0}{\sigma} \right) - \tanh \left(\frac{x + l_0}{\sigma} \right) \right]. \quad (5.16)$$

Here, l_0 is the trap width and σ is the trap wall thickness. Throughout this work, we fix $l_0 = (1/2)L$ and $\sigma = 3$; the former limiting the inhabitable region of the system to a box of same size as the un-trapped system. The potential V_{trap} is shown for these parameters in Figure 5.4. We also tested the impact of reducing the wall thickness to $\sigma = 1$, but this had negligible effect.

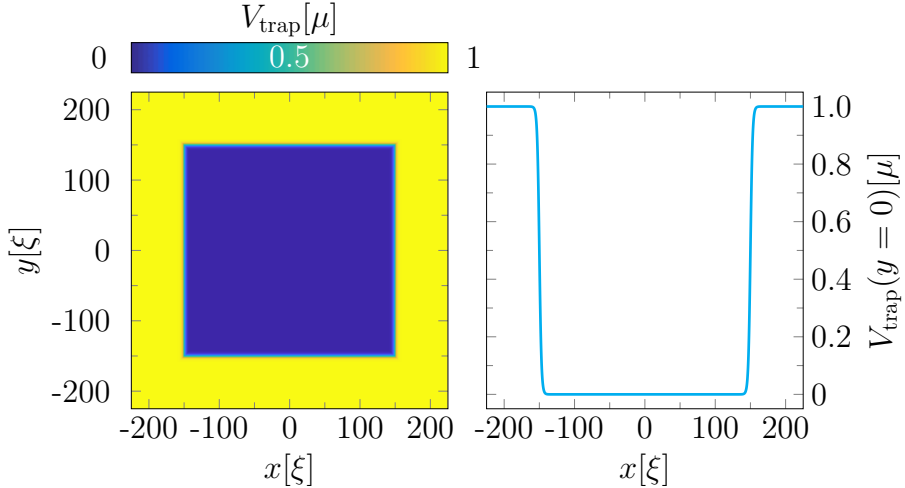


Figure 5.4: The square trapping potential $V_{\text{trap}} = \max \{V(x), V(y)\}$, where $V(x)$ is defined in Equation (5.16). Here, $l_0 = 150\xi$ and $\sigma = 3\xi$. Left: The full spatial profile of V_{trap} . Right: a slice through V_{trap} at $y = 0$.

The inclusion of a trapping potential introduces a further complication; we no longer have analytic formulae for the vacuum states and must find these numerically. We first seek the Thomas-Fermi (TF) [86] ground state corresponding to $\theta = \varphi = 0$. This is found by making the transformation $\mu \rightarrow \mu - V_{\text{trap}}$ and solving the standard Gross-Pitaevskii equation (GPE), under the assumption that the kinetic and $\mathcal{O}(\epsilon^2)$ terms can be neglected. In the parameterisation (4.39)-(4.40), the standard Thomas-Fermi approximation becomes:

$$\rho_{\text{TF}} = \begin{cases} \frac{\mu - V_{\text{trap}} - \omega_q/2}{g(1 + g'/g)} & \text{if } \mu - V_{\text{trap}} - \omega_q/2 > 0, \\ 0 & \text{otherwise,} \end{cases} \quad (5.17)$$

where ω_q is the quadratic Zeeman shift introduced in Section 1.5.6. We then proceed by propagating the Thomas-Fermi solution in real time, using a damped GPE:

$$i \frac{\partial \psi_m}{\partial t} = (1 - i) \left[-\frac{1}{2} \nabla^2 \psi_m + \frac{\partial V}{\partial \psi_m^\dagger} \right], \quad (5.18)$$

where the chemical potential and trapping potential are included in V . The simulation is run for sufficient time to allow the wavefunction to converge to a stable vacuum state, as shown in Figure 5.5, which is then input as the initial conditions of the usual SPGPE procedure.

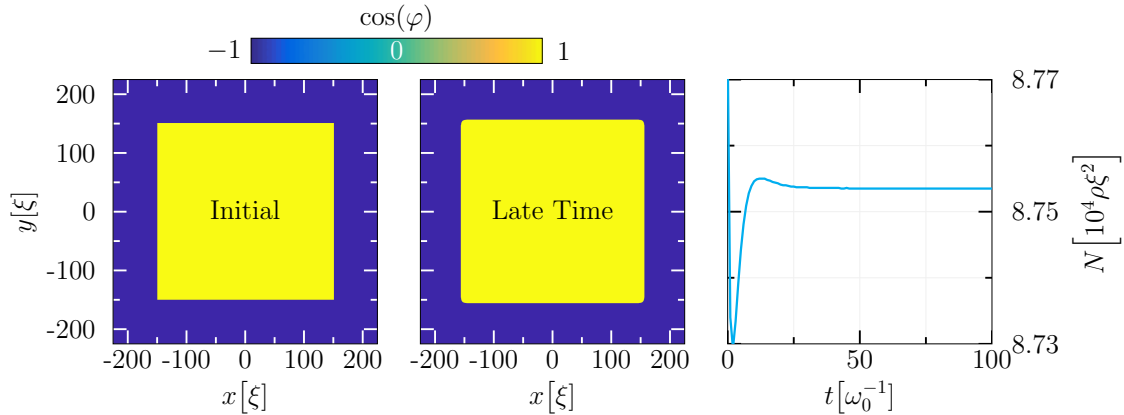


Figure 5.5: The result of propagating the Thomas Fermi solution (5.17) in real time using the damped GPE (5.18). Left: The spatial profile of $\cos(\varphi)$ prior to this evolution. Centre: The resultant profile of $\cos(\varphi)$. The profile rounds about the corners of the inhabitable region. Right: The evolution of the total particle number, N . Here, N converges to a constant value, corresponding to the area of the inhabitable region.

5.6 Numerical Results: Trapping Potential

The behaviour of $\cos(\varphi)$ in the presence of V_{trap} is explored in Figure 5.6. The addition of boundaries accelerates the bubble nucleation process; the trap walls themselves act as nucleation sites. In general, bubbles form along these first, before expanding to enclose and ultimately fill the inhabitable region. Bubbles rarely have time to form away from the walls, and any such bubbles are eventually consumed by their older neighbours. An example of this is included in Figure 5.6. In order to increase the yield of central bubbles, and prolong their existence, we suggest increasing the system size substantially. Due to computational cost, we refrained from doing this.

The effect of boundaries is made more explicit in Figure 5.7, where the rate of false vacuum decay is plotted as a function of density for both the trapped and un-trapped systems. Whilst Γ continues to decay with density in the presence of V_{trap} , the inclusion of an external trapping potential induces a global increase in the rate of vacuum decay.

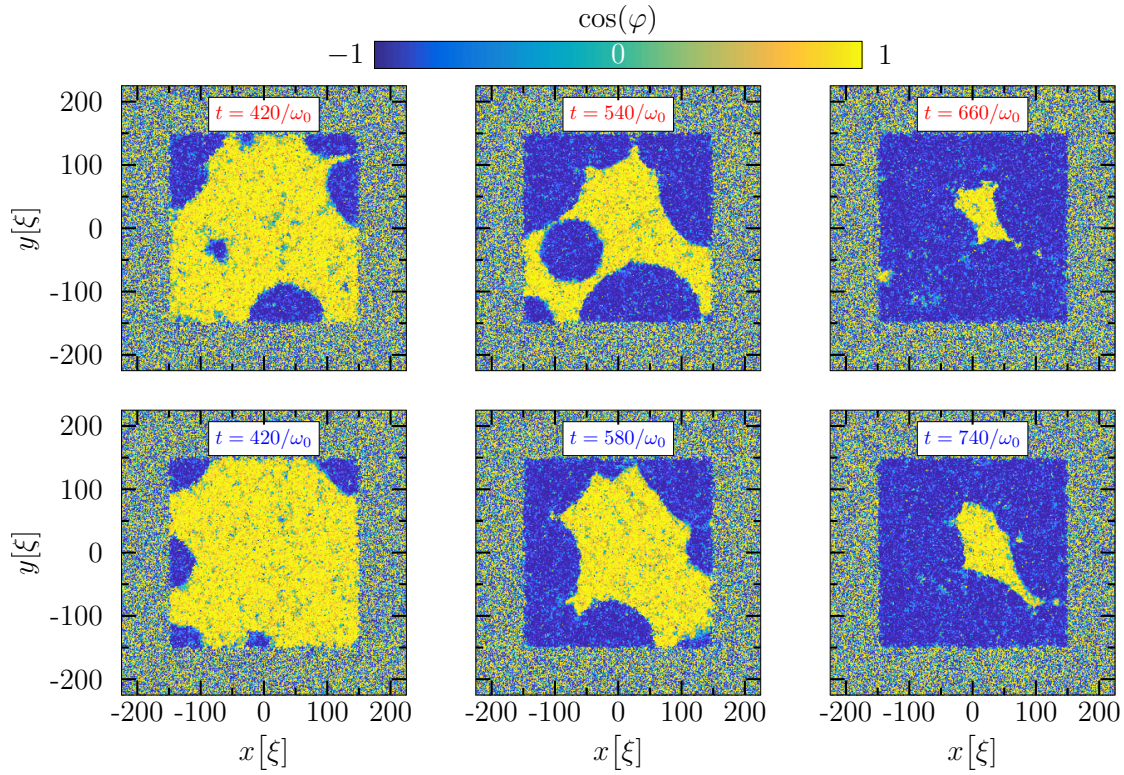


Figure 5.6: The varying behaviour of example $\cos(\varphi)$ realisations in the presence of a square external potential, V_{trap} . Parameters are the same as in Figure 5.2, but with density $\rho = 20/\xi^2$. In all observed realisations, bubbles first nucleate around the trap boundaries. Top row (rare): A bubble nucleates away from the wall, which is eventually engulfed by the boundary bubbles. Bottom row (common): Boundary bubbles expand and fill the trap before a central bubble can form.

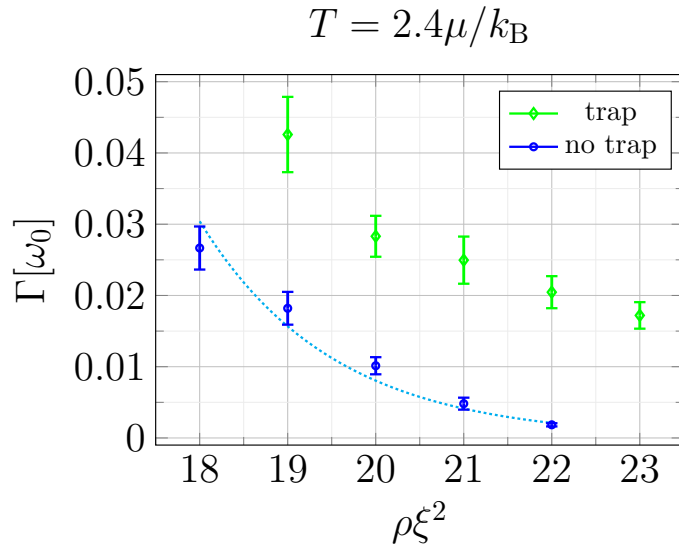


Figure 5.7: A comparison of the vacuum decay rate Γ in the presence (green diamond) and absence (blue circle) of V_{trap} . Here, Γ is plotted as a function of the density ρ (made dimensionless as $\rho\xi^2$), for $\lambda = 1.7$ and $\epsilon = 0.1$. The instanton fit (dotted line) is included alongside the simulated data for the trap-less case.

5.7 Experimental Realisation

Here, many experimental details remain as described in Section 4.9; the relevant physical properties of the alkali species considered in this chapter can be found in Table 4.1, and whilst g'/g is fixed by the atomic species, there continues to be considerable flexibility in the choice of tuneable experimental parameters that correspond to the dimensionless parameters used in our simulations.

As an example, a system with parameters similar to those used in Figure 5.3, but with a larger density $\rho = 50/\xi^2$, would correspond to around 50,000 ${}^7\text{Li}$ atoms in a 100 μm wide square optical trap, with transverse frequency $\omega_r = 2\pi \times 50 \text{ kHz}$, a bias field of $B_z = 0.27 \text{ Gauss}$, and timescale ω_0^{-1} corresponding to 1.1 ms. Such a system would have a smaller extent (32ξ) than our simulations when measured in healing lengths, and the temperature unit $\mu/k_B \approx 7 \text{ nK}$ would be small in comparison to $\hbar\omega_\perp/(2k_B)$. An alternative scheme with potassium would correspond to around $1.9 \times 10^6 {}^{41}\text{K}$ atoms in a 170 μm wide square trap, with transverse frequency $\omega_r = 2\pi \times 1.9 \text{ kHz}$ and a bias field of $B_z = 0.08 \text{ Gauss}$. Such a system would have timescale $\omega_0^{-1} = 0.2 \text{ ms}$, density $\rho = 21/\xi^2$, and an extent of 300ξ similar to our simulations. The energy scales would satisfy $\mu \lesssim \hbar\omega_\perp/2 \lesssim k_B T$ when the temperature is a few times the temperature unit $\mu/k_B \approx 37 \text{ nK}$.

Again, in any experiment, we assume there to be substantial experimental flexibility in the coupling field Rabi frequencies and detuning (Ω , Ω_{\pm} , Δ_e). In practice, additional smaller light shifts must be considered in order to achieve the desired ϵ and λ values.

Finally, we note that whilst the three-component system of this thesis utilises radio-frequency mixing to couple level $|0\rangle$ to $|+1\rangle$ and level $| -1\rangle$ to $|0\rangle$, our proposal should work equally well if these levels were instead coupled by Raman transitions.

5.8 Conclusion

In this chapter, we extended our investigations of a spin-1 Bose gas to a two-dimensional system at finite temperature. Following Chapters 2-4, we initially examined a periodic system, first locating a parameter space in which bubble nucleation could be observed for ^7Li atoms, before going on to examine the relationship between the rate of false vacuum decay, temperature and density for this species. We compared our numerical results to instanton predictions and found good agreement. We then added a trapping potential to the system, in order to determine the effect of boundaries on bubble growth. We found boundaries to seed nucleation, resulting in an overall increase in the rate of vacuum decay. Whilst boundaries largely inhibited the clean nucleation events observed in their absence, we are confident that their disruption can be minimised by increasing the system size. This observation also adds strength to the suspicion that bubbles may themselves act as nucleation sites for other bubbles; an avenue we hope to explore in the near future.

Chapter 6

Conclusions and Future Work

Here, we summarize the key findings of this thesis, and suggest possible avenues for future work.

6.1 Conclusions

We comment on each chapter in turn, before drawing some general conclusions.

6.1.1 Chapter 2

The investigations of this thesis began in Chapter 2. Here, we built on previous efforts to model false vacuum decay in a one-dimensional, two-component, Bose gas, by incorporating finite temperature effects. In this chapter, we approximated the experimental interaction potential with the well established stationary potential of Fialko *et al.* [39, 41]. The main purpose of this chapter was to demonstrate the effectiveness of the SPGPE. Thus, we first examined correlations about the true vacuum state at a range of temperatures and found the correlation function to agree qualitatively with the analytic Klein-Gordon formula. Full agreement was found once we accounted for the renormalization of the interaction potential. We then proceeded to investigate bubble nucleation in this system, first examining the qualitative behaviour of individual nucleation events, before going on to determine the dependence of the decay rate on temperature and potential geometry. We found the simulated rates of false vacuum decay to align with instanton predictions, increasing with temperature but decreasing with barrier height.

6.1.2 Chapter 3

The motivation for incorporating thermal effects in the first place was to investigate whether or not they could be used to overcome the parametric instability that emerges when the full time-dependent interaction potential is implemented. Thus, in Chapter 3, we replaced the static interaction potential of Chapter 2 with its oscillatory counterpart. We first carried out a theoretical investigation to identify the dependence of the location and size of the resonance band on the driving frequency of the potential and on the damping parameter γ . Having predicted the values of γ required to erase the instability, we went on to verify this numerically. We used SPGPE simulations to examine the relationship between the rate of false vacuum decay and the damping parameter at a range of temperatures and driving frequencies and compared our findings with the stationary-potential results. At low γ values, we found decay rates to significantly exceed stationary-potential values, indicating the presence of a parametric instability. However, as we increased γ , we found the decay rate to converge to the stationary-potential value as a result of the instability being erased. The higher the driving frequency, the lower the value of γ at which agreement was reached. However, the γ values shown to damp out the instability were higher than any predicted or experimentally-measured value. This brought into question the viability of the two-component system altogether.

6.1.3 Chapter 4

With this in mind, we turned to an alternative system, free from instabilities; a one-dimensional, three-component Bose gas at zero temperature. We spent the first half of Chapter 4 examining the complex phase structure of this more complicated system and searching its vast parameter space for vacua. We used the PGPE under the truncated Wigner approximation to simulate bubble nucleation in this system. In particular, we examined the relationship between the rate of false vacuum decay and density, and found this rate to decrease as density increases. We compared our simulated data curves to instanton predictions and found good agreement. We also briefly investigated the dependence of the decay rate on barrier height and, in line with Chapter 2, found the rate of false vacuum decay to decrease as the potential barrier height is raised. This initial investigation showed the spin-1 system to be a worthy contender for future analogue experiments.

6.1.4 Chapter 5

In Chapter 5, we improved the applicability of our three-component considerations to the early universe, by upgrading to a two-dimensional system at finite temperature. Consequently, we returned to the SPGPE. We first investigated vacuum decay in a periodic

system, beginning with a qualitative examination of bubble nucleation, which revealed the growth of neat, circularly-symmetric bubbles. We went on to explore the relationship between decay rate, density, and temperature, finding the rate of false vacuum decay to decrease with density but increase with temperature, following instanton predictions. With future experiments in mind, we went on to incorporate a trapping potential into the system. We found this to accelerate the vacuum decay process, as a result of bubbles nucleating preferentially along the trap walls. This was problematic, since boundary effects are not authentic to the early universe. However, we concluded that this effect could be negated by increasing the size of our analogue system.

6.1.5 General Conclusions

In this thesis, we evaluated the merits and drawbacks of a range of cold atom analogue systems. We successfully simulated relativistic false vacuum decay in each and determined the dependence of decay rate on key parameters, filling vital gaps in the wider understanding of such systems. Whilst setbacks may arise along the way, we remain confident that with the aid of future theoretical investigations, cold-atom laboratories will soon provide an invaluable window into the first-order phase transitions of the early universe.

6.2 Future Work

6.2.1 Pseudo-Spin-1/2 System

The most pressing issue with the two-component system is the presence of a parametric instability, which may or may not be overcome by thermal effects. Whilst in Chapter 3, the values of the damping parameter γ needed to suppress the instability were deemed unrealistically high, it is possible that we did not capture the full picture. When using the simple growth SPGPE, we make a number of assumptions; we assume the damping parameter to be constant, we assume a static thermal cloud, and we neglect additional scattering terms present in the full SPGPE theory [88]. Lifting any of these assumptions could have a notable effect on bubble dynamics. Thus, it would be worthwhile to explore each further. In particular, a dynamic thermal cloud could be modelled using a quantum Boltzmann equation, following the ZNG approach [120, 81]. Accounting for thermal cloud dynamics would permit us to raise the modulation frequency of the interaction potential, which in itself is likely lessen the instability.

6.2.2 Spin-1 System

The very same adjustments would also be worth investigating in the three-component system. However, the precise value of the damping parameter is less important in this system. Instead, here, we are concerned with boundary effects. We found the inclusion of a trapping potential to disrupt our investigations, since boundaries seeded bubbles at locations uncharacteristic of the early universe. We predict that this issue can be overcome by increasing the system size to such an extent that boundary effects can be isolated from some specified central region of the system for long enough to allow so-called central bubbles to nucleate undisturbed. It would therefore be useful to carry out this investigation and calculate the rate of false vacuum decay in the central region only.

6.2.3 General Ideas

Some more natural extensions of our work arise, common to both systems. In order to draw a closer analogy with the early universe, it would be beneficial to extend each system to three spatial dimensions. It could also be useful to investigate a larger range of isotopes, in order to give experimentalists more freedom. Furthermore, the analyses of this thesis primarily focus on the rate of false vacuum decay. It would be interesting to go beyond this and, for example, look more closely at bubble collision events and the correlation between bubble nucleation sites.

Appendix A

A.1 Reducing the Dimensions of the GPE

The 3D Gross-Pitaevskii Equation (GPE) is given by:

$$i\hbar \frac{\partial \Psi}{\partial t} = -\frac{\hbar^2}{2m} \nabla^2 \Psi + V\Psi + g|\Psi|^2\Psi - \mu\Psi, \quad (\text{A.1})$$

where $\Psi = \Psi(x, y, z, t)$ and $V = \frac{1}{2}m(\omega_x^2x^2 + \omega_y^2y^2 + \omega_z^2z^2)$ for a harmonically-trapped condensate.

A.1.1 1D condensate

Provided that $\omega_x, \omega_y \gg \omega_z$ and $\hbar(\omega_x\omega_y)^{1/2} \gg \mu$, our condensate assumes an effectively 1D cigar shape, tightly aligned in the z direction. Consequently, the x and y dependence of Ψ is determined solely by the respective harmonic oscillator ground states. We make the ansatz:

$$\Psi(x, y, z, t) = \psi_z(z, t)G_x(x)G_y(y), \quad (\text{A.2})$$

where,

$$G_{x_j}(x_j) = \frac{1}{(\pi\ell_{x_j}^2)^{1/4}} e^{-x_j^2/2\ell_{x_j}^2}, \quad x_j = x, y, z, \quad (\text{A.3})$$

are the ground states and $\ell_{x_j} = \sqrt{\frac{\hbar}{m\omega_{x_j}}}$ are the corresponding harmonic oscillator lengths.

The prefactors in equation (A.2) ensure that the ground states are normalised to unity:

$$\int_{-\infty}^{\infty} |G_{x_j}|^2 dx_j = \int_{-\infty}^{\infty} G_{x_j}^2 dx_j = 1. \quad (\text{A.4})$$

Now, substituting ansatz (A.2) into Equation (A.1) yields:

$$\begin{aligned} i\hbar G_x G_y \frac{\partial \psi_z}{\partial t} = & -\frac{\hbar^2}{2m} \left[\left(\frac{x^2}{\ell_x^4} - \frac{1}{\ell_x^2} + \frac{y^2}{\ell_y^4} - \frac{1}{\ell_y^2} \right) G_x G_y \psi_z + G_x G_y \frac{\partial^2 \psi_z}{\partial z^2} \right] \\ & + \frac{1}{2} m \left(\omega_x^2 x^2 + \omega_y^2 y^2 + \omega_z^2 z^2 \right) G_x G_y \psi_z + g G_x G_y \psi_z |G_x|^2 |G_y|^2 |\psi_z|^2 \\ & - \mu G_x G_y \psi_z. \end{aligned} \quad (\text{A.5})$$

Multiplying by $G_x^* G_y^*$ and integrating with respect to x and y reduces this to:

$$i\hbar \frac{\partial \psi_z}{\partial t} = -\frac{\hbar^2}{2m} \frac{\partial^2 \psi_z}{\partial z^2} + \frac{1}{2} m \omega_z^2 z^2 \psi_z - \mu \psi_z + F(x, y), \quad (\text{A.6})$$

where,

$$F(x, y) = \frac{\hbar^2}{2m} \left(\frac{1}{\ell_x^2} + \frac{1}{\ell_y^2} \right) \psi_z + \frac{g}{2\pi\ell_x\ell_y} |\psi_z|^2 \psi_z. \quad (\text{A.7})$$

We may then reformulate Equation (A.6) as follows:

$$i\hbar \frac{\partial \psi_z}{\partial t} = -\frac{\hbar^2}{2m} \frac{\partial^2 \psi_z}{\partial z^2} + V_z \psi_z - \mu_{1D} \psi_z + g_{1D} |\psi_z|^2 \psi_z, \quad (\text{A.8})$$

where,

$$V_z = \frac{1}{2} m \omega_z^2 z^2, \quad (\text{A.9})$$

$$\mu_{1D} = \mu - \frac{\hbar^2}{2m} \left(\frac{1}{\ell_x^2} + \frac{1}{\ell_y^2} \right) \equiv \mu - \frac{\hbar}{2} (\omega_x + \omega_y), \quad (\text{A.10})$$

$$g_{1D} = \frac{g}{2\pi\ell_x\ell_y}. \quad (\text{A.11})$$

In the special case where $\ell_x = \ell_y = \ell_\perp$, μ_{1D} and g_{1D} simplify to:

$$\mu_{1D} = \mu - \hbar \omega_\perp, \quad \text{where } \omega_\perp = \frac{\hbar}{m\ell_\perp^2}, \quad (\text{A.12})$$

$$g_{1D} = \frac{g}{2\pi\ell_\perp^2}. \quad (\text{A.13})$$

In this case, substituting in $\ell_\perp = \sqrt{\frac{\hbar}{m\omega_\perp}}$ and $g = \frac{4\pi\hbar^2 a_s}{m}$ gives:

$$g_{1D} = \frac{1}{2\pi} \left(\frac{4\pi\hbar^2 a_s}{m} \right) \frac{m\omega_\perp}{\hbar} = 2\hbar a_s \omega_\perp. \quad (\text{A.14})$$

A.1.2 2D condensate

Provided that $\omega_x, \omega_y \ll \omega_z$ and $\hbar\omega_z \gg \mu$, our harmonically trapped condensate assumes an effectively 2D pancake shape. Consequently, the z dependence of Ψ is determined solely by the corresponding harmonic oscillator ground state. We make the ansatz:

$$\Psi(x, y, z, t) = \psi_{\perp}(x, y, t)G_z(z), \quad (\text{A.15})$$

where $G_z(z)$ is as defined in Equation (A.3).

Following the 1D calculation, substituting ansatz (A.15) into Equation (A.1) yields:

$$\begin{aligned} i\hbar G_z \frac{\partial \psi_{\perp}}{\partial t} &= -\frac{\hbar^2}{2m} \left[\frac{\partial^2 \psi_{\perp}}{\partial x^2} G_z + \frac{\partial^2 \psi_{\perp}}{\partial y^2} G_z + \left(\frac{z^2}{\ell_z^4} - \frac{1}{\ell_z^2} \right) \psi_{\perp} G_z \right] \\ &\quad + \frac{1}{2} m \left(\omega_x^2 x^2 + \omega_y^2 y^2 + \omega_z^2 z^2 \right) \psi_{\perp} G_z \\ &\quad + g |\psi_{\perp}|^2 |G_z|^2 \psi_{\perp} G_z - \mu \psi_{\perp} G_z. \end{aligned} \quad (\text{A.16})$$

Multiplying by G_z^* and then integrating with respect to z reduces this to:

$$i\hbar \frac{\partial \psi_{\perp}}{\partial t} = -\frac{\hbar^2}{2m} \nabla_{2D}^2 \psi_{\perp} + \frac{1}{2} m \left(\omega_x^2 x^2 + \omega_y^2 y^2 \right) \psi_{\perp} - \mu \psi_{\perp} + H(z), \quad (\text{A.17})$$

where,

$$H(z) = \frac{\hbar^2}{2m} \frac{1}{\ell_z^2} \psi_{\perp} + \frac{g}{\sqrt{2\pi}\ell_z} |\psi_{\perp}|^2 \psi_{\perp}. \quad (\text{A.18})$$

We may then reformulate Equation (A.17) as follows:

$$i\hbar \frac{\partial \psi_{\perp}}{\partial t} = -\frac{\hbar^2}{2m} \nabla_{2D}^2 \psi_{\perp} + V_{\perp} \psi_{\perp} - \mu_{2D} \psi_{\perp} + g_{2D} |\psi_{\perp}|^2 \psi_{\perp}, \quad (\text{A.19})$$

where,

$$V_{\perp} = \frac{1}{2} m \left(\omega_x^2 x^2 + \omega_y^2 y^2 \right), \quad (\text{A.20})$$

$$\mu_{2D} = \mu - \frac{\hbar^2}{2m} \frac{1}{\ell_z^2} \equiv \mu - \frac{\hbar}{2} \omega_z, \quad (\text{A.21})$$

$$g_{2D} = \frac{g}{\sqrt{2\pi}\ell_z}. \quad (\text{A.22})$$

Substituting in $\ell_z = \sqrt{\frac{\hbar}{m\omega_z}}$ and $g = \frac{4\pi\hbar^2 a_s}{m}$ gives:

$$g_{2D} = \frac{1}{\sqrt{2\pi}} \left(\frac{4\pi\hbar^2 a_s}{m} \right) \sqrt{\frac{m\omega_z}{\hbar}} = \left(\frac{8\pi\hbar^3 \omega_z}{m} \right)^{1/2} a_s. \quad (\text{A.23})$$

Appendix B

B.1 Reformulating the two-component potential in terms of relative phase

The stationary interaction potential of the two-component system investigated in Chapter 2 is given by:

$$V_{\text{stat}} = \frac{g}{2} \sum_{j=1,2} (\psi_j^\dagger \psi_j)^2 - \mu \psi^\dagger \psi - \mu \epsilon^2 \psi^\dagger \sigma_x \psi + \frac{g}{4} \epsilon^2 \lambda^2 (\psi^\dagger \sigma_y \psi)^2, \quad (\text{B.1})$$

$$\begin{aligned} &= \frac{g}{2} \left[(\psi_1^\dagger \psi_1)^2 + (\psi_2^\dagger \psi_2)^2 \right] - \mu (\psi_1^\dagger \psi_1 + \psi_2^\dagger \psi_2) - \mu \epsilon^2 (\psi_1^\dagger \psi_2 + \psi_2^\dagger \psi_1) \\ &\quad - \frac{g}{4} \epsilon^2 \lambda^2 (\psi_2^\dagger \psi_1 - \psi_1^\dagger \psi_2)^2. \end{aligned} \quad (\text{B.2})$$

We make the Madelung transformation:

$$\psi_1 \approx \sqrt{n_1} e^{i\theta_1}, \quad \psi_2 \approx \sqrt{n_2} e^{i\theta_2}. \quad (\text{B.3})$$

Substituting the above into Equation (B.2) yields:

$$\begin{aligned} V_{\text{stat}} &= \frac{g}{2} (n_1^2 + n_2^2) - \mu(n_1 + n_2) - \mu \epsilon^2 \left[\sqrt{n_1 n_2} \left(e^{i(\theta_2 - \theta_1)} + e^{i(\theta_1 - \theta_2)} \right) \right] \\ &\quad - \frac{g}{4} \epsilon^2 \lambda^2 \left[\sqrt{n_1 n_2} \left(e^{i(\theta_1 - \theta_2)} - e^{i(\theta_2 - \theta_1)} \right) \right]^2. \end{aligned} \quad (\text{B.4})$$

By assuming approximately equal component densities, $n_1 \approx n_2 = n$ and introducing the phase difference between components, $\varphi = \theta_1 - \theta_2$, we find:

$$V_{\text{stat}} \approx gn^2 - 2\mu n - \mu \epsilon^2 n (e^{i\varphi} + e^{-i\varphi}) - \frac{g}{4} \epsilon^2 \lambda^2 n^2 (e^{i\varphi} - e^{-i\varphi})^2, \quad (\text{B.5})$$

$$= gn^2 - 2\mu n - 2\mu \epsilon^2 n \cos(\varphi) + g \epsilon^2 \lambda^2 n^2 \sin^2(\varphi). \quad (\text{B.6})$$

In the last step, we made use of the identities $\sin(x) = \frac{1}{2i}(e^{ix} - e^{-ix})$ and $\cos(x) = \frac{1}{2}(e^{ix} + e^{-ix})$. Finally, by assuming $n \approx \rho_0$, where $\rho_0 = \mu/g$ is the mean condensate density, we arrive at:

$$V_{\text{stat}}(\varphi) \approx \frac{\mu^2}{g} \left[-1 - 2\epsilon^2 \cos(\varphi) + \epsilon^2 \lambda^2 \sin^2(\varphi) \right]. \quad (\text{B.7})$$

B.2 Making the 1D SGPE Dimensionless

We begin with the one-dimensional (1D) stochastic Gross-Pitaevskii equation (SGPE):

$$i\hbar \frac{\partial \psi}{\partial t} = (1 - i\gamma) \left[-\frac{\hbar^2}{2m} \frac{\partial^2 \psi}{\partial x^2} + \frac{\partial V(\psi)}{\partial \psi^*} \right] + \eta(x, t), \quad (\text{B.8})$$

where $\langle \eta^*(x, t)\eta(x', t') \rangle = 2\gamma\hbar k_B T \delta(x - x')\delta(t - t')$. We express each variable featured above in terms of a characteristic quantity and a corresponding dimensionless variable, distinguished by a hat:

$$x = \xi \hat{x}, \quad t = \omega_0^{-1} \hat{t}, \quad \psi = \rho_0^{1/2} \hat{\psi}. \quad (\text{B.9})$$

Here, $\xi = \hbar/(mg\rho_0)^{1/2}$ is the healing length of the system, $\omega_0 = c/\xi$ is a characteristic frequency, dependent on the speed of sound $c = \hbar/(m\xi)$, and $\rho_0 = \mu/g$ is the mean particle density. Substituting these transformations into Equation (B.8) yields:

$$ig\rho_0^{3/2} \frac{\partial \hat{\psi}}{\partial \hat{t}} = (1 - i\gamma) \left[-\frac{1}{2} g \rho_0^{3/2} \frac{\partial^2 \hat{\psi}}{\partial \hat{x}^2} + \rho_0^{-1/2} \frac{\partial V(\hat{\psi})}{\partial \hat{\psi}^*} \right] + \eta(\hat{x}, \hat{t}), \quad (\text{B.10})$$

$$\Rightarrow i \frac{\partial \hat{\psi}}{\partial \hat{t}} = (1 - i\gamma) \left[-\frac{1}{2} \frac{\partial^2 \hat{\psi}}{\partial \hat{x}^2} + g^{-1} \rho_0^{-2} \frac{\partial V(\hat{\psi})}{\partial \hat{\psi}^*} \right] + g^{-1} \rho_0^{-3/2} \eta(\hat{x}, \hat{t}). \quad (\text{B.11})$$

Natural rescalings of both V and η emerge from the above:

$$V = g\rho_0^2 \hat{V} = \hbar\omega_0 \rho_0 \hat{V}, \quad \eta = g\rho_0^{3/2} \hat{\eta} = \hbar\omega_0 \rho_0^{1/2} \hat{\eta}. \quad (\text{B.12})$$

Then, we arrive at:

$$i \frac{\partial \hat{\psi}}{\partial \hat{t}} = (1 - i\gamma) \left[-\frac{1}{2} \frac{\partial^2 \hat{\psi}}{\partial \hat{x}^2} + \frac{\partial \hat{V}(\hat{\psi})}{\partial \hat{\psi}^*} \right] + \hat{\eta}(\hat{x}, \hat{t}). \quad (\text{B.13})$$

Finally, we introduce a rescaled temperature, \hat{T} , defined such that:

$$\langle \hat{\eta}^*(\hat{x}, \hat{t}) \hat{\eta}(\hat{x}', \hat{t}') \rangle = 2\gamma \hat{T} \delta(\hat{x} - \hat{x}') \delta(\hat{t} - \hat{t}'). \quad (\text{B.14})$$

We calculate $\langle \hat{\eta}^*(\hat{x}, \hat{t}) \hat{\eta}(\hat{x}', \hat{t}') \rangle$ as follows:

$$\langle \hat{\eta}^*(\hat{x}, \hat{t}) \hat{\eta}(\hat{x}', \hat{t}') \rangle = \hbar^{-2} \omega_0^{-2} \rho_0^{-1} \langle \eta^*(x, t) \eta(x', t') \rangle, \quad (\text{B.15})$$

$$= (\hbar^{-1} \omega_0^{-1} \rho_0^{-1} \xi^{-1} k_B) (2\gamma T \delta(\hat{x} - \hat{x}') \delta(\hat{t} - \hat{t}')). \quad (\text{B.16})$$

If we let $T = T_{\text{CO}} \hat{T}$, where $T_{\text{CO}} = \hbar \omega_0 \rho_0 \xi / k_B = \hbar c \rho_0 / k_B$, then Equation (B.14) follows. It turns out that T_{CO} is actually the cross-over temperature, the temperature below which a phase-fluctuating quasi-condensate forms [73], as introduced in Section 1.4.4. Note that T_{CO} is sometimes defined with an additional factor of 2.

B.3 Klein-Gordon Reduction of the SGPE

The dimensionless Stochastic Gross-Pitaevskii Equation (SGPE) for the spin-1/2 system with stationary potential reads:

$$i \frac{\partial \psi_j}{\partial t} = (1 - i\gamma) \left[-\frac{1}{2} \nabla^2 \psi_j + \frac{\partial \hat{V}_{\text{stat}}}{\partial \psi_j^\dagger} \right] + \eta_j, \quad j = 1, 2, \quad (\text{B.17})$$

where,

$$\hat{V}_{\text{stat}} = \frac{1}{2} \sum_{j=1,2} (\psi_j^\dagger \psi_j)^2 - \psi^\dagger \psi - \epsilon^2 \psi^\dagger \sigma_x \psi + \frac{1}{4} \lambda^2 \epsilon^2 (\psi^\dagger \sigma_y \psi)^2, \quad (\text{B.18})$$

$$= \frac{1}{2} (\psi_1^\dagger \psi_1)^2 + \frac{1}{2} (\psi_2^\dagger \psi_2)^2 - \psi_1^\dagger \psi_1 - \psi_2^\dagger \psi_2 - \epsilon^2 \psi_1^\dagger \psi_2 - \epsilon^2 \psi_2^\dagger \psi_1 - \frac{1}{4} \lambda^2 \epsilon^2 (\psi_2^\dagger \psi_1 - \psi_1^\dagger \psi_2)^2. \quad (\text{B.19})$$

When considering fluctuations about the true vacuum state, $\varphi = 0$, we make the ansatz:

$$\psi_1 = e^{\chi/2} e^{\sigma/2} e^{i\varphi/2} e^{i\theta/2}, \quad (\text{B.20})$$

$$\psi_2 = e^{\chi/2} e^{-\sigma/2} e^{-i\varphi/2} e^{i\theta/2}, \quad (\text{B.21})$$

where,

- χ represents fluctuations in global density,
- σ represents fluctuations in relative density,
- φ represents fluctuations in relative phase,
- θ represents fluctuations in global phase.

We work in the long wavelength limit, for which $\nabla = \mathcal{O}(\epsilon)$, and make the additional assumptions that $\chi = \mathcal{O}(\epsilon)$, $\sigma = \mathcal{O}(\epsilon)$ and $\gamma = \mathcal{O}(\epsilon)$. For clarity, we consider each term of Equation (B.17) individually. We consider only the $j = 1$ component initially.

LHS

Here we substitute equations (B.18)-(B.19) into the left hand side (LHS) of Equation (B.17). We find:

$$i\frac{\partial\psi_1}{\partial t} = \frac{1}{2}\psi_1\left\{i\left(\dot{\chi} + \dot{\sigma}\right) - \left(\dot{\varphi} + \dot{\theta}\right)\right\}. \quad (\text{B.22})$$

RHS - Kinetic Term

Analogously to the above:

$$\frac{\partial\psi_1}{\partial x} = \frac{1}{2}\psi_1\frac{\partial}{\partial x}\left\{(\chi + \sigma) + i(\varphi + \theta)\right\}, \quad (\text{B.23})$$

$$\Rightarrow \frac{\partial^2\psi_1}{\partial x^2} = \frac{1}{2}\psi_1\frac{\partial^2}{\partial x^2}\left\{(\chi + \sigma) + i(\varphi + \theta)\right\} + \frac{1}{4}\psi_1\left(\frac{\partial}{\partial x}\left\{(\chi + \sigma) + i(\varphi + \theta)\right\}\right)^2. \quad (\text{B.24})$$

Then, by symmetry:

$$\nabla^2\psi_1 = \frac{1}{2}\psi_1\nabla^2\left\{(\chi + \sigma) + i(\varphi + \theta)\right\} + \frac{1}{4}\psi_1\left(\nabla\left\{(\chi + \sigma) + i(\varphi + \theta)\right\}\right)^2. \quad (\text{B.25})$$

Neglecting lowest order terms yields:

$$\nabla^2\psi_1 \approx \frac{i}{2}\psi_1\nabla^2(\varphi + \theta) - \frac{1}{4}\psi_1\left(\nabla(\varphi + \theta)\right)^2. \quad (\text{B.26})$$

RHS - Interaction Term

We may expand the interaction in terms of $(\chi, \sigma, \varphi, \theta)$ as follows:

$$\frac{\partial\hat{V}_{\text{stat}}}{\partial\psi_1^\dagger} = \frac{\partial\hat{V}_{\text{stat}}}{\partial\chi}\frac{\partial\chi}{\partial\psi_1^\dagger} + \frac{\partial\hat{V}_{\text{stat}}}{\partial\sigma}\frac{\partial\sigma}{\partial\psi_1^\dagger} + \frac{\partial\hat{V}_{\text{stat}}}{\partial\varphi}\frac{\partial\varphi}{\partial\psi_1^\dagger} + \frac{\partial\hat{V}_{\text{stat}}}{\partial\theta}\frac{\partial\theta}{\partial\psi_1^\dagger}. \quad (\text{B.27})$$

Now,

$$\chi = \frac{1}{2} \ln \left\{ \psi_1^\dagger \psi_1 \right\} + \frac{1}{2} \ln \left\{ \psi_2^\dagger \psi_2 \right\}, \quad (\text{B.28})$$

$$\sigma = \frac{1}{2} \ln \left\{ \psi_1^\dagger \psi_1 \right\} - \frac{1}{2} \ln \left\{ \psi_2^\dagger \psi_2 \right\}, \quad (\text{B.29})$$

$$\varphi = \frac{i}{2} \ln \left\{ \psi_1^\dagger \psi_2 \right\} - \frac{i}{2} \ln \left\{ \psi_2^\dagger \psi_1 \right\}, \quad (\text{B.30})$$

$$\theta = \frac{i}{2} \ln \left\{ \psi_1^\dagger \psi_2^\dagger \right\} - \frac{i}{2} \ln \left\{ \psi_1 \psi_2 \right\}. \quad (\text{B.31})$$

Thus,

$$\frac{\partial}{\partial \psi_1^\dagger} (\chi, \sigma, \varphi, \theta) = \frac{1}{2\psi_1^\dagger} (1, 1, i, i). \quad (\text{B.32})$$

Furthermore,

$$\begin{aligned} \hat{V}_{\text{stat}} &= \frac{1}{2} (\psi_1^\dagger \psi_1)^2 + \frac{1}{2} (\psi_2^\dagger \psi_2)^2 - \psi_1^\dagger \psi_1 - \psi_2^\dagger \psi_2 - \epsilon^2 \psi_1^\dagger \psi_2 - \epsilon^2 \psi_2^\dagger \psi_1 \\ &\quad - \frac{1}{4} \lambda^2 \epsilon^2 (\psi_2^\dagger \psi_1 - \psi_1^\dagger \psi_2)^2, \end{aligned} \quad (\text{B.33})$$

$$= \chi^2 + \sigma^2 - 2\epsilon^2 \cos(\varphi) + \lambda^2 \epsilon^2 \sin^2(\varphi) - 1 + \mathcal{O}(\epsilon^3). \quad (\text{B.34})$$

Then,

$$\frac{\partial \hat{V}_{\text{stat}}}{\partial \chi} = 2\chi, \quad (\text{B.35})$$

$$\frac{\partial \hat{V}_{\text{stat}}}{\partial \sigma} = 2\sigma, \quad (\text{B.36})$$

$$\frac{\partial \hat{V}_{\text{stat}}}{\partial \varphi} = 2\epsilon^2 \sin(\varphi) + 2\lambda^2 \epsilon^2 \sin(\varphi) \cos(\varphi), \quad (\text{B.37})$$

$$\frac{\partial \hat{V}_{\text{stat}}}{\partial \theta} = 0. \quad (\text{B.38})$$

For brevity, we momentarily refrain from expanding $\frac{\partial \hat{V}_{\text{stat}}}{\partial \varphi}$ in the SGPE, but note that this quantity is $\mathcal{O}(\epsilon^2)$. Combining the above with Equation (B.32) gives:

$$\frac{\partial \hat{V}_{\text{stat}}}{\partial \psi_1^\dagger} = \frac{1}{\psi_1^\dagger} \left(\chi + \sigma + \frac{i}{2} \frac{\partial \hat{V}_{\text{stat}}}{\partial \varphi} \right). \quad (\text{B.39})$$

Returning to the SGPE

Substituting Equations (B.22), (B.26) & (B.39) into Equation (B.17) gives:

$$\begin{aligned} & \frac{1}{2} \left\{ i(\dot{\chi} + \dot{\sigma}) - (\dot{\varphi} + \dot{\theta}) \right\} \\ &= (1 - i\gamma) \left[-\frac{i}{4} \nabla^2(\varphi + \theta) + \frac{1}{8} (\nabla(\varphi + \theta))^2 + e^{-\chi} e^{-\sigma} \left(\chi + \sigma + \frac{i}{2} \frac{\partial \hat{V}_{\text{stat}}}{\partial \varphi} \right) \right] + \tilde{\eta}_1, \end{aligned} \quad (\text{B.40})$$

$$\begin{aligned} &= (1 - i\gamma) \left[-\frac{i}{4} \nabla^2(\varphi + \theta) + \frac{1}{8} ((\nabla\varphi)^2 + 2\nabla\varphi \cdot \nabla\theta + (\nabla\theta)^2) \right. \\ &\quad \left. + \chi + \sigma + \frac{i}{2} \frac{\partial \hat{V}_{\text{stat}}}{\partial \varphi} - \chi^2 - \sigma^2 - 2\sigma\chi + \mathcal{O}(\epsilon^3) \right] + \tilde{\eta}_1, \end{aligned} \quad (\text{B.41})$$

where $\tilde{\eta}_1 = \psi_1^{-1} \eta_1$. Making the transformations $\psi_1 \rightarrow \psi_2$, $\sigma \rightarrow -\sigma$ and $\varphi \rightarrow -\varphi$, gives an analogous equation for $j = 2$. We have:

$$\begin{aligned} & \frac{1}{2} \left\{ i(\dot{\chi} + \dot{\sigma}) - (\dot{\varphi} + \dot{\theta}) \right\} \\ &= (1 - i\gamma) \left[-\frac{i}{4} \nabla^2(\varphi + \theta) + \frac{1}{8} ((\nabla\varphi)^2 + 2\nabla\varphi \cdot \nabla\theta + (\nabla\theta)^2) \right. \\ &\quad \left. + \chi + \sigma + \frac{i}{2} \frac{\partial \hat{V}_{\text{stat}}}{\partial \varphi} - \chi^2 - \sigma^2 - 2\sigma\chi \right] + \tilde{\eta}_1, \end{aligned} \quad (\text{B.42})$$

$$\begin{aligned} & \frac{1}{2} \left\{ i(\dot{\chi} - \dot{\sigma}) - (-\dot{\varphi} + \dot{\theta}) \right\} \\ &= (1 - i\gamma) \left[-\frac{i}{4} \nabla^2(-\varphi + \theta) + \frac{1}{8} ((\nabla\varphi)^2 - 2\nabla\varphi \cdot \nabla\theta + (\nabla\theta)^2) \right. \\ &\quad \left. + \chi - \sigma - \frac{i}{2} \frac{\partial \hat{V}_{\text{stat}}}{\partial \varphi} - \chi^2 - \sigma^2 + 2\sigma\chi \right] + \tilde{\eta}_2, \end{aligned} \quad (\text{B.43})$$

where $\tilde{\eta}_2 = \psi_2^{-1} \eta_2$.

Equations for $\dot{\varphi}$ and $\dot{\sigma}$

Subtracting Equation (B.43) from Equation (B.42) and collecting real terms gives:

$$\dot{\varphi} = -\frac{1}{2}\nabla\varphi \cdot \nabla\theta - 2\sigma + 4\sigma\chi + \frac{1}{2}\gamma\nabla^2\varphi - \gamma\frac{\partial\hat{V}_{\text{stat}}}{\partial\varphi} + \eta_\varphi, \quad (\text{B.44})$$

$$= -2\sigma + \eta_\varphi + \mathcal{O}(\epsilon^2). \quad (\text{B.45})$$

Collecting imaginary terms gives:

$$\dot{\sigma} = -\frac{1}{2}\nabla^2\varphi + \frac{\partial\hat{V}_{\text{stat}}}{\partial\varphi} - \frac{1}{2}\gamma\nabla\varphi \cdot \nabla\theta - 2\gamma\sigma + 4\gamma\sigma\chi + \eta_\sigma, \quad (\text{B.46})$$

$$= -\frac{1}{2}\nabla^2\varphi + \frac{\partial\hat{V}_{\text{stat}}}{\partial\varphi} - 2\gamma\sigma + \eta_\sigma + \mathcal{O}(\epsilon^3). \quad (\text{B.47})$$

Note, Equations (B.45) & (B.47) have each been truncated to their lowest order in ϵ . It is of no consequence that this order varies between equations.

Since the principal aim of this calculation is to examine fluctuations about the true vacuum state, $\varphi = 0$, we make the additional assumption that $\varphi = \mathcal{O}(\epsilon)$. Then:

$$m_{\text{T}} \equiv \left(\frac{\partial^2\hat{V}_{\text{stat}}}{\partial\varphi^2} \right)^{1/2} = \sqrt{2}\epsilon(\lambda^2 + 1)^{1/2}, \quad (\text{B.48})$$

is the mass of the true vacuum state.

Equations for $\dot{\theta}$ and $\dot{\chi}$

Whilst we are primarily interested in the behaviour of φ , for completeness we proceed to obtain equations for $\dot{\theta}$ and $\dot{\chi}$. Adding Equations (B.42) and (B.43) and collecting real terms gives:

$$\dot{\theta} = -\frac{1}{4}(\nabla\varphi)^2 - \frac{1}{4}(\nabla\theta)^2 - 2\chi + 2\chi^2 + 2\sigma^2 + \frac{1}{2}\gamma\nabla^2\theta + \eta_\theta, \quad (\text{B.49})$$

$$= -2\chi + \eta_\theta + \mathcal{O}(\epsilon^2). \quad (\text{B.50})$$

Collecting imaginary terms gives:

$$\dot{\chi} = -\frac{1}{2}\nabla^2\theta - \frac{1}{4}\gamma(\nabla\varphi)^2 - \frac{1}{4}\gamma(\nabla\theta)^2 - 2\gamma\chi - 2\gamma\chi^2 - 2\gamma\sigma^2 + \eta_\chi, \quad (\text{B.51})$$

$$= -\frac{1}{2}\nabla^2\theta - 2\gamma\chi + \eta_\chi + \mathcal{O}(\epsilon^3). \quad (\text{B.52})$$

It can be shown that $\langle\eta_\alpha^*\eta_\beta\rangle \propto 2\gamma T\delta_{\alpha\beta}$, where $\{\alpha, \beta\} = \{\varphi, \sigma, \theta, \chi\}$.

To Fourier Space and Beyond!

At this stage, it is convenient to move to Fourier space. We use the convention:

$$\hat{f}(k, \omega) = \int_{-\infty}^{\infty} f(x, t) e^{i(kx - \omega t)} dx dt, \quad (\text{B.53})$$

$$f(x, t) = \frac{1}{(2\pi)^2} \int_{-\infty}^{\infty} \hat{f}(k, \omega) e^{-i(kx - \omega t)} dk d\omega, \quad (\text{B.54})$$

for any function $f(x, t)$, so that $\nabla^2 \rightarrow -k^2$ and $\partial/\partial t \rightarrow -i\omega$. Then, Equations (B.45) & (B.47) become:

$$-i\omega\hat{\varphi} = -2\hat{\sigma} + \hat{\eta}_\varphi, \quad (\text{B.55})$$

$$-i\omega\hat{\sigma} = \frac{1}{2}k^2\hat{\varphi} + m_{\text{T}}^2\hat{\varphi} - 2\gamma\hat{\sigma} + \hat{\eta}_\sigma, \quad (\text{B.56})$$

or more compactly:

$$\begin{pmatrix} -i\omega & 2 \\ -\omega_k^2/2 & -i\omega + 2\gamma \end{pmatrix} \begin{pmatrix} \hat{\varphi} \\ \hat{\sigma} \end{pmatrix} = \begin{pmatrix} \hat{\eta}_\varphi \\ \hat{\eta}_\sigma \end{pmatrix}, \quad (\text{B.57})$$

where $\omega_k^2 = k^2 + 2m_{\text{T}}^2$. Inverting this relation gives:

$$\begin{pmatrix} \hat{\varphi} \\ \hat{\sigma} \end{pmatrix} = \frac{1}{\Delta} \begin{pmatrix} i\omega - 2\gamma & 2 \\ -\omega_k^2/2 & i\omega \end{pmatrix} \begin{pmatrix} \hat{\eta}_\varphi \\ \hat{\eta}_\sigma \end{pmatrix}, \quad (\text{B.58})$$

where $\Delta = \omega^2 + 2i\gamma\omega - \omega_k^2$.

Correlation Functions

By design, η_φ and η_σ are Gaussian random variables, which satisfy:

$$\langle \eta_\alpha(x, t) \eta_\alpha(x', t') \rangle = 2\gamma T \delta(x - x') \delta(t - t'), \quad \alpha = \varphi, \sigma, \quad (\text{B.59})$$

$$\langle \eta_\varphi(x, t) \eta_\sigma(x', t') \rangle = 0. \quad (\text{B.60})$$

Therefore,

$$\langle \hat{\eta}_\alpha(k, \omega) \hat{\eta}_\alpha^*(k', \omega') \rangle = 2\gamma T \delta_{kk'} \delta_{\omega\omega'}, \quad (\text{B.61})$$

where $\delta_{qq'} \equiv 2\pi\delta(q - q')$ for any coordinate q . Then, following on from Equation (B.58):

$$\begin{aligned} \langle \hat{\varphi}(k, \omega) \hat{\varphi}^*(k', \omega') \rangle &= \frac{1}{\Delta \Delta'^*} \left[(i\omega - 2\gamma)(-i\omega' - 2\gamma) \langle \hat{\eta}_\varphi(k, \omega) \hat{\eta}_\varphi^*(k', \omega') \rangle \right. \\ &\quad \left. + 4 \langle \hat{\eta}_\sigma(k, \omega) \hat{\eta}_\sigma^*(k', \omega') \rangle \right], \end{aligned} \quad (\text{B.62})$$

$$= \frac{2\gamma T}{\Delta \Delta'^*} [(i\omega - 2\gamma)(-i\omega' - 2\gamma) + 4] \delta_{kk'} \delta_{\omega\omega'}, \quad (\text{B.63})$$

$$= 2\gamma T \left(\frac{\omega^2 + 4\gamma^2 + 4}{(\omega^2 - \omega_k^2)^2 + 4\gamma^2 \omega^2} \right) \delta_{kk'} \delta_{\omega\omega'}. \quad (\text{B.64})$$

From this, we can obtain the equal-time phase correlator in k -space:

$$\langle \hat{\varphi}(k, t) \hat{\varphi}^*(k', t) \rangle = \frac{1}{(2\pi)^2} \int_{-\infty}^{\infty} \langle \hat{\varphi}(k, \omega) \hat{\varphi}^*(k', \omega') \rangle e^{i(\omega - \omega')t} d\omega d\omega', \quad (\text{B.65})$$

$$= \frac{2\gamma T}{(2\pi)^2} \int_{-\infty}^{\infty} \left(\frac{\omega^2 + 4\gamma^2 + 4}{(\omega^2 - \omega_k^2)^2 + 4\gamma^2 \omega^2} \right) e^{i(\omega - \omega')t} \delta_{kk'} \delta_{\omega\omega'} d\omega d\omega', \quad (\text{B.66})$$

$$= 2\gamma T \delta(k - k') \int_{-\infty}^{\infty} \left(\frac{\omega^2 + 4\gamma^2 + 4}{(\omega^2 - \omega_k^2)^2 + 4\gamma^2 \omega^2} \right) d\omega, \quad (\text{B.67})$$

$$= 2\gamma T \delta(k - k') \left(\frac{4\gamma^2 + \omega_k^2 + 4}{2\gamma \omega_k^2} \right) \pi, \quad (\text{B.68})$$

$$\approx \left(\frac{\omega_k^2 + 4}{2\omega_k^2} \right) T \delta_{kk'}, \quad \text{since } \gamma = \mathcal{O}(\epsilon). \quad (\text{B.69})$$

Finally, we arrive at the equal-time phase correlator in x -space:

$$\langle \varphi(x, t) \varphi^*(x', t) \rangle = \frac{1}{(2\pi)^2} \int_{-\infty}^{\infty} \langle \hat{\varphi}(k, t) \hat{\varphi}^*(k', t) \rangle e^{-i(kx - k'x')} dk dk', \quad (\text{B.70})$$

$$= \frac{T}{(2\pi)^2} \int_{-\infty}^{\infty} \left(\frac{\omega_k^2 + 4}{2\omega_k^2} \right) e^{-i(kx - k'x')} \delta_{kk'} dk dk', \quad (\text{B.71})$$

$$= \frac{T}{2\pi} \int_{-\infty}^{\infty} \left(\frac{2}{k^2 + 2m_{\text{T}}^2} + \frac{1}{2} \right) e^{-ik(x - x')} dk, \quad (\text{B.72})$$

$$= \frac{T}{2\pi} \left[\frac{2\pi}{\sqrt{2}m_{\text{T}}} e^{-\sqrt{2}m_{\text{T}}|x - x'|} + \pi \delta(x' - x) \right], \quad (\text{B.73})$$

$$= \frac{T}{\sqrt{2}m_{\text{T}}} e^{-\sqrt{2}m_{\text{T}}r} + \frac{T}{2} \delta(r), \quad (\text{B.74})$$

where $r = |x - x'|$. Note also that $\varphi(x, t)$ is a real function, hence we refer to the above as $\langle \varphi(x, t) \varphi(x', t) \rangle$ in the main text of Section 2.4. Furthermore, in the vicinity of the true

vacuum state, $\langle \varphi(x, t) \rangle = 0$. Thus, here:

$$g(r) = \langle \varphi(x)\varphi(x') \rangle - \langle \varphi(x) \rangle \langle \varphi(x') \rangle = \langle \varphi(x)\varphi(x') \rangle. \quad (\text{B.75})$$

B.4 Instanton exponent

Here, we follow the instanton methodology of Coleman *et al.* [23, 24], as described in Section 1.2.1, to derive the theoretical rate of false vacuum decay, Γ , in a one-dimensional, finite-temperature, two-component Bose gas with stationary interaction potential.

For convenience, we begin by shifting the potential by a constant, such that it equals zero in the false vacuum state. Here, we achieve this by replacing \hat{V}_{stat} with:

$$\tilde{V}_{\text{stat}} = \hat{V}_{\text{stat}} - 2\epsilon^2 + 1. \quad (\text{B.76})$$

This allows us to use Equation (1.21) directly, provided we know the Euclidean action of the bounce, $S_E[\varphi_b]$. By making the Klein-Gordon approximation, we are able to show that the Euclidean action of our system reduces to that of Ref. [27]. This enables us to use the analytic formula for $S_E[\varphi_b]$ derived there.

In order to achieve this, we begin with the action:

$$S[\psi, \psi^\dagger] = \chi \int_{-\infty}^{\infty} dt dx \left[i\psi^\dagger \frac{\partial \psi}{\partial t} - \frac{1}{2} \frac{\partial \psi^\dagger}{\partial x} \frac{\partial \psi}{\partial x} - \tilde{V}_{\text{stat}} \right], \quad (\text{B.77})$$

where the integrand is expressed in terms of dimensionless variables and the parameter χ accounts for any remaining physical quantities. We then move to Euclidean spacetime, by making the transformation:

$$t = i\tau. \quad (\text{B.78})$$

The Euclidean action, $S_E = iS$, is then given by:

$$S_E[\psi, \psi^\dagger] = \chi \int_{-\infty}^{\infty} d\tau dx \left[-\psi^\dagger \frac{\partial \psi}{\partial \tau} + \frac{1}{2} \frac{\partial \psi^\dagger}{\partial x} \frac{\partial \psi}{\partial x} + \tilde{V}_{\text{stat}} \right]. \quad (\text{B.79})$$

Given that we're considering a purely thermal transition, the time-dependence of ψ vanishes, and Equation (B.79) simplifies to:

$$S_E[\psi, \psi^\dagger] = \beta \chi \int_{-\infty}^{\infty} dx \left[\frac{1}{2} \frac{\partial \psi^\dagger}{\partial x} \frac{\partial \psi}{\partial x} + \tilde{V}_{\text{stat}} \right], \quad (\text{B.80})$$

where $\beta = 1/T$.

The next step is to make the Klein-Gordon reduction of Appendix B.3, in the long-

wavelength limit, $\nabla = \mathcal{O}(\epsilon)$, under the assumption that χ , σ and θ are negligible:

$$\psi_1 = e^{i\varphi/2}, \quad (\text{B.81})$$

$$\psi_2 = e^{i\varphi/2}. \quad (\text{B.82})$$

Before proceeding, we note that if not assuming a purely thermal transition, σ -dependence should be included in the above, as in Appendix B.3. Substituting Equations (B.81)-(B.82) into Equation (B.80) yields:

$$S_E[\varphi] = \chi\beta \int_{-\infty}^{\infty} dx \left[\frac{1}{4} \left(\frac{\partial \varphi}{\partial x} \right)^2 + \tilde{V}_{\text{stat}} \right], \quad (\text{B.83})$$

$$= \chi \frac{\alpha(\lambda, \varphi)\epsilon}{T}, \quad (\text{B.84})$$

where,

$$\alpha(\lambda, \varphi) = \frac{1}{4\epsilon} \int_{-\infty}^{\infty} dx \left[\left(\frac{\partial \varphi}{\partial x} \right)^2 + 4\tilde{V}_{\text{stat}} \right]. \quad (\text{B.85})$$

The introduction of ϵ may seem counter-intuitive, however this is necessary to draw analogy with Ref. [27]. If, in addition, we introduce $\tilde{x} = 2\epsilon x$, then:

$$\alpha(\lambda, \varphi) = \int_{-\infty}^{\infty} d\tilde{x} \left[\left(\frac{1}{2} \frac{\partial \varphi}{\partial \tilde{x}} \right)^2 + \mathcal{V} \right], \quad (\text{B.86})$$

where $\mathcal{V} = -1 - \cos(\varphi) + \frac{1}{2}\lambda^2 \sin^2(\varphi)$. This is precisely the integral $\alpha(\lambda, \varphi)$ which appears in Ref. [27]. The authors go on to show that:

$$\alpha(\lambda) \equiv \alpha(\lambda, \varphi_b) = 4 \left\{ (\lambda^2 - 1)^{1/2} - \lambda^{-1} \ln \left[(\lambda^2 - 1)^{1/2} + \lambda \right] \right\}. \quad (\text{B.87})$$

Appendix C

C.1 Klein-Gordon Reduction: Time-Dependent Potential

Here, we complete the Klein-Gordon reduction of the SGPE with oscillatory interaction potential, as outlined in Section 3.3.

The dimensionless SGPE for the spin-1/2 system with oscillatory potential is given by:

$$i \frac{\partial \psi}{\partial t} = (1 - i\gamma) \left[-\frac{1}{2} \frac{\partial^2 \psi}{\partial x^2} + \frac{\partial \hat{V}_{\text{osc}}}{\partial \psi^\dagger} \right] + \eta, \quad (\text{C.1})$$

where,

$$\hat{V}_{\text{osc}} = \frac{1}{2} \sum_{j=1,2} (\psi_j^\dagger \psi_j)^2 - \psi^\dagger \psi - (\epsilon^2 + \delta\omega \cos(\omega t)) \psi^\dagger \sigma_x \psi. \quad (\text{C.2})$$

The aim of this calculation is to characterize the extrema of V_{osc} . Thus, as in Appendix B.3, we make the ansatz:

$$\psi_1 = e^{\chi/2} e^{\sigma/2} e^{i\varphi/2} e^{i\theta/2}, \quad (\text{C.3})$$

$$\psi_2 = \pm e^{\chi/2} e^{-\sigma/2} e^{-i\varphi/2} e^{i\theta/2}, \quad (\text{C.4})$$

where χ , σ , φ and θ represent fluctuations in global density, relative density, relative phase, and total phase. The positive and negative signs of ψ_2 correspond to expansion about $\varphi = 0$ and $\varphi = \pi$, respectively. Only the interaction term differs from the SGPE examined in Appendix B.3. Substituting Equations (C.3)-(C.4) into Equation (C.2) yields:

$$\hat{V}_{\text{osc}} = \frac{1}{2} e^{2\chi} \left[e^{2\sigma} + e^{-2\sigma} \right] - e^\chi \left[e^\sigma + e^{-\sigma} \right] \mp (\epsilon^2 + \delta\omega \cos(\omega t)) e^\chi \left[e^{i\varphi} + e^{-i\varphi} \right], \quad (\text{C.5})$$

which, making use of Equation (B.32), gives:

$$\frac{\partial \hat{V}_{\text{osc}}}{\partial \psi_1} = \frac{1}{\psi_1^\dagger} \left[e^{2\chi} e^{2\sigma} - e^{\chi} e^{\sigma} \mp (\epsilon^2 + \delta\omega \cos(\omega t)) e^{\chi} e^{-i\varphi} \right]. \quad (\text{C.6})$$

Substituting equations (B.22), (B.25) & (C.6) into the SGPE (C.1) and linearizing in $\{\chi, \sigma, \varphi, \theta\}$ gives:

$$\begin{aligned} \frac{1}{2} \left\{ i(\dot{\chi} + \dot{\sigma}) - (\dot{\varphi} + \dot{\theta}) \right\} &= (1 - i\gamma) \left[-\frac{1}{4} \nabla^2 \{(\chi + \sigma) + i(\varphi + \theta)\} + \chi + \sigma \right. \\ &\quad \left. \mp (\epsilon^2 + \delta\omega \cos(\omega t)) \{1 - \sigma - i\varphi\} \right] + \tilde{\eta}_1, \end{aligned} \quad (\text{C.7})$$

where $\tilde{\eta}_1 = \psi_1^{-1} \eta_1$. Note the contrast between the kinetic terms of the above and those of Equation (B.42). Here, we have not taken the long-wavelength limit, nor have we assumed that any of $\{\chi, \sigma, \varphi, \theta\}$ dominate. By making the transformations $\psi_1 \rightarrow \psi_2$, $\sigma \rightarrow -\sigma$ and $\varphi \rightarrow -\varphi$, we arrive at an analogous equation for $j = 2$:

$$\begin{aligned} \frac{1}{2} \left\{ i(\dot{\chi} - \dot{\sigma}) - (-\dot{\varphi} + \dot{\theta}) \right\} &= (1 - i\gamma) \left[-\frac{1}{4} \nabla^2 \{(\chi - \sigma) + i(-\varphi + \theta)\} + \chi - \sigma \right. \\ &\quad \left. \mp (\epsilon^2 + \delta\omega \cos(\omega t)) \{1 + \sigma + i\varphi\} \right] + \tilde{\eta}_2. \end{aligned} \quad (\text{C.8})$$

Subtracting Equation (C.8) from (C.7) and collecting real and imaginary terms gives:

$$\dot{\varphi} = \frac{1}{2} \nabla^2 \sigma + \frac{1}{2} \gamma \nabla^2 \varphi - 2\sigma \mp 2(\epsilon^2 + \delta\omega \cos(\omega t)) \{\sigma + \gamma\varphi\} + \eta_\varphi, \quad (\text{C.9})$$

$$\dot{\sigma} = -\frac{1}{2} \nabla^2 \varphi + \frac{1}{2} \gamma \nabla^2 \sigma - 2\gamma\sigma \pm 2(\epsilon^2 + \delta\omega \cos(\omega t)) \{\varphi - \gamma\sigma\} + \eta_\sigma. \quad (\text{C.10})$$

Similarly, adding Equations (C.7) and (C.8) gives:

$$\dot{\theta} = \frac{1}{2} \nabla^2 \chi + \frac{1}{2} \gamma \nabla^2 \theta - 2\chi \pm 2(\epsilon^2 + \delta\omega \cos(\omega t)) + \eta_\theta, \quad (\text{C.11})$$

$$\dot{\chi} = -\frac{1}{2} \nabla^2 \theta + \frac{1}{2} \gamma \nabla^2 \chi - 2\gamma\chi \pm 2\gamma(\epsilon^2 + \delta\omega \cos(\omega t)) + \eta_\chi. \quad (\text{C.12})$$

Again, it can be shown that $\langle \eta_\alpha^* \eta_\beta \rangle \propto 2\gamma T \delta_{\alpha\beta}$, where $\{\alpha, \beta\} = \{\varphi, \sigma, \theta, \chi\}$. Notice that the relative phase, φ , couples only to the relative density variation, σ . Fourier transforming

Equations (C.9)-(C.10) in space yields:

$$\frac{\partial \hat{\varphi}}{\partial t} = -(a \pm 2\delta\omega \cos(\omega t))\hat{\sigma} - \gamma(b \pm 2\delta\omega \cos(\omega t))\hat{\varphi} + \hat{\eta}_\varphi, \quad (\text{C.13})$$

$$\frac{\partial \hat{\sigma}}{\partial t} = -\gamma(a \pm 2\delta\omega \cos(\omega t))\hat{\sigma} + (b \pm 2\delta\omega \cos(\omega t))\hat{\varphi} + \hat{\eta}_\sigma, \quad (\text{C.14})$$

where,

$$a = \frac{1}{2}k^2 + 2 \pm 2\epsilon^2, \quad b = \frac{1}{2}k^2 \pm 2\epsilon^2. \quad (\text{C.15})$$

In order to find a time-averaged effective description of V_{osc} , we set:

$$\hat{\varphi} = \varphi_0 + \varphi_1 \cos(\omega t) + \varphi_2 \sin(\omega t), \quad (\text{C.16})$$

$$\hat{\sigma} = \sigma_0 + \sigma_1 \sin(\omega t) + \sigma_2 \cos(\omega t), \quad (\text{C.17})$$

under the assumptions that $\varphi_{\{1,2\}}$ and $\sigma_{\{1,2\}}$ are small compared to φ_0 and σ_0 , vary slowly compared to the sinusoidal terms, and $\omega^2 \gg ab$. Then:

$$\frac{\partial \hat{\varphi}}{\partial t} \approx \dot{\varphi}_0 - \omega\varphi_1 \sin(\omega t) + \omega\varphi_2 \cos(\omega t), \quad (\text{C.18})$$

$$\frac{\partial \hat{\sigma}}{\partial t} \approx \dot{\sigma}_0 + \omega\sigma_1 \cos(\omega t) - \omega\sigma_2 \sin(\omega t). \quad (\text{C.19})$$

Substituting Equations (C.16)-(C.19) into Equations (C.13)-(C.14) and collecting coefficients of $\sin(\omega t)$ and $\cos(\omega t)$ gives:

$$\varphi_1 = \frac{a}{\omega}\sigma_1 + \frac{\gamma b}{\omega}\varphi_2, \quad (\text{C.20})$$

$$\varphi_2 = \mp 2\delta\sigma_0 \mp 2\gamma\delta\varphi_0 - \frac{a}{\omega}\sigma_2 - \frac{\gamma b}{\omega}\varphi_1, \quad (\text{C.21})$$

$$\sigma_1 = \pm 2\delta\varphi_0 \mp 2\gamma\delta\sigma_0 + \frac{b}{\omega}\varphi_1 - \frac{\gamma a}{\omega}\sigma_2, \quad (\text{C.22})$$

$$\sigma_2 = -\frac{b}{\omega}\varphi_2 + \frac{\gamma a}{\omega}\sigma_1. \quad (\text{C.23})$$

By making the use of the assumption $\omega^2 \gg ab$, and neglecting lowest order terms, each of the above quantities may be reformulated in terms of φ_0 and σ_0 :

$$\varphi_1 = \pm \frac{2\delta a}{\omega}(\varphi_0 - \gamma\sigma_0), \quad (\text{C.24})$$

$$\varphi_2 = \mp 2\delta(\sigma_0 + \gamma\varphi_0), \quad (\text{C.25})$$

$$\sigma_1 = \pm 2\delta(\varphi_0 - \gamma\sigma_0), \quad (\text{C.26})$$

$$\sigma_2 = \pm \frac{2\delta b}{\omega}(\sigma_0 + \gamma\varphi_0). \quad (\text{C.27})$$

Substituting Equations (C.24)-(C.27) into Equations (C.13)-(C.14), via Equations (C.16)-(C.19), and taking the period average of each gives:

$$\dot{\varphi}_0 = -[a + 2\delta^2 b - 2\gamma^2 \delta^2 a] \sigma_0 - \gamma [b + 2\delta^2 a + 2\delta^2 b] \varphi_0 + \bar{\hat{\eta}}_\varphi, \quad (\text{C.28})$$

$$\dot{\sigma}_0 = +[b + 2\delta^2 a - 2\gamma^2 \delta^2 b] \varphi_0 - \gamma [a + 2\delta^2 a + 2\delta^2 b] \sigma_0 + \bar{\hat{\eta}}_\sigma, \quad (\text{C.29})$$

where bars denote a period average. Here, we have made use of $\overline{\cos^2(\omega t)} = \overline{\sin^2(\omega t)} = \frac{1}{2}$ and $\overline{\cos(\omega t)} = \overline{\sin(\omega t)} = \overline{\sin(\omega t) \cos(\omega t)} = 0$. By neglecting terms of order $\mathcal{O}(\gamma \delta^2)$ and taking the long-wavelength limit, $k \ll 1$, Equations (C.28)-(C.29) simplify to:

$$\dot{\varphi}_0 = -2\sigma_0 + \bar{\hat{\eta}}_\varphi, \quad (\text{C.30})$$

$$\dot{\sigma}_0 = \frac{1}{2}\omega_k^2 \varphi_0 - 2\gamma\sigma_0 + \bar{\hat{\eta}}_\sigma, \quad (\text{C.31})$$

where $\omega_k^2 = k^2 + 4\epsilon^2(\lambda^2 \pm 1)$. Finally, by eliminating σ_0 , we arrive at a damped Klein-Gordon equation for φ_0 , with noise η_{eff} :

$$\ddot{\varphi}_0 + 2\gamma\dot{\varphi}_0 + \omega_k^2 \varphi_0 = \eta_{\text{eff}}. \quad (\text{C.32})$$

C.2 Parametric Resonance: Growth Rate

In order to determine the growth rate, Γ_{PR} , of the parametric resonance, we make the ansatz:

$$\varphi = A(t) \cos(\omega t/2) + B(t) \sin(\omega t/2), \quad (\text{C.33})$$

$$\sigma = C(t) \cos(\omega t/2) + D(t) \sin(\omega t/2), \quad (\text{C.34})$$

where $A - D$ vary slowly in time compared to the sinusoidal terms. By substituting Equations (C.33)-(C.34) into Equations (C.13)-(C.14), we arrive at:

$$\begin{aligned} \dot{A}c + \dot{B}s + \frac{\omega}{2}(Bc - As) &= -[a + 2\delta\omega(c^2 - s^2)](Cc + Ds) \\ &\quad - \gamma[b + 2\delta\omega(c^2 - s^2)](Ac + Bs), \end{aligned} \quad (\text{C.35})$$

$$\begin{aligned} \dot{C}c + \dot{D}s + \frac{\omega}{2}(Dc - Cs) &= [b + 2\delta\omega(c^2 - s^2)](Ac + Bs) \\ &\quad - \gamma[a + 2\delta\omega(c^2 - s^2)](Cc + Ds), \end{aligned} \quad (\text{C.36})$$

where $c \equiv \cos(\omega/2)$ and $s \equiv \sin(\omega/2)$. When expanded, each term of the above is proportional to $c^n s^m$, where $n + m$ is odd. Therefore, we gain nothing by taking the period averages of these equations as they stand. However, by multiplying each by c and s

independently, to obtain four equations in total, and *then* period averaging, we obtain:

$$\begin{pmatrix} \dot{A} \\ \dot{B} \\ \dot{C} \\ \dot{D} \end{pmatrix} = \begin{pmatrix} -\gamma b & -\omega/2 & -(a \pm \delta\omega) & 0 \\ \omega/2 & -\gamma b & 0 & \pm\delta\omega - a \\ b \pm \delta\omega & 0 & -\gamma a & -\omega/2 \\ 0 & -(\pm\delta\omega - b) & \omega/2 & -\gamma a \end{pmatrix} \begin{pmatrix} A \\ B \\ C \\ D \end{pmatrix}. \quad (\text{C.37})$$

Note that above we have neglected terms of order $\mathcal{O}(\gamma\delta)$. Let $\lambda_{\{1,2,3,4\}}$ denote the eigenvalues of this linear system, and $\boldsymbol{\eta}_{\{1,2,3,4\}}$ denote the corresponding eigenvectors. Then, the general solution of Equation (C.37) is given by:

$$\mathbf{A}(t) = \sum_{j=1}^4 c_j e^{\lambda_j t} \boldsymbol{\eta}_j, \quad (\text{C.38})$$

where $\mathbf{A} = (A, B, C, D)$ and c_j are arbitrary constants. Equation (C.38) is then dominated by the eigenvalue with largest real part, which we denote λ_+ . This is given by:

$$\lambda_+ = \frac{1}{2} \left\{ \left[2(4a^2\delta^2\omega^2 - a^2\gamma^2\omega^2 + 8ab\delta^2\omega^2 + 2ab\gamma^2\omega^2 + 4ab\omega^2 + 4b^2\delta^2\omega^2 - b^2\gamma^2\omega^2)^{1/2} \right. \right. \\ \left. \left. + a^2\gamma^2 - 2ab\gamma^2 - 4ab + b^2\gamma^2 - 4\delta^2\omega^2 - \omega^2 \right]^{1/2} - \gamma(a + b) \right\}. \quad (\text{C.39})$$

Therefore, the growth rate of $A - D$ is given by:

$$\Gamma_{\text{PR}} = \text{Re}(\lambda_+). \quad (\text{C.40})$$

Appendix D

D.1 Spin 1 System: Klein Gordon Reduction

In terms of the dimensionless units introduced in Section 4.3, the Lagrangian density of the spin-1 system is given by:

$$\mathcal{L} = i\psi^\dagger \frac{\partial\psi}{\partial t} - \frac{1}{2}(\nabla\psi^\dagger) \cdot (\nabla\psi) - V_{\text{int}}, \quad (\text{D.1})$$

with interaction potential:

$$\begin{aligned} V_{\text{int}}(\psi^\dagger, \psi) = & -\mu\psi^\dagger\psi + \frac{1}{2}(\psi^\dagger\psi)^2 + \frac{1}{2}\frac{g'}{g}(\psi^\dagger\mathbf{J}\psi)^2 + \omega_q(\psi^\dagger J_z^2\psi) \\ & + \frac{1}{2}\epsilon^2\psi^\dagger J_x\psi - \frac{1}{8}\epsilon^2\lambda^2\psi^\dagger(J_+^2 + J_-^2)\psi. \end{aligned} \quad (\text{D.2})$$

In order to reduce the Lagrangian to that of a Klein-Gordon system, we expand the wavefunctions about the false vacuum state, $\varphi = 0$, under the assumption that $\theta \approx 0$. Thus, we make the ansatz:

$$\psi_{+1} = \zeta e^{\sigma/2} e^{i\varphi}, \quad (\text{D.3})$$

$$\psi_0 = \zeta', \quad (\text{D.4})$$

$$\psi_{-1} = \zeta e^{-\sigma/2} e^{-i\varphi}, \quad (\text{D.5})$$

where σ represents fluctuations in the relative density between $|+1\rangle$ and $| -1\rangle$, and we define:

$$\zeta = \frac{1}{2}\left(1 + \frac{g\omega_q}{2g'}\right)^{1/2} \quad \text{and} \quad \zeta' = \sqrt{1 - 2\zeta^2}. \quad (\text{D.6})$$

Going forward, we assume $\sigma = \mathcal{O}(\epsilon)$, where $\epsilon \ll 1$. Then, by making use of the relations:

$$2\zeta^2 + \zeta'^2 = 1, \quad (\text{D.7})$$

$$\mu = 1 + \frac{g'}{g} + \frac{\omega_q}{2}, \quad (\text{D.8})$$

and neglecting terms constant in (θ, φ) space, we arrive at:

$$V_{\text{int}} = \zeta^2 \left[\frac{\omega_q}{2} \sigma^2 + \sqrt{2} \epsilon^2 \frac{\zeta'}{\zeta} \cos(\varphi) + \epsilon^2 \lambda^2 \sin^2(\varphi) \right]. \quad (\text{D.9})$$

It remains to substitute ansatz (D.3)-(D.5) into the derivative terms of the Lagrangian. We find:

$$\psi^\dagger \frac{\partial \psi}{\partial t} = [\dot{\sigma} + 2i\dot{\varphi}] \zeta^2 \sinh(\sigma), \quad (\text{D.10})$$

$$\approx 2i\sigma\zeta^2\dot{\varphi}, \quad (\text{D.11})$$

and,

$$(\nabla \psi^\dagger) \cdot (\nabla \psi) = \left[\frac{1}{2} (\nabla \sigma)^2 + 2(\nabla \varphi)^2 \right] \zeta^2 \cosh(\sigma), \quad (\text{D.12})$$

$$\approx 2\zeta^2 (\nabla \varphi)^2. \quad (\text{D.13})$$

Therefore, the Lagrangian density becomes:

$$\mathcal{L} = \zeta^2 \left[-2\sigma\dot{\varphi} - (\nabla \varphi)^2 - \frac{\omega_q}{2} \sigma^2 - \sqrt{2} \epsilon^2 \frac{\zeta'}{\zeta} \cos(\varphi) - \epsilon^2 \lambda^2 \sin^2(\varphi) \right]. \quad (\text{D.14})$$

We wish to remove the σ dependence from \mathcal{L} . This can be achieved by varying \mathcal{L} with respect to σ . We find:

$$\sigma = -\frac{2\dot{\varphi}}{\omega_q}, \quad (\text{D.15})$$

and we arrive at an effective Klein-Gordon Lagrangian:

$$\mathcal{L}_{\text{eff}} = 2\zeta^2 \left[\frac{\dot{\varphi}^2}{2c^2} - \frac{1}{2} (\nabla \varphi)^2 - V_{\text{eff}}(\varphi) \right], \quad (\text{D.16})$$

where $c^2 = \omega_q/2$,

$$V_{\text{eff}} = \epsilon^2 \lambda_c^2 \cos(\varphi) + \frac{1}{2} \epsilon^2 \lambda^2 \sin^2(\varphi), \quad (\text{D.17})$$

and,

$$\lambda_c = \left(\frac{1 - g\omega_q/(2g')}{1 + g\omega_q/(2g')} \right)^{1/4}. \quad (\text{D.18})$$

Bibliography

- [1] M. Hindmarsh, M. Lüben, J. Lumma, and M. Pauly, SciPost Phys. Lect. Notes p. 24 (2021), URL <https://scipost.org/10.21468/SciPostPhysLectNotes.24>.
- [2] A. Mazumdar and G. White, Rept. Prog. Phys. **82**, 076901 (2019), URL <https://iopscience.iop.org/article/10.1088/1361-6633/ab1f55>.
- [3] Planck Collaboration, N. Aghanim, Y. Akrami, M. Ashdown, J. Aumont, C. Bacigalupi, M. Ballardini, A. J. Banday, R. B. Barreiro, N. Bartolo, et al., A&A **641**, A6 (2020), URL <https://ui.adsabs.harvard.edu/abs/2020A&A...641A...6P/abstract>.
- [4] A. H. Guth, Phys. Rev. D **23**, 347 (1981), URL <https://link.aps.org/doi/10.1103/PhysRevD.23.347>.
- [5] S. W. Hawking, I. G. Moss, and J. M. Stewart, Phys. Rev. D **26**, 2681 (1982), URL <https://journals.aps.org/prd/abstract/10.1103/PhysRevD.26.2681>.
- [6] A. Linde, Physics Letters B **108**, 389 (1982), ISSN 0370-2693, URL <https://www.sciencedirect.com/science/article/pii/0370269382912199>.
- [7] A. Albrecht and P. J. Steinhardt, Phys. Rev. Lett. **48**, 1220 (1982), URL <https://link.aps.org/doi/10.1103/PhysRevLett.48.1220>.
- [8] S. Hawking and I. Moss, Physics Letters B **110**, 35 (1982), ISSN 0370-2693, URL <https://www.sciencedirect.com/science/article/pii/0370269382909467>.
- [9] I. G. Moss, Contemporary Physics **56**, 468 (2015), URL <https://doi.org/10.1080/00107514.2015.1058543>.
- [10] H. Kodama, M. Sasaki, and K. Sato, Progress of Theoretical Physics **68**, 1979 (1982), ISSN 0033-068X, URL <https://academic.oup.com/ptp/article-pdf/68/6/1979/5311817/68-6-1979.pdf>.
- [11] H. Deng and A. Vilenkin, JCAP **1712**, 044 (2017), URL <https://iopscience.iop.org/article/10.1088/1475-7516/2017/12/044>.

- [12] A. Kosowsky, M. S. Turner, and R. Watkins, Phys. Rev. D **45**, 4514 (1992), URL <https://link.aps.org/doi/10.1103/PhysRevD.45.4514>.
- [13] M. Kamionkowski, A. Kosowsky, and M. S. Turner, Phys. Rev. D **49**, 2837 (1994), URL <https://link.aps.org/doi/10.1103/PhysRevD.49.2837>.
- [14] C. Caprini, R. Durrer, T. Konstandin, and G. Servant, Phys. Rev. D **79**, 083519 (2009), URL <https://journals.aps.org/prd/abstract/10.1103/PhysRevD.79.083519>.
- [15] M. Hindmarsh, S. J. Huber, K. Rummukainen, and D. J. Weir, Phys. Rev. Lett. **112**, 041301 (2014), URL <https://journals.aps.org/prl/abstract/10.1103/PhysRevLett.112.041301>.
- [16] A. D. Sakharov, Pisma Zh. Eksp. Teor. Fiz. **5**, 32 (1967), URL <https://iopscience.iop.org/article/10.1070/PU1991v034n05ABEH002497>.
- [17] A. G. Cohen, D. B. Kaplan, and A. E. Nelson, Annual Review of Nuclear and Particle Science **43**, 27 (1993), URL <https://doi.org/10.1146/annurev.ns.43.120193.000331>.
- [18] G. M. Fuller, G. J. Mathews, and C. R. Alcock, Phys. Rev. D **37**, 1380 (1988), URL <https://link.aps.org/doi/10.1103/PhysRevD.37.1380>.
- [19] T. Inoue, S. Aoki, T. Doi, T. Hatsuda, Y. Ikeda, N. Ishii, K. Murano, H. Nemura, and K. Sasaki, Nuclear Physics A **881**, 28 (2012), ISSN 0375-9474, URL <https://www.sciencedirect.com/science/article/pii/S0375947412000760>.
- [20] S. M. Feeney, M. C. Johnson, J. D. McEwen, D. J. Mortlock, and H. V. Peiris, Phys. Rev. D **88**, 043012 (2013), URL <https://link.aps.org/doi/10.1103/PhysRevD.88.043012>.
- [21] M. Paranjape, *The Theory and Applications of Instanton Calculations* (Cambridge University Press, 2022), ISBN 978-1-009-29123-1.
- [22] T. Lancaster and S. J. Blundell, *Quantum Field Theory for the Gifted Amateur, 3rd Edition* (Oxford University Press, 2018), ISBN 978-0-19-969933-9.
- [23] S. R. Coleman, Phys. Rev. D **15**, 2929 (1977), [Erratum: Phys. Rev. D 16, 1248 (1977)], URL <https://journals.aps.org/prd/abstract/10.1103/PhysRevD.15.2929>.
- [24] C. G. Callan and S. R. Coleman, Phys. Rev. D **16**, 1762 (1977), URL <https://journals.aps.org/prd/abstract/10.1103/PhysRevD.16.1762>.

- [25] S. R. Coleman and F. De Luccia, Phys. Rev. D **21**, 3305 (1980), URL <https://journals.aps.org/prd/abstract/10.1103/PhysRevD.21.3305>.
- [26] A. D. Linde, Nucl. Phys. B **216**, 421 (1983), [Erratum: Nucl.Phys.B 223, 544 (1983)], URL <https://www.sciencedirect.com/science/article/abs/pii/0550321383902936>.
- [27] M. Gutierrez Abed and I. G. Moss, Phys. Rev. D **107**, 076027 (2023), URL <https://link.aps.org/doi/10.1103/PhysRevD.107.076027>.
- [28] T. Treu et al., Astrophys. J. **935**, 110 (2022), URL <https://iopscience.iop.org/article/10.3847/1538-4357/ac8158>.
- [29] G. F. Smoot, Rev. Mod. Phys. **79**, 1349 (2007), URL <https://link.aps.org/doi/10.1103/RevModPhys.79.1349>.
- [30] Planck Collaboration, Aghanim, N., Akrami, Y., Arroja, F., Ashdown, M., Aumont, J., Baccigalupi, C., Ballardini, M., Banday, A. J., Barreiro, R. B., et al., A&A **641**, A1 (2020), URL <https://doi.org/10.1051/0004-6361/201833880>.
- [31] W. G. Unruh, Phys. Rev. Lett. **46**, 1351 (1981), URL <https://journals.aps.org/prl/abstract/10.1103/PhysRevLett.46.1351>.
- [32] P. Jain, A. S. Bradley, and C. W. Gardiner, Phys. Rev. A **76**, 023617 (2007), URL <https://link.aps.org/doi/10.1103/PhysRevA.76.023617>.
- [33] J. Steinhauer, Nature Phys. **12**, 959 (2016), URL <https://www.nature.com/articles/nphys3863>.
- [34] J. R. M. de Nova, K. Golubkov, V. I. Kolobov, and J. Steinhauer, Nature **569**, 688–691 (2018), URL <https://www.nature.com/articles/s41586-019-1241-0>.
- [35] Y.-H. Wang, T. Jacobson, M. Edwards, and C. W. Clark, Phys. Rev. A **96**, 023616 (2017), URL <https://link.aps.org/doi/10.1103/PhysRevA.96.023616>.
- [36] C. Barcelo, S. Liberati, and M. Visser, Living Rev. Rel. **14**, 3 (2011), URL <https://link.springer.com/article/10.12942/lrr-2011-3>.
- [37] S. Eckel, A. Kumar, T. Jacobson, I. B. Spielman, and G. K. Campbell, Phys. Rev. X **8**, 021021 (2018), URL <https://journals.aps.org/prx/abstract/10.1103/PhysRevX.8.021021>.
- [38] T. Roger, C. Maitland, K. Wilson, N. Westerberg, D. Vocke, E. M. Wright, and D. Faccio, Nature Communications **7**, 13492 (2016), URL <https://www.nature.com/articles/ncomms13492>.

- [39] O. Fialko, B. Opanchuk, A. I. Sidorov, P. D. Drummond, and J. Brand, Europhysics Letters **110**, 56001 (2015), URL <https://iopscience.iop.org/article/10.1209/0295-5075/110/56001>.
- [40] P. L. Kapitza, Soviet Phys. JETP. **21**, 588–597 (1951).
- [41] O. Fialko, B. Opanchuk, A. I. Sidorov, P. D. Drummond, and J. Brand, Journal of Physics B Atomic Molecular Physics **50**, 024003 (2017), URL <https://iopscience.iop.org/article/10.1088/1361-6455/50/2/024003/meta>.
- [42] J. Braden, M. C. Johnson, H. V. Peiris, A. Pontzen, and S. Weinfurtner, Phys. Rev. Lett. **123**, 031601 (2019), [Erratum: Phys.Rev.Lett. 129, 059901 (2022)], URL <https://journals.aps.org/prl/abstract/10.1103/PhysRevLett.123.031601>.
- [43] J. Braden, M. C. Johnson, H. V. Peiris, and S. Weinfurtner, JHEP **07**, 014 (2018), URL [https://link.springer.com/article/10.1007/JHEP07\(2018\)014](https://link.springer.com/article/10.1007/JHEP07(2018)014).
- [44] J. Braden, M. C. Johnson, H. V. Peiris, A. Pontzen, and S. Weinfurtner, JHEP **10**, 174 (2019), URL [https://link.springer.com/article/10.1007/JHEP10\(2019\)174](https://link.springer.com/article/10.1007/JHEP10(2019)174).
- [45] M. P. Hertzberg, F. Rompineve, and N. Shah, Phys. Rev. D **102**, 076003 (2020), URL <https://journals.aps.org/prd/abstract/10.1103/PhysRevD.102.076003>.
- [46] T. P. Billam, R. Gregory, F. Michel, and I. G. Moss, Phys. Rev. D **100**, 065016 (2019), URL <https://link.aps.org/doi/10.1103/PhysRevD.100.065016>.
- [47] T. P. Billam, K. Brown, and I. G. Moss, Phys. Rev. A **102**, 043324 (2020), URL <https://link.aps.org/doi/10.1103/PhysRevA.102.043324>.
- [48] K. L. Ng, B. Opanchuk, M. Thenabadu, M. Reid, and P. D. Drummond, PRX Quantum **2**, 010350 (2021), URL <https://journals.aps.org/prxquantum/abstract/10.1103/PRXQuantum.2.010350>.
- [49] T. P. Billam, K. Brown, A. J. Groszek, and I. G. Moss, Phys. Rev. A **104**, 053309 (2021), URL <https://link.aps.org/doi/10.1103/PhysRevA.104.053309>.
- [50] T. P. Billam, K. Brown, and I. G. Moss, Phys. Rev. A **105**, L041301 (2022), URL <https://link.aps.org/doi/10.1103/PhysRevA.105.L041301>.
- [51] D. Pirvu, J. Braden, and M. C. Johnson, Phys. Rev. D **105**, 043510 (2022), URL <https://journals.aps.org/prd/abstract/10.1103/PhysRevD.105.043510>.

- [52] J. Braden, M. C. Johnson, H. V. Peiris, A. Pontzen, and S. Weinfurtner, Phys. Rev. D **107**, 083509 (2023), URL <https://link.aps.org/doi/10.1103/PhysRevD.107.083509>.
- [53] T. P. Billam, K. Brown, and I. G. Moss, New Journal of Physics **25**, 043028 (2023), URL <https://dx.doi.org/10.1088/1367-2630/accca2>.
- [54] A. Zenesini, A. Berti, R. Cominotti, C. Rogora, I. G. Moss, T. P. Billam, I. Carusotto, G. Lamporesi, A. Recati, and G. Ferrari, Nature **569** (2024), URL <https://www.nature.com/articles/s41567-023-02345-4>.
- [55] A. C. Jenkins, J. Braden, H. V. Peiris, A. Pontzen, M. C. Johnson, and S. Weinfurtner (2023), arXiv preprint, 2307.02549, URL <https://arxiv.org/abs/2307.02549>.
- [56] M. Planck, Ann. Phys. **1**, 719 (1900).
- [57] S. N. Bose, Z.Phys **26**, 178 (1924).
- [58] A. Einstein, Sitzber. Kgl. Preuss. Akad. Wiss. **22** (1924).
- [59] A. Einstein, Sitzber. Kgl. Preuss. Akad. Wiss. **23** (1925).
- [60] J. F. Annett, *Superconductivity, superfluids, and condensates*, Oxford master series in condensed matter physics (Oxford University Press, 2004), ISBN 0198507550.
- [61] L. V. P. R. de Broglie, Annales de Physique **3** (1925).
- [62] R. P. Smith and Z. Hadzibabic, *Effects of Interactions on Bose-Einstein Condensation of an Atomic Gas* (Springer Berlin Heidelberg, Berlin, Heidelberg, 2013), pp. 341–359, ISBN 978-3-642-37569-9, URL https://doi.org/10.1007/978-3-642-37569-9_16.
- [63] M. H. Anderson, J. R. Ensher, M. R. Matthews, C. E. Wieman, and E. A. Cornell, Science **269**, 198 (1995), URL <https://www.science.org/doi/10.1126/science.269.5221.198>.
- [64] S. Chu, Rev. Mod. Phys. **70**, 685 (1998), URL <https://link.aps.org/doi/10.1103/RevModPhys.70.685>.
- [65] C. N. Cohen-Tannoudji, Rev. Mod. Phys. **70**, 707 (1998), URL <https://link.aps.org/doi/10.1103/RevModPhys.70.707>.
- [66] W. D. Phillips, Rev. Mod. Phys. **70**, 721 (1998), URL <https://link.aps.org/doi/10.1103/RevModPhys.70.721>.

- [67] K. B. Davis, M. O. Mewes, M. R. Andrews, N. J. van Druten, D. S. Durfee, D. M. Kurn, and W. Ketterle, Phys. Rev. Lett. **75**, 3969 (1995), URL <https://link.aps.org/doi/10.1103/PhysRevLett.75.3969>.
- [68] I. Bouchoule, M. Arzamasovs, K. V. Kheruntsyan, and D. M. Gangardt, Phys. Rev. A **86**, 033626 (2012), URL <https://link.aps.org/doi/10.1103/PhysRevA.86.033626>.
- [69] T. Langen, S. Erne, R. Geiger, B. Rauer, T. Schweigler, M. Kuhnert, W. Rohringer, I. E. Mazets, T. Gasenzer, and J. Schmiedmayer, Science **348**, 207 (2015), URL <https://www.science.org/doi/abs/10.1126/science.1257026>.
- [70] A. Görlitz, J. M. Vogels, A. E. Leanhardt, C. Raman, T. L. Gustavson, J. R. Abo-Shaeer, A. P. Chikkatur, S. Gupta, S. Inouye, T. Rosenband, et al., Phys. Rev. Lett. **87**, 130402 (2001), URL <https://link.aps.org/doi/10.1103/PhysRevLett.87.130402>.
- [71] S. Erne, R. Bücker, T. Gasenzer, J. Berges, and J. Schmiedmayer, Nature **563**, 225 (2018), ISSN 1476-4687, URL <https://doi.org/10.1038/s41586-018-0667-0>.
- [72] M. Prüfer, P. Kunkel, H. Strobel, S. Lannig, D. Linnemann, C.-M. Schmied, J. Berges, T. Gasenzer, and M. K. Oberthaler, Nature **563**, 217 (2018), ISSN 1476-4687, URL <https://doi.org/10.1038/s41586-018-0659-0>.
- [73] K. V. Kheruntsyan, D. M. Gangardt, P. D. Drummond, and G. V. Shlyapnikov, Phys. Rev. Lett. **91**, 040403 (2003), URL <https://link.aps.org/doi/10.1103/PhysRevLett.91.040403>.
- [74] K. V. Kheruntsyan, D. M. Gangardt, P. D. Drummond, and G. V. Shlyapnikov, Phys. Rev. A **71**, 053615 (2005), URL <https://link.aps.org/doi/10.1103/PhysRevA.71.053615>.
- [75] C. Henkel, T.-O. Sauer, and N. P. Proukakis, Journal of Physics B: Atomic, Molecular and Optical Physics **50**, 114002 (2017), URL <https://doi.org/10.1088%2F1361-6455%2Fa6888>.
- [76] N. Prokof'ev, O. Ruebenacker, and B. Svistunov, Phys. Rev. Lett. **87**, 270402 (2001), URL <https://link.aps.org/doi/10.1103/PhysRevLett.87.270402>.
- [77] D. J. Griffiths and D. F. Schroeter, *Introduction to Quantum Mechanics* (Cambridge University Press, 2018), 3rd ed.
- [78] A. P. A. P. French, *An introduction to quantum physics*, M.I.T. introductory physics series (CRC Press, 1978), ISBN 9781315137308.

- [79] E. Arimondo, M. Inguscio, and P. Violino, Rev. Mod. Phys. **49**, 31 (1977), URL <https://link.aps.org/doi/10.1103/RevModPhys.49.31>.
- [80] D. M. Stamper-Kurn and M. Ueda, Rev. Mod. Phys. **85**, 1191 (2013), URL <https://journals.aps.org/rmp/abstract/10.1103/RevModPhys.85.1191>.
- [81] N. P. Proukakis and B. Jackson, J. Phys. B **41**, 203002 (2008), URL <https://iopscience.iop.org/article/10.1088/0953-4075/41/20/203002>.
- [82] E. P. Gross, Nuovo Cimento **20**, 454 (1961), URL <https://doi.org/10.1007/BF02731494>.
- [83] P. P. Pitaevskii, Soviet Phys. JETP. **13**, 451 (1961).
- [84] N. N. Bogoliubov, Il Nuovo Cimento **7**, 794 (1958), URL <https://doi.org/10.1007/BF02745585>.
- [85] C. Pethick and H. Smith, *Bose-Einstein condensation in dilute gases* (Cambridge University Press, 2008), 2nd ed., ISBN 9780521846516.
- [86] L. Pitaevskii and S. Stringari, *Bose-Einstein Condensation and Superfluidity*, International Series of Monographs on Physics (OUP, Oxford, 2016), ISBN 9780198758884.
- [87] M. J. Steel, M. K. Olsen, L. I. Plimak, P. D. Drummond, S. M. Tan, M. J. Collett, D. F. Walls, and R. Graham, Phys. Rev. A **58**, 4824 (1998), URL <https://journals.aps.org/pra/abstract/10.1103/PhysRevA.58.4824>.
- [88] P. Blakie, A. Bradley, M. Davis, R. Ballagh, and C. Gardiner, Advances in Physics **57**, 363 (2008), URL <https://doi.org/10.1080/00018730802564254>.
- [89] C. W. Gardiner, J. R. Anglin, and T. I. A. Fudge, Journal of Physics B: Atomic, Molecular and Optical Physics **35**, 1555 (2002), URL <https://iopscience.iop.org/article/10.1088/0953-4075/35/6/310>.
- [90] C. W. Gardiner and M. J. Davis, Journal of Physics B: Atomic, Molecular and Optical Physics **36**, 4731 (2003), URL <https://iopscience.iop.org/article/10.1088/0953-4075/36/23/010>.
- [91] A. S. Bradley, C. W. Gardiner, and M. J. Davis, Phys. Rev. A **77**, 033616 (2008), URL <https://journals.aps.org/pra/abstract/10.1103/PhysRevA.77.033616>.
- [92] A. S. Bradley and P. B. Blakie, Phys. Rev. A **90**, 023631 (2014), URL <https://journals.aps.org/pra/abstract/10.1103/PhysRevA.90.023631>.

- [93] H. Stoof, Journal of Low Temperature Physics **114**, 11 (1999), URL <https://link.springer.com/article/10.1023/A:1021897703053>.
- [94] H. T. C. Stoof and M. J. Bijlsma, Journal of Low Temperature Physics **124**, 431 (2001), URL <https://link.springer.com/article/10.1023/A:1017519118408>.
- [95] K. Brown, T. Bland, P. Comaron, and N. P. Proukakis, Phys. Rev. Res. **3**, 013097 (2021), URL <https://link.aps.org/doi/10.1103/PhysRevResearch.3.013097>.
- [96] Y. Kawaguchi and M. Ueda, Physics Reports **520**, 253 (2012), URL <https://www.sciencedirect.com/science/article/pii/S0370157312002098>.
- [97] G. R. Dennis, J. J. Hope, and M. T. Johnsson, Computer Physics Communications **184**, 201 (2013), URL <https://www.sciencedirect.com/science/article/pii/S0010465512002822>.
- [98] B. Efron, *Bootstrap Methods: Another Look at the Jackknife*. In: Kotz, S., Johnson, N.L. (eds) *Breakthroughs in Statistics*, Springer Series in Statistics (Springer, New York, 1992), ISBN 978-1-4612-4380-9.
- [99] I. G. Hughes and T. P. A. Hase, *Measurements and their uncertainties : a practical guide to modern error analysis* (Oxford University Press, 2010), ISBN 9780199566327.
- [100] M. Lapaine and E. L. Usery (Eds.), *Choosing a map projection* (Springer, 2017), ISBN 978-3-319-51834-3.
- [101] C. N. Weiler, T. W. Neely, D. R. Scherer, A. S. Bradley, M. J. Davis, and B. P. Anderson, Nature **455**, 948 (2008), ISSN 0028-0836, 1476-4687, URL <https://www.nature.com/articles/nature07334>.
- [102] I.-K. Liu, S. Donadello, G. Lamporesi, G. Ferrari, S.-C. Gou, F. Dalfovo, and N. P. Proukakis, Commun Phys **1** (2018), ISSN 2399-3650, URL <http://www.nature.com/articles/s42005-018-0023-6>.
- [103] S. J. Rooney, T. W. Neely, B. P. Anderson, and A. S. Bradley, Phys. Rev. A **88**, 063620 (2013), URL <http://link.aps.org/doi/10.1103/PhysRevA.88.063620>.
- [104] M. Ota, F. Larcher, F. Dalfovo, L. Pitaevskii, N. P. Proukakis, and S. Stringari, Phys. Rev. Lett. **121**, 145302 (2018), URL <https://link.aps.org/doi/10.1103/PhysRevLett.121.145302>.
- [105] A. S. Bradley, S. J. Rooney, and R. G. McDonald, Phys. Rev. A **92**, 033631 (2015), URL <https://link.aps.org/doi/10.1103/PhysRevA.92.033631>.

- [106] S. P. Cockburn, D. Gallucci, and N. P. Proukakis, Phys. Rev. A **84**, 023613 (2011), URL <https://link.aps.org/doi/10.1103/PhysRevA.84.023613>.
- [107] M. J. Davis, P. B. Blakie, A. H. van Amerongen, N. J. van Druten, and K. V. Kheruntsyan, Phys. Rev. A **85**, 031604 (2012), URL <https://link.aps.org/doi/10.1103/PhysRevA.85.031604>.
- [108] J. B. Trebbia, J. Esteve, C. I. Westbrook, and I. Bouchoule, Phys. Rev. Lett. **97**, 250403 (2006), URL <https://link.aps.org/doi/10.1103/PhysRevLett.97.250403>.
- [109] A. H. van Amerongen, J. J. P. van Es, P. Wicke, K. V. Kheruntsyan, and N. J. van Druten, Phys. Rev. Lett. **100**, 090402 (2008), URL <https://link.aps.org/doi/10.1103/PhysRevLett.100.090402>.
- [110] A. L. Gaunt, T. F. Schmidutz, I. Gotlibovych, R. P. Smith, and Z. Hadzibabic, Phys. Rev. Lett. **110**, 200406 (2013), URL <https://journals.aps.org/prl/abstract/10.1103/PhysRevLett.110.200406>.
- [111] F. Salces-Carcoba, C. J. Billington, A. Putra, Y. Yue, S. Sugawa, and I. B. Spielman, New Journal of Physics **20**, 113032 (2018), URL <https://iopscience.iop.org/article/10.1088/1367-2630/aaef9b>.
- [112] T. I. Fossen and H. Nijmeijer, eds., *Parametric resonance in dynamical systems* (Springer, 2012), ISBN 9781461410430.
- [113] D. Kirzhnits and A. Linde, Physics Letters B **42**, 471 (1972), ISSN 0370-2693, URL <http://www.sciencedirect.com/science/article/pii/0370269372901098>.
- [114] L. Dolan and R. Jackiw, Phys. Rev. D **9**, 3320 (1974), URL <https://link.aps.org/doi/10.1103/PhysRevD.9.3320>.
- [115] S. Weinberg, Phys. Rev. D **9**, 3357 (1974), URL <https://link.aps.org/doi/10.1103/PhysRevD.9.3357>.
- [116] S. J. Rooney, P. B. Blakie, and A. S. Bradley, Phys. Rev. A **86**, 053634 (2012), URL <https://journals.aps.org/pra/abstract/10.1103/PhysRevA.86.053634>.
- [117] C. Foot, *Atomic Physics*, Oxford Master Series in Physics (OUP, Oxford, 2005), ISBN 9780198506966.
- [118] C. Gerry and P. Knight, *Introductory quantum optics* (Cambridge University Press, 2005), ISBN 9780511791239.

Bibliography

- [119] K. C. Wright, L. S. Leslie, and N. P. Bigelow, Phys. Rev. A **78**, 053412 (2008), URL <https://journals.aps.org/pra/abstract/10.1103/PhysRevA.78.053412>.
- [120] A. Griffin, T. Nikuni, and E. Zaremba, *Bose-condensed gases at finite temperatures* (Cambridge University Press, 2009), ISBN 9780521837026.